Ultrasound Energy Transfer using Charged CMUTs

Youri Westhoek

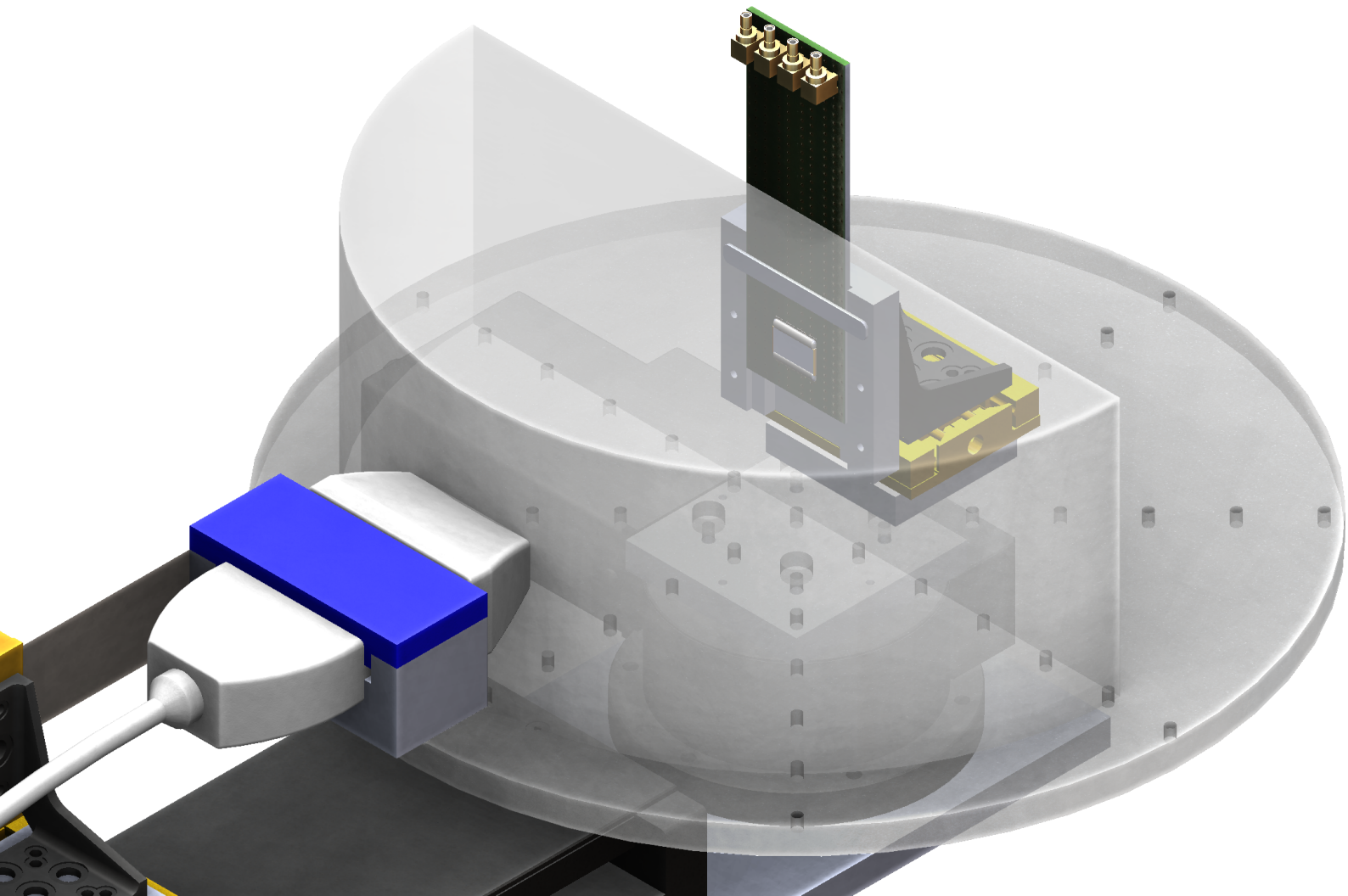

Ultrasound Energy Transfer using Charged CMUTs

Thesis

by

Youri Westhoek

to obtain the degree of
Master of Science
at the Delft University of Technology

Thesis committee:

Prof. dr. ir. R. Dekker,	TU Delft, Philips
Prof. dr. P. J. French,	TU Delft
Dr. V. Giagka,	TU Delft
Dr. M. Mastrangeli,	TU Delft

Abstract

Implantable medical devices (IMDs) such as cardiac pacemakers, cochlear implants, and neurostimulators improve millions of people's lives every day. Over the years, IMDs have significantly improved in function, increased in lifetime, and decreased in size. However, further miniaturisation is limited by the batteries used to power these devices, and therefore methods to power them wirelessly are gaining in popularity. The technique most used to wirelessly power IMDs is electromagnetic energy transfer. However, at low frequencies this method is limited to shallow implants due to its low directivity, while at high frequencies it is limited by attenuation in the human body. Therefore, ultrasound energy may be the future of wirelessly powering implants. Its high directivity and low attenuation in the human body opens up the possibility to wirelessly power deep implants without any harmful side effects.

An ultrasound energy transfer set-up was established in this work to demonstrate that Philips' capacitive micromachined ultrasound transducers (CMUTs) can be used as ultrasound energy harvesters. Normally, CMUTs need a bias voltage to function as an energy harvester. However, the CMUTs in this work are chargeable and therefore eliminate the need for this bias voltage.

The results show that charged CMUTs can indeed be used as efficient energy harvesters of ultrasound and that information can be sent back to the ultrasound probe using echo modulation. The charged CMUTs showed to be able to harvest sufficient energy to stimulate a nerve and power a Bluetooth module, even when ultrasound sent through 90 mm of biological (pork) tissue. The maximum power harvested during the ultrasound energy transfer experiments was 250 mW over a transferring distance of 75 mm.

Acknowledgements

First of all, I want to thank Ronald Dekker for giving me the opportunity to graduate from Philips Research. Thank you for your daily optimism, jokes, and foremost for creating an atmosphere that felt like home.

Next, I would like to thank Shinnosuke Kawasaki for being my daily supervisor for the last year. Thank you for guiding me through my project and helping me create something that I'm proud of.

Then I would like to thank Eugene Timmering. Thank you for your help, knowledge, and cheerful attitude that made everything easier within Philips. I also would like to thank Chris van Heesch and Frank van Heesch for all the technical support I received during the year. You have been of great help.

A big thank you to all the other interns and PhDs for making graduating more of a joy than I thought it would be. Thank you, Marta, Jian, Jia-Jun, Dino, Indu, Eric, Joshua, and Sevda, for all the great times we have had together.

Finally, I want to thank my family. Thank you, Oma, for your kindness, thank you, Luuk and Fleur, for being the best brother and sister imaginable, and of course, thank you, Mam and Pap, for always being there for me. You mean everything to me. Words cannot describe how grateful I am to have you all in my life.

Contents

List of Figures

List of Tables

1

Introduction

This thesis aims to demonstrate that Philips' capacitive micromachined ultrasound transducers (CMUTs) can be used as ultrasound energy harvesters of ultrasound energy transmitted by a medical imaging probe.

In this Chapter, an introduction is given to implantable medical devices, the biophysics of ultrasound, ultrasound energy transferring systems, and Philips' capacitive micromachined ultrasound transducer.

1.1. Implantable Medical Devices

Implantable medical devices (IMDs) have their place in the medical world for a while now. Devices such as cardiac pacemakers, cochlear implants, and neurostimulators improve millions of people's lives every day. Over the years, IMDs have significantly improved in function, increased in lifetime and durability, and decreased in size.

An important factor in both the size and the lifetime of an implantable medical device is the way it is powered. The most common implantable medical devices' power requirement is shown in table 1.1.

Table 1.1: Power requirements for typical implanted medical devices [36]

Implanted device	**Typical power requirement**
pacemaker	30-100 μW
cardiac defibrillator	30-100 μW
neurological stimulator	30 μW to several mW
drug pump	100 μW to 2 mW
cochlear implants	10 mW

Improving powering methods while satisfying the above-mentioned power requirements could play an important role in the further development of implantable medical devices. Especially in the miniaturisation of IMDs, since it would be best to keep IMDs as less intrusive as possible for patients.

The first active implantable medical devices used trans-cutaneous lead wires to power the device. In this case, the powering of the device was done by wires through the skin connected to a power source

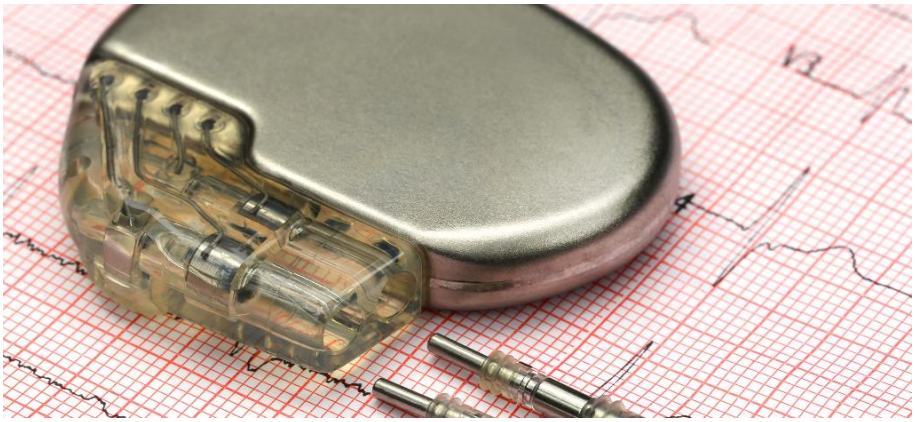

Figure 1.1: An IMD in the form of a neurological stimulator [26]

outside of the body. With this form of powering, the patient has limited freedom in movement, and it imposed infection risks for the patient [37].

Most of the active implantable medical devices on the market today use a battery encapsulated within the implant, eliminating the need for trans-cutaneous wires and preserving the freedom of movement for the patient. However, these batteries take up to 60% of the volume of the implant, limiting further miniaturisation (see figure 1.2). Furthermore, these batteries have a limited lifespan and need to be replaced every 5 to 10 years, requiring an invasive surgical procedure.

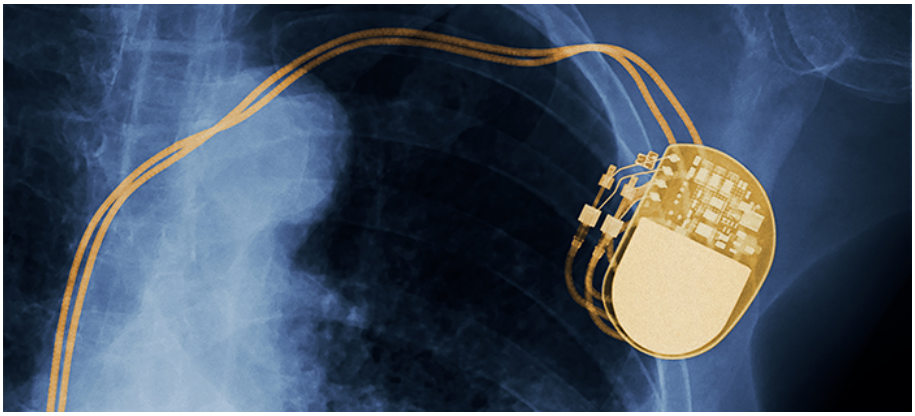

Figure 1.2: X-ray image of a neurological stimulator showing the volume usage of the internal battery [12]

In a new wave of technological advances now wireless energy transfer (WET) technologies have emerged. These technologies generally use an external power source that transmits energy wirelessly through the skin to the IMD that in turn collects the energy received into its internal battery or uses the energy received directly for a certain function.

Wireless energy transfer offers a solution for the long-term powering of implantable medical devices and may be a way to prolong the lifetime of IMDs. Current research in wireless power transfer for medical devices shows that various methods can be used to directly power implantable medical devices, of which electromagnetic energy transfer is the most used. However, ultrasound energy transfer (UET), a method in which mechanical ultrasound waves are used as the energy carrier, shows some significant advantages over electromagnetic energy transfer: such as lower attenuation and smaller wavelengths. Making it possible to focus ultrasound deep inside the body on small transducers.

1.2. Biophysics of Ultrasound

The use of ultrasound waves is a relatively new way of transferring power to implantable medical devices but already was first used in 1985 for biomedical applications [7][27]. ultrasound energy transfer is a method in which energy is transferred from a transmitting transducer to a receiving transducer using ultrasound waves (acoustic waves with a frequency of 20 kHz and higher).

The main advantage of using ultrasound waves for wireless energy transfer for biomedical applications is that due to the short wavelengths of ultrasound waves in the body (typically less than 1 mm), the energy can be focused in a specific spot. Furthermore, they are not susceptible to electromagnetic interference and don't interfere with existing wiring within the body, as is the case for electromagnetic waves [21].

The acoustic intensity is defined as the incident power per unit area and can be described as shown in equation 1.1. Integrating the incident power per unit area over the excited area yields the acoustic power delivered, usually given in milliwatts (mW) [17].

$$\vec{I}(x,y,z,t) = p(x,y,z,t)\vec{c}(x,y,z,t) \tag{1.1}$$

where:

$\vec{I}(x,y,z,t)$ = The intensity vector in W
$p(x,y,z,t)$ = The pressure field in Pa
$\vec{c}(x,y,z,t)$ = The acoustic velocity vector at a specific location in m/s

Ultrasound benefits from the same benefits known for ultrasound imaging in the body, including the ability to penetrate deep in the body without being significantly attenuated. With a low attenuation coefficient α_0 of 0.5–1.0 dB cm^{-1} MHz^{-1} through tissue. Depending on the frequency, ultrasound waves are capable of traveling through gases, liquids, and solids [32][23][27][35].

The attenuation of an ultrasound wave is described by equation 1.2. For soft tissue, b is 1 [23]. In table 1.2 the attenuation for the most relevant mediums related to wireless energy transfer of active implantable biomedical devices are given for an ultrasound signal with frequency f=1 MHz.

$$\alpha = \alpha_0 \cdot f^b \tag{1.2}$$

where:

α = The attenuation factor
α_0 = Attenuation coefficient of the tissue in dB cm^{-1} MHz^{-1}
f = The frequency of the ultrasound signal in Hz
b = Tissue coefficient, for soft tissue b = 1

Another important physical phenomenon of ultrasound is reflection. Reflection occurs when there is an acoustic impedance mismatch between the transducer and the medium or during a transition from one medium to another. In the case of ultrasound energy transfer, part of the transmitted energy will not reach the receiving transducer when reflections occur due to an impedance mismatch. In table 1.2 the acoustic impedance for the most relevant mediums related to wireless energy transfer of active implantable biomedical devices is given.

Table 1.2: Acoustic properties of biological tissues [8]

Acoustic properties of biological tissues						
for $f = 1MHz$*:*	**Water (**20 °C**)**	**Cortical bone**	**Fat**	**Muscle**	**Tendon**	**Soft tissue**
Attenuation dB/cm	0.0022	6.9	0.48	1.09	4.7	0.54
Velocity m/s	1480	3476	1478	1547	1670	1561
Impedance $MRayl$	1.48	7.38	1.40	1.62	1.84	1.63

For the efficient transfer of energy from the transducer to the body, impedance matching is used. Impedance matching is done by inserting an intermediate medium with an acoustic impedance value lying in between that of the mismatched mediums to create a gradual transition from one acoustic impedance to the next. This layer is also called a coupling layer. An example is shown in figure 1.4. The extra medium can be a single layer medium [21], or a multi-layer medium [13].

To focus ultrasound waves onto the receiving transducer within the body, different techniques can be used. Ultrasound waves have the advantage with respect to electromagnetic waves that their wavelengths are significantly shorter [23][6]. Equation 1.3 shows the relationship between the wavelength, speed, and frequency of an acoustic signal.

$$\lambda = \frac{v}{f} \tag{1.3}$$

where:

$\lambda =$ wavelength in m
$v =$ speed of sound in m/s
$f =$ frequency in Hz

Substituting in equation 1.3 for the velocity of sound in tissue v = 1480 m/ sec, shows that ultrasound waves have submillimeter wavelengths for a frequency of 1.5 MHz and higher. Meaning that ultrasound energy transfer can work with much smaller receiving transducers than electromagnetic energy transfer systems.

There are several ways to focus ultrasound energy. For example, acoustic lenses focus an acoustic wave the same way normal lenses focus light [11]. Alternatively, piezo-composite materials used in piezoelectric ultrasound transducers can be mechanically shaped, thus producing focused beams without using acoustic lenses [23].

The characteristics of the generated pressure field of an acoustic transmitter changes with the distance. In the near field, the acoustic pressure of an acoustic transmitter is generally unpredictable, whereas the acoustic pressure has a smooth decay with distance for the far-field. Where the near-field transitions into the far-field, a natural focus point exists. This natural focal point of an acoustic transducer is called the *Rayleigh Distance* (L) and is defined as:

$$L = \frac{\left(D^2 - \lambda^2\right)}{4\lambda} \approx \frac{D^2}{4\lambda}, D^2 \gg \lambda^2 \tag{1.4}$$

where:

L = the Rayleigh distance in m
λ = wavelength in m
D = diameter of the aperture in m

These methods of focusing result in a fixed focusing distance, and therefore, the transmitting transducer needs to be physically positioned to focus the energy upon the receiving transducer to efficiently transfer energy [29].

A more versatile way of focusing ultrasound energy upon a receiving transducer is beam-forming. Beam-forming is a technique in which directional information is given to received or transmitted signals. For example, in B-mode imaging, Time of Arrival (ToA) and Time Difference of Arrival (TDoA) techniques are used to reconstruct an image in a specific direction with respect to the receiving transducer. Vice versa, manipulating the time differences between transducer elements of a transmitting transducer can give spatial directivity to a transmitted signal; focusing the signal in a specific direction [35]. A visual representation of such a focus point is illustrated in figure 1.3.

The Verasonics Vantage system, created for ultrasound research, has the capability to focus the transmitted beam at a specific point, significantly increasing the power output compared to an unfocused beam [35].

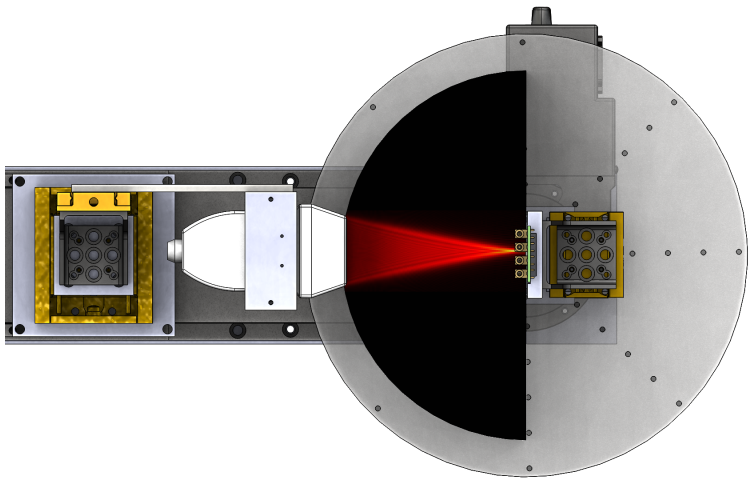

Figure 1.3: A simulation of a focal point obtained when focusing the Philips L7-4

To wirelessly charge or power an active implantable medical device, it is crucial to know where the implant is located. To localise an implant, harmonic back-scattering as utilised in conventional B-mode ultrasound imaging can be used. The implant may, however, not be distinguishable from other objects within the body. In this case, the implant may need a mechanism to change its reflection over time so that the implant can be recognised. In the case of a PZT crystal, it can be short-circuited periodically so that the reflection changes over time [35].

Localisation accuracy depends on the aperture of the ultrasound array [35]. For optimal localisation of the implant, it is beneficial to use a probe with sufficient elements for high accuracy, both in imaging and energy focusing.

Since ultrasound is widely used for imaging purposes, many safety guidelines for the safe use of ultrasound are already in place. These safety guidelines are based on several biophysical effects of ultrasound.

One biophysical effect of ultrasound that has to be considered is thermal heating due to the energy absorption by the tissue through which the ultrasound is sent. The thermal index (TI) is used to quantify this heating and is calculated, as shown in equation 1.5.

$$\mathrm{TI} = \frac{W_{\mathrm{p}}}{W_{\mathrm{deg}}} \tag{1.5}$$

where:

TI = the thermal index
W_p = acoustic power at a specific location in W
W_{deg} = power needed to elevate the temperature of a tissue by 1 °C in W

Also, the mechanical biophysical effect of ultrasound is important to take into account. Negative pressures in the acoustic field can cause cavitation; the creation of microscopic bubbles in biological tissue that can potentially implode or explode and could lead to the formation of free radicals [1][9]. To quantify the strength of the mechanical interaction of ultrasound with tissue, the mechanical index (MI) is used [14]. The mechanical index is given by equation 1.6.

$$MI = \frac{p_N}{\sqrt{f_{US}}} \tag{1.6}$$

where:

MI = the mechanical index
p_N = the negative peak pressure in Pa
f_{US} = the frequency of the ultrasound signal in Hz

Furthermore, the FDA has defined the maximum spatial-peak temporal-average intensity (I_{SPTA}) and the spatial-peak pulse-average intensity (I_{SPPA}), both given in power per unit area. The safety limits for the TI, MI, I_{SPTA} and I_{SPPA} for the use of ultrasound in the body are summarized in table 1.3.

Table 1.3: Safety limits for ultrasound [14][3][2]

Safety limits for ultrasound	
TI	≤ 6
MI	≤ 1.9
I_{spta}	$\leq 720\,\mathrm{mW\,cm^{-2}}$
I_{sppa}	$\leq 190\,\mathrm{W\,cm^{-2}}$

1.3. Ultrasound Energy Transfer

An ultrasound energy transferring system usually consists of an external transmitter, a coupling layer, an implanted receiver, a harvesting circuit, and an implanted medical device. A schematic overview of a typical ultrasound energy transferring system is shown in figure 1.4.

Ultrasound energy transfer allows for shorter wavelengths than electromagnetic energy transfer; the current state of the art in wireless energy transfer. Because of these shorter wavelengths, higher beam directivity can be obtained, which in turn allows for smaller receiving transducers [4][32][23].

Ultrasound energy transfer for now has a lower maximum system efficiency than electromagnetic energy transfer, and generally can generate only a few Milliwatts (mW) [1][22][19][31][34][39] with total system efficiencies ranging from 0.4% to 39.1%, for distances ranging from 20 cm to 0.5 cm. However, for receiver transducers smaller than 10 mm and for IMDs implanted deeper than 10 cm ultrasound energy transfer outperforms electromagnetic energy transfer [23]. This makes ultrasound energy transfer an attractive alternative worth exploring.

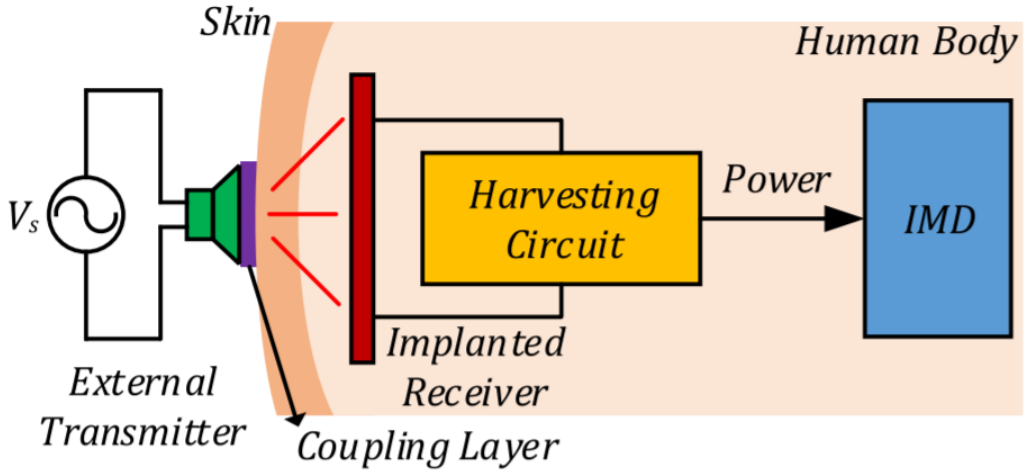

Figure 1.4: A typical ultrasound energy transfer system [1]

The external transducer is the ultrasound source; it transmits the ultrasound wave and provides the energy to the internal transducer. For the external transducer, usually, PZT crystals and PZT probes are used. In case of an array of PZT crystals or a linear array PZT probe, beam-forming can be used as a technique to focus the beam upon the implanted receiver [22][19][31][34][39].

The coupling layer serves to reduce the impedance mismatch between the external transmitter and the tissue or phantom in which the implanted receiver is positioned. In the case of ultrasound energy transfer and ultrasound imaging, the impedance mismatch between the transducer and the human skin is minimised by using an acoustic gel or water as the coupling layer.

For the internal receiver, generally, two types of ultrasound transducers are used: piezoelectric ultrasound transducers (PUTs) and capacitive ultrasound transducers (CUTs). Additionally, the internal ultrasound transducer is usually integrated into the active implantable medical device because of the compactness of such a transducer [1][23].

Capacitive ultrasound transducers (CUTs) are composed of two electrodes with a vacuum gap in between. The bottom electrode is fixed to the silicon substrate, and the top electrode is part of a movable membrane as can be seen in figure 1.5. CUTs can convert the received mechanical ultrasound wave into the electrical domain through its changing capacitance induced by the vibrating top electrode.

CUTs can also send ultrasound waves by applying an alternate signal over the capacitive structure and thereby inducing motion in the membrane [1][40].

Piezoelectric ultrasound transducers (PUTs) are based on the piezoelectric effect of piezoelectric materials. When piezoelectric materials are put under strain, an electric charge is generated across the materials surface [30]. Incoming ultrasound waves induce a strain upon the piezoelectric material, generating an electric potential, thus converting ultrasound waves into electric energy. The other way around, piezoelectric materials will go under strain when an electric potential is applied over its surface. When an alternating signal is applied, this mechanical strain will be rhythmic; resulting in ultrasound waves [1]. The material most often used for its piezoelectric effect is PZT (lead zirconate titanate) [15].

The capacitive ultrasound transducer has the advantage that it can be fabricated through standard integrated circuits (IC) based fabrication techniques and thus can be mass-produced. Piezoelectric ultrasound transducers usually need bulk materials rather than thin-film deposited materials to obtain maximum power generation, and therefore are often not IC integrated. Besides that, PZT is not biocompatible [4].

PUTs and CUTs have an optimal energy transfer efficiency when both the receiving transducer and the transmitting transducer work at the same operating frequency. This frequency is usually called the resonance frequency since its frequency is determined by the transducer's mechanical structure. For PUTs, it depends on the piezoelectric material and its thickness. In contrast, for CUTs, it mainly depends on the vibrating surface area of the membrane, usually determined by the magnitude of the bias-voltage used to drive the CUT. By tuning the bias-voltage, CUTs may have the possibility to be set to the 'right' operating frequency so that maximum energy transfer is achieved.

The harvesting circuit rectifies the incoming AC signal from the implanted receiving transducer, which is usually done by a full-bridge rectification circuit. The rectified signal can be used to directly power an implantable medical device or charge its internal battery.

1.4. The Capacitive Micromachined Ultrasound Transducer

A capacitive micro-machined ultrasound transducer (CMUT) consists of a top and bottom electrode separated by a dielectric layer and a vacuum gap. There are two operating modes; reception and transmission [24]. In receive mode, an incoming ultrasound wave will mechanically displace the membrane resulting in an alternating electric current. In transmitting mode, an alternating voltage is applied to the CMUT, causing the top and bottom electrodes to exert electrostatic force upon each other, causing the top electrode – the membrane - to vibrate, producing ultrasound waves.

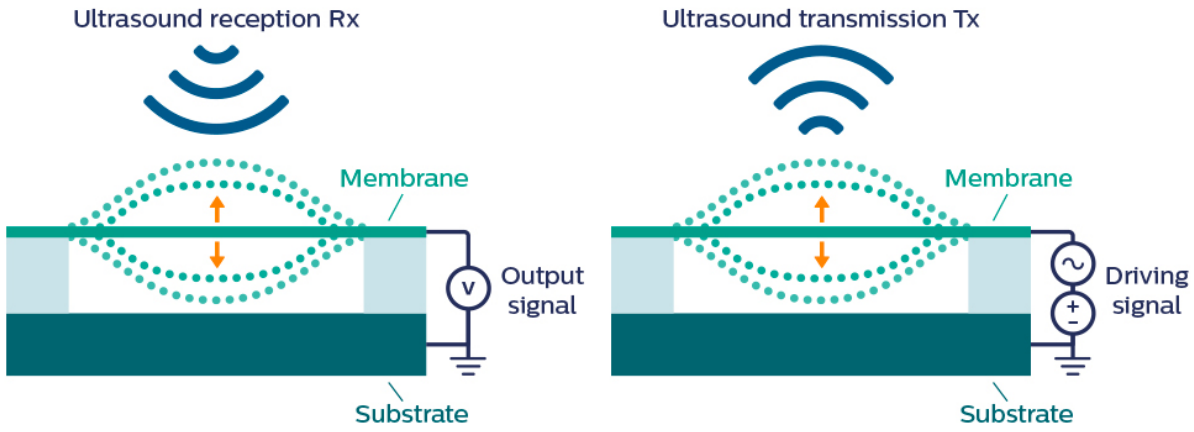

Figure 1.5: Receiving and transmission modes of a CUT [24]

For energy transferring purposes, CMUTs should be operated in collapsed mode, meaning that the top membrane is collapsed onto the dielectric of the bottom electrode at all times during operation [20]. In collapsed mode, CMUTS have a higher power efficiency than when operated in non-collapse mode [5][38]. To get a CMUT into collapse mode, a bias voltage is applied between the top and bottom electrodes, generating an electric field between the plates causing the top membrane to collapse onto the bottom dielectric.

To improve collapsed mode CMUTs, Philips Research has done extensive research into different layer structures to increase the electrostatic force acting on the membrane to increase the acoustic output power. One of the investigated layer structures involved a layer of the high dielectric constant material Al_2O_3 embedded within the bottom dielectric, but was shelved as a viable solution for ultrasound transmission since the CMUTs with an incorporated layer of Al_2O_3 showed to have a non-linear behaviour due to a charging effect of the Al_2O_3 layer.

This charging effect induced by the layer of Al_2O_3 incorporated into the bottom dielectric is because Al_2O_3 is a dielectric with a high dielectric constant, into which charges can be tunnelled by applying a bias voltage [25]. These charges remain trapped when the bias voltage is removed. Thus a permanent electric field is generated exerting a permanent electrostatic force upon the membrane, holding it in collapse without the need for a permanently applied bias voltage. A CMUT in collapse mode can then be driven with only an alternating voltage signal, as shown in figure 1.7.

The CMUT can be modeled using the Van Dyke model. An altered version of the Van Dyke model where the capacitance is split into two capacitances in series is shown in figure 1.6. Where R_m, L_m and C_m are the electrical equivalents of a mass-spring-damper system, used to model the physical behavior of the CMUT, and where C_1 and C_2 are the capacitive properties of the CMUT resulting from the layer structure, as shown in figure 1.7 [16].

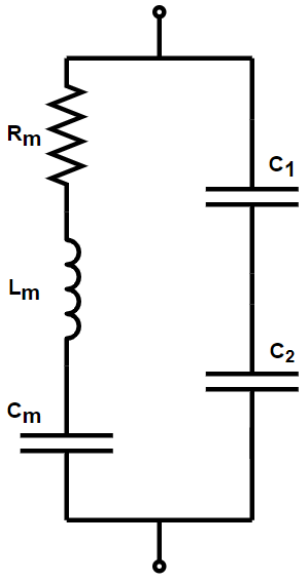

where:

R_m = the electrical equivalent of a mass
L_m = the electrical equivalent of a spring
C_m = the electrical equivalent of a damper
C_1 = the capacity between the top electrode and the Al_2O_3 layer
C_2 = the capacity between the bottom electrode and the Al_2O_3 layer

Figure 1.6:
Electrical equivalent of a CMUT

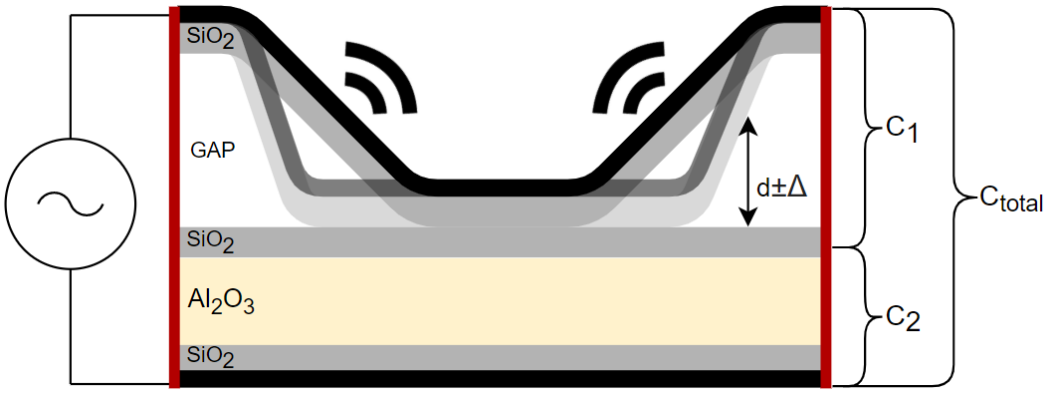

Figure 1.7: A collapsed mode CMUT

Previous research on the CMUTs used in this work done within Philips Research by M. Saccher and S. Kawasaki show that the energy harvesting efficiency of the CMUTs is 43.4% for an ultrasound wave of 2.15 MHz and that the energy harvesting efficiency for an ultrasound wave of 5.85 MHz is 48.8% [28]. Without the need for a permanent bias voltage and with a high power harvesting efficiency, a charged CMUT is a great option for directly powering or charging an active implantable device.

2

Materials and Methods

In this Chapter, the materials and methods used to achieve a working ultrasound energy transferring system are discussed. First, the energy harvester, energy transmitting system, and the experimental set-up are explained. Finally, an overview of the total ultrasound energy transfer system is given.

2.1. The Energy Harvester

In this section, the energy harvester is elaborated. The energy harvester has two components: a printed circuit board consisting of charged capacitive micromachined ultrasound transducers and a matching and rectification circuit.

2.1.1. The Capacitive Micromachined Ultrasound Transducer

The energy harvester uses charged capacitive micromachined ultrasound transducers mounted on a printed circuit board as the energy receiver, from now on referred to as *CMUT*. The CMUT is made using a standard IC fabrication based process and consists of multiple layers. The layers used in these CMUTs can vary depending on the application of the specific CMUT, and therefore different configurations exist.

In this work, three different types of CMUTs were characterised to determine which configuration is best suited for ultrasound energy harvesting. The types differ in their layer structures, but all of them have a layer of the charge trapping Al_2O_3 incorporated, allowing for them to be charged. The layer structures can be found in table 2.1.

The CMUT devices used in this work consist of 128 elements of 56 CMUT drums each, resulting in a total of 7168 drums. The devices were mounted on a PCB with connectors for testing, as shown in figure 2.3. Each connector connects to 6 elements of 56 drums, resulting in 336 connected drums, each having a diameter of 135µm (figure 2.1).

Table 2.1: The layer structures of the P67, P103, and P69 CMUTs

Layer structures of the characterised CMUTs					
Step	**Layer**	**Unit**	***P67***	***P103***	***P69***
Substrate			P	P	P
ILD	Therm. Ox.	nm	2000	2000	2000
IN	AlNd/WTi	nm	190/50	190/50	190/50
1st Dielectric	TEOS	nm			
	ALD SiO2	nm	50	50	10
	ALD Al2O3	nm	200	200	240
	ALD SiO2	nm	50	50	30
INS	AlNd	nm	500	500	500
D2D	TEOS	nm			
	ALD SiO2	nm	100	200	100
2nd Dielectric	TEOS	nm			
	ALD SiO2	nm	50	50	30
INT	WTi/AlNd	nm	50/190	50/190	50/190
ON	Oxide	nm	50	50	50
ON	SiN	nm	2400	2250	2420
M1 metal	Mo	nm		40	
	AlNd	nm	100	100	100
M1 protec.	Oxide	nm	50	50	50
	SiN	nm	150	150	150
Plug	SiN	nm	2000	2000	2000
BP	Al	nm	1000	1000	1000

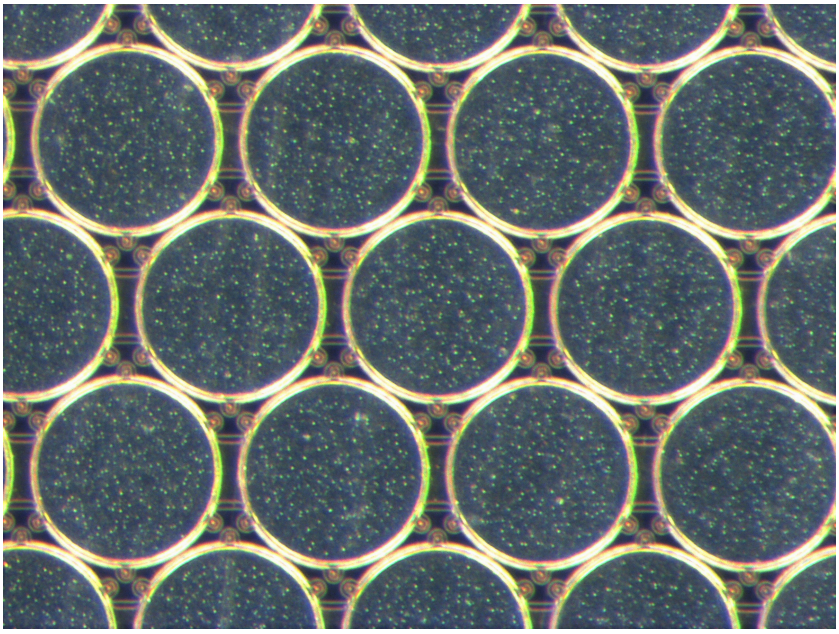

Figure 2.1: The drums of a CMUT

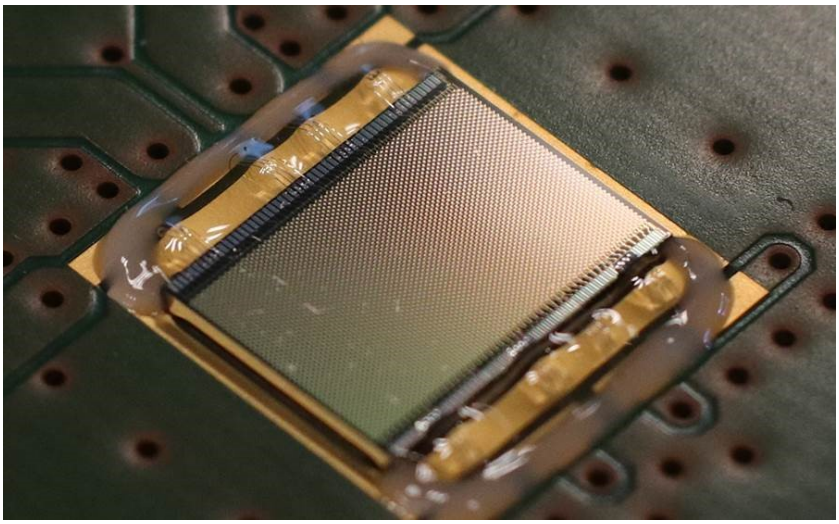

Figure 2.2: An array of capacitive micromachined ultrasound transducers

Figure 2.3: The PCB mounted CMUT

2.1.2. Charging of the Capacitive Micromachined Ultrasound Transducer

Charging of a CMUT is done by applying a bias voltage high enough to collapse the top membrane of the CMUT, and tunnel charges into the Al_2O_3 layer. Two independent variables were taken into account while charging; charging-voltage and charging-duration. The measurement table with the selected values for these independent variables is shown in table 2.2.

Table 2.2: The charging measurement table

	Duration [s]							
Voltage [V]		.1	1	5	30	60	300	600
	125							
	150							
	175							
	200							

The charging of each CMUT was done using the programmable power source Keithley Interactive SourceMeter Model 2450 connected to a PC via a GPIB-USB-HS IEEE 488 controller and programmed in TSP using Test Script Builder. The power source's current output was limited by placing a 1 MΩ in series with the CMUT.

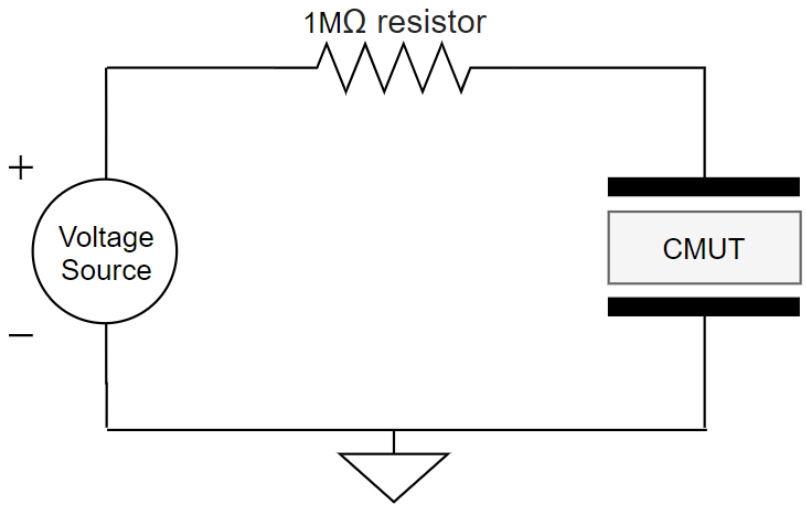

Figure 2.4: The circuit used to charge the CMUTs

Since the CMUT can be modeled as a resonance circuit (RLC) in parallel to two capacitors in series (see figure 1.6), the general behavior of the impedance spectrum of a collapsed-mode CMUT resembles that of a capacitor with one or more resonance peaks. As an example, the impedance and phase spectra of a CMUT with its first resonance frequency at 1.5MHz is shown in figure 2.5.

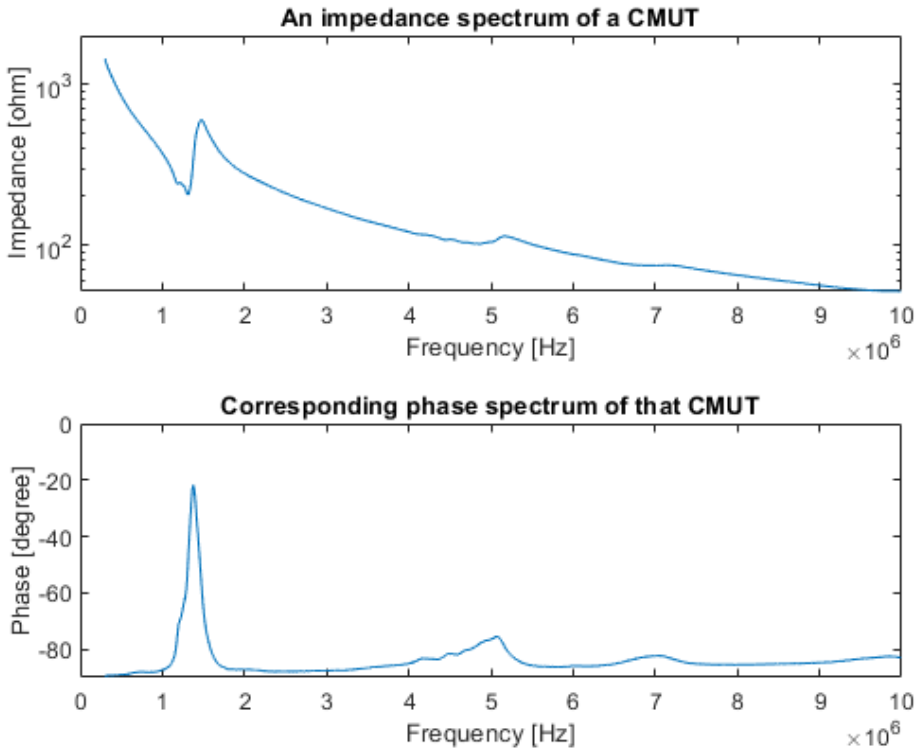

Figure 2.5: The typical behaviour of a collapsed-mode CMUT

It is desirable to operate the CMUT at its first resonance frequency. The collapsed membrane is optimally mechanically displaced at this frequency, producing or harvesting the optimal amount of power [20]. The phase peak height is a good indicator of the power transfer efficiency; a higher phase peak will mean higher efficiency. Varying the bias voltage will change the degree in which the membrane is collapsed, shifting its first resonance frequency, thus shifting its optimal operating frequency.

When a CMUT goes into the collapsed mode, the entire impedance spectrum shows a sudden decrease in impedance, due to the sudden increase in capacitance across the vacuum gap.

Completing table 2.2 for each type of CMUT gives insight into the charging behavior of the CMUTs. The focus is on finding under which circumstances the CMUTs will start charging, what amount of charge will be trapped, and what effect charging has on the operation of the CMUTs.

2.1.3. Discharging of the Capacitive Micromachined Ultrasound Transducer

A charged CMUT can be discharged by applying an AC voltage over the top and bottom electrodes. The AC voltage removes the trapped charges from the dielectric layer of Al_2O_3 by way of charging and discharging during every cycle, averaging a potential of 0 V, through which the resulting charge potential eventually approaches 0 V. The dis-charging circuit used is shown in figure 2.6.

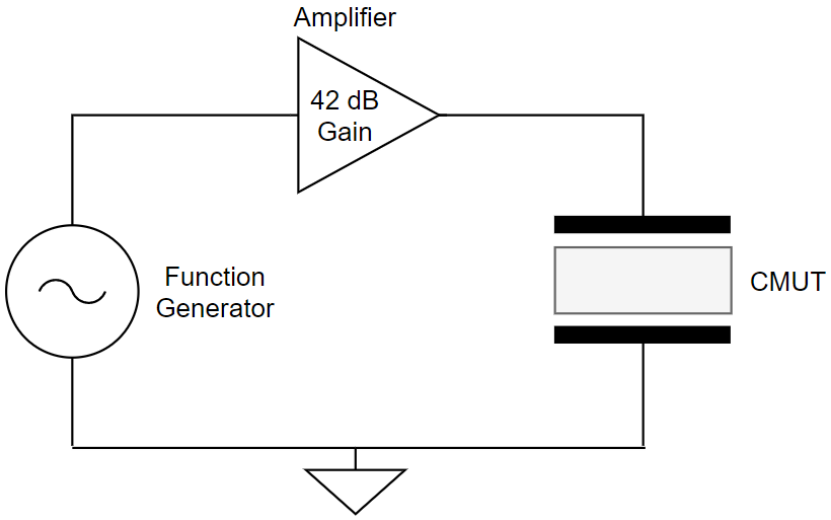

Figure 2.6: The circuit used to discharge the CMUTs

The required AC Voltage to dis-charge a CMUT is determined by the Voltage at which a charging effect starts taking place within the CMUT. The signal used in this work to dis-charge the CMUTs is a 50% symmetric saw-tooth AC Voltage with a peak-to-peak value of 157 V at a frequency of 200 Hz.

2.1.4. Estimating the Amount of Trapped Charge

The amount of trapped charge $Q_{trapped}$ in the layer of Al_2O_3 can be estimated by comparing the charge distribution of a charged CMUT to the charge distribution of the same CMUT under a range of bias voltages. If it is known under which external bias voltage the CMUT has the same behaviour as its charged variant, one can determine the amount of charge trapped in the Al_2O_3 layer that is needed to collapse the membrane of the CMUT similarly, as is shown in figure 2.7.

$$Q_{trapped} = Q_1 + Q_2 \tag{2.1}$$

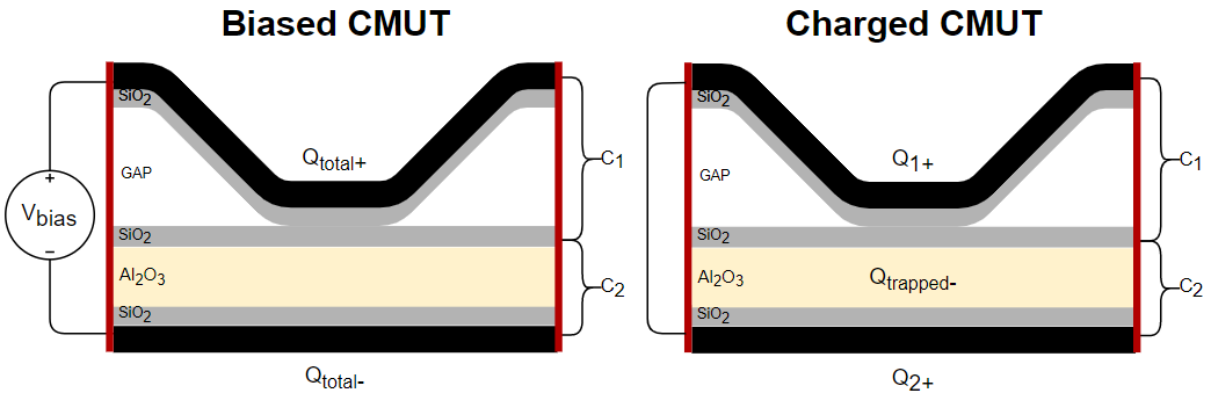

Figure 2.7: A CMUT under an external bias voltage and a charged CMUT

First, the total charge Q_{total} is estimated through determining the equivalent bias voltage V_{bias} and the total capacitance C_{total} of the electrical equivalent of the CMUT (figure 1.6).

$$Q_{total} = V_{bias} C_{total} \tag{2.2}$$

where:

$$C_{total} = C_m + \frac{C_1 C_2}{(C_1 + C_2)} \tag{2.3}$$

The equivalent bias voltage V_{bias} is determined by matching the impedance spectrum of the charged CMUT to a range of impedance spectra of the same biased CMUT using an R-Squared estimation. In figure 2.8 an 'equivalent bias voltage estimation' is shown for the spectrum of the P67 charged for 0.1 s at 175 V, resulting in an equivalent bias voltage of 50 V (97% fit). The comparison between the CMUT under bias voltage V_{bias} and its charged twin is valid as long as the applied bias-voltage is lower than the voltage under which charge is injected into the Al_2O_3 layer.

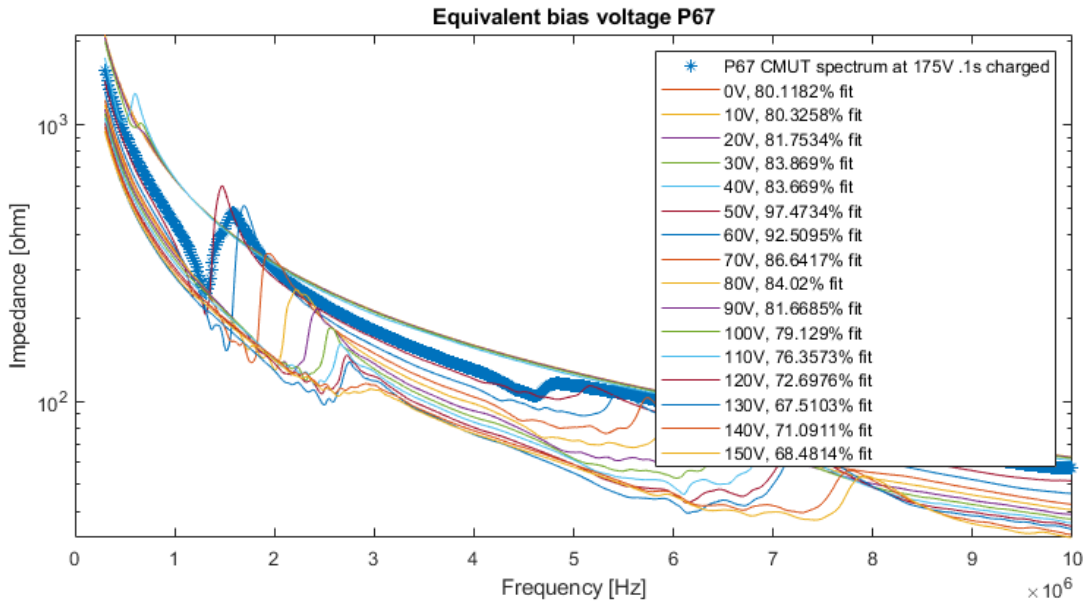

Figure 2.8: The spectra of a charged CMUT compared to the spectra of the CMUT under a range of bias-voltages

To estimate the value of the capacitance C_{total} the spectra of a range of capacitors with interval steps of 1 pF were fitted to the retrieved spectra of the CMUT up till the resonance frequency using an R-squared estimation. In figure 2.9 an example is shown of three capacitor values fitted to the spectrum of a charged CMUT, indicating C_{total} is approximately 340 pF (99% fit).

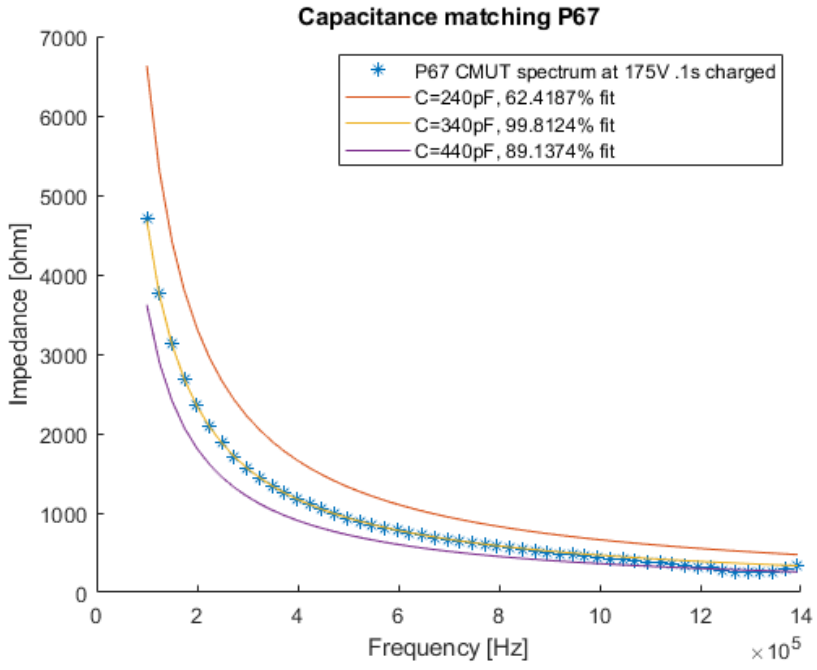

Figure 2.9: The spectrum of the charged CMUT up to its first resonance frequency compared to the spectra of a range of capacitance values

With V_{bias} and C_{total} known, Q_{total} can be calculated using equation 2.2. For the biased CMUT, the total charge Q_{total} is distributed over the top and bottom electrodes.

For the trapped charge CMUT, no bias voltage V_{bias} is applied (V_{bias} = 0 V). The trapped charge $Q_{trapped}$ will therefor distribute over C_1 and C_2 and result in Q_{1+} and Q_{2+}. Since C_1 and C_2 are in parallel, the voltage over C_1 and C_2 is equal, and the following applies:

$$\frac{Q_1}{C_1} = \frac{Q_2}{C_2} \tag{2.4}$$

When the impedance spectra between the trapped-charge and biased CMUT are equivalent, the membrane is deformed similarly. This implies that the charge over C_1 in the charged state must match the amount of charge over C_{total} when an external bias voltage is applied, meaning $Q_1 = Q_{total}$. Then, Q_2 can be determined as:

$$Q_2 = \frac{Q_1}{C_1} C_2 = \frac{Q_{total}}{C_1} C_2 \tag{2.5}$$

The capacitance C_1 is variable and changes when the membrane (top electrode) is subjected to the electrostatic force induced by an applied bias voltage or charge trapped into the Al_2O_3 layer. The capacitance C_2 is static and can be calculated by using

$$C_2 = N\varepsilon_0\varepsilon_{sio_2}\frac{\pi r^2}{d_{sio_2}}[F] \tag{2.6}$$

where:

N = the number of drums (membranes)
ε_0 = the dielectric constant of a vacuum
$\varepsilon_{\mathrm{sio_2}}$ = the dielectric constant of SiO_2
r = the radius of a drum membrane
d_{sio_2} = the layer thickness of the bottom dielectric

When utilising 336 drums, all with a radius of 67.5 µm, and a bottom dielectric of 50 nm, C_2 becomes approximately 3.3 nF. Using the obtained C_2 and assuming $C_m << C_{total}$, C_1 can then be determined by:

$$C_1 = \frac{C_2 C_{total}}{C_2 - C_{total}} \tag{2.7}$$

With the total amount of charged trapped inside the Al_2O_3 layer resulting in

$$Q_{trapped} = Q_{total} \times (1 + \frac{C_2}{C_1}) \tag{2.8}$$

2.1.5. Matching and Rectification

The electrical equivalent model of a CMUT (as can be seen in figure 1.6) reduces to the electrical model in figure 2.10 when operated at its resonance frequency.

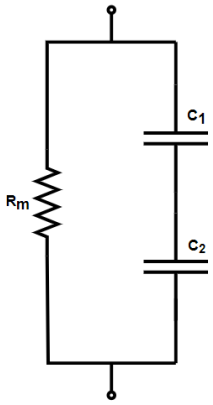

Figure 2.10: Electrical equivalent of a CMUT when operated at its resonance frequency

The by the CMUT harvested mechanical ultrasound energy (figure 2.16) is converted to the electrical domain and outputted as an AC voltage. Matching and rectification are done to maximise the harvested AC voltage and to rectify the AC voltage into a DC voltage. The circuit used to match and rectify the raw AC voltage coming from the output of the CMUT can be seen in figure 2.11.

To maximise the AC voltage V_0 at the output of the CMUT, the capacitive values of C_1 and C_2 (figure 2.10) of the CMUT are compensated with an inductance. The value of the inductance needed depends on the charged state of the CMUT and is therefore made variable so that the output at V_1 can be maximised manually.

The resulting maximised AC voltage V_1 then is rectified to a direct DC voltage V_2, which can then be applied to a connected load. The output power over the load is then maximised employing impedance matching of the CMUT's internal resistance R_m.

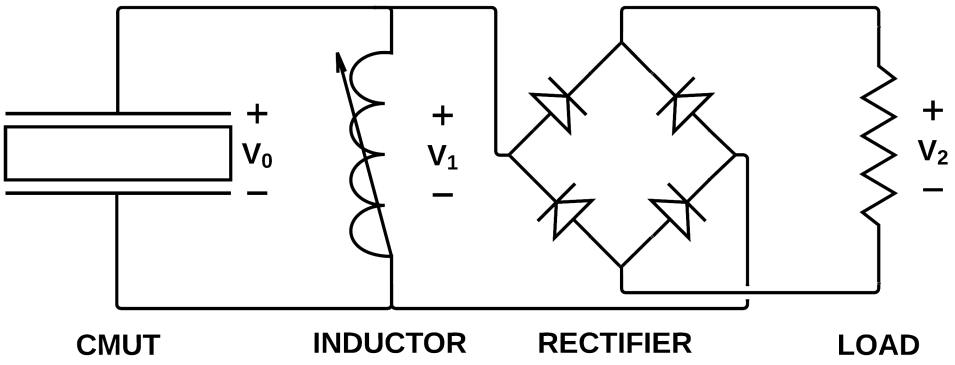

Figure 2.11: The schematic of the matching and rectification circuit

2.2. The Ultrasound Transmitting System

In this Section, the ultrasound transmitting system is elaborated. The system used to direct focused ultrasound to the energy harvester is the Verasonics Vantage.

2.2.1. The Verasonics Vantage

The Verasonics Vantage research ultrasound system (figure 2.12) is a fully programmable system that can be used for all ultrasound applications in research and development. It was programmed in Matlab to send focused ultrasound waves to the energy harvester located within the phantom through beam-steering.

Figure 2.12: The Verasonics Vantage Research Ultrasound System

The Verasonics Vantage is controllable by means of a graphical user interface (GUI) and displays a live ultrasound image generated utilizing conventional B-mode imaging. The GUI and an example of such an ultrasound image can be seen in figure 2.13.

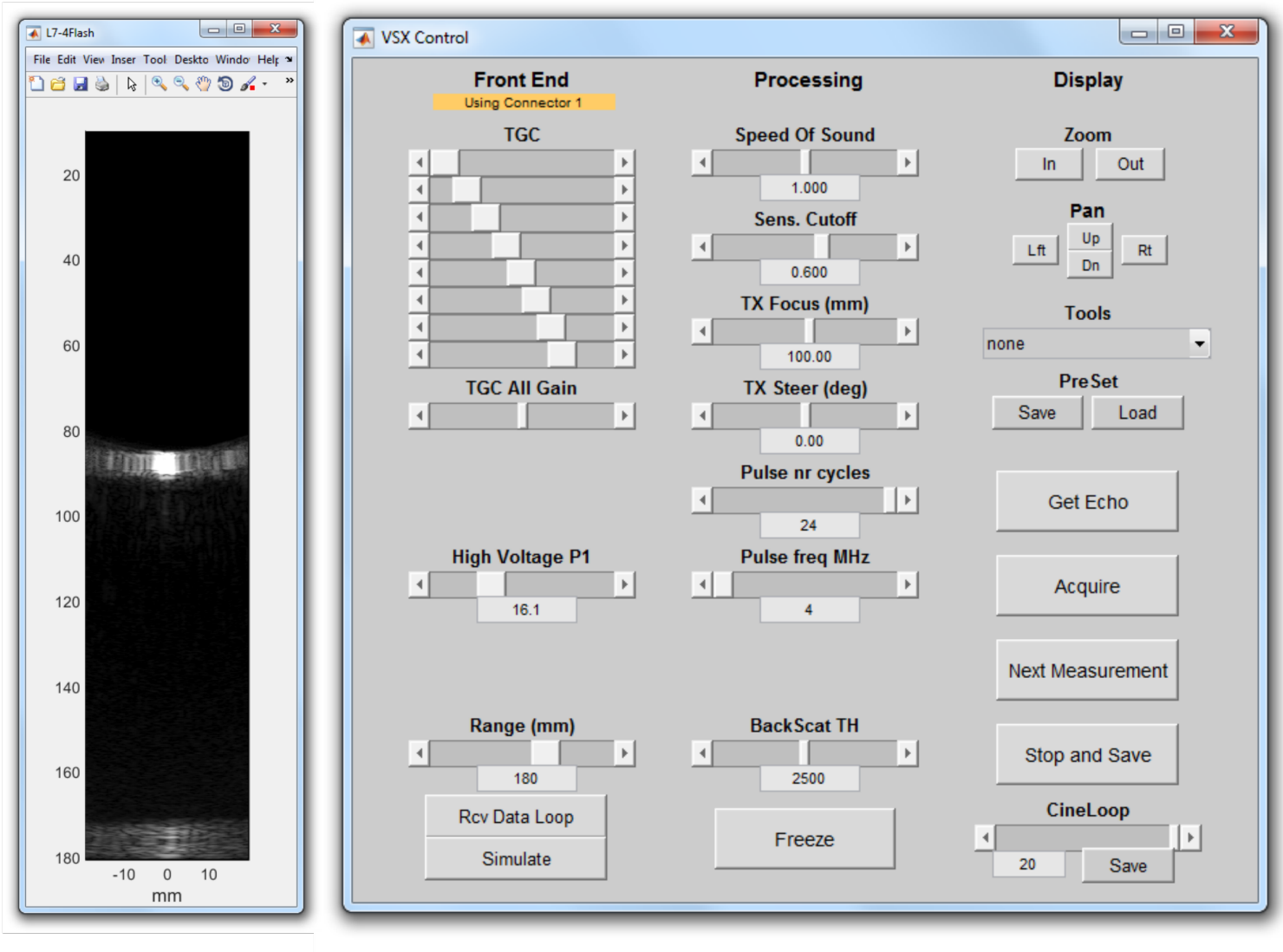

Figure 2.13: The GUI of the Verasonics Vantage

2.2.2. The Probe

The probe chosen for the ultrasound energy transfer experiments is the Philips L7-4 linear array transducer (figure 2.14). Firstly because the frequency bandwidth of the L7-4 overlaps with the frequency bandwidth of the used CMUT devices, and secondly because the L7-4 is completely medically certified and fulfills the safety requirements of the use of ultrasound within the body, and therefore provides for an excellent proof of concept of ultrasound energy transfer for biomedical applications.

The Philips L7-4 medical probe has a frequency range of 4 MHz to 7 MHz. It has 128 elements with a width of 0.283 mm, a height of 7 mm, and a spacing of 25 µm (figure 2.15).

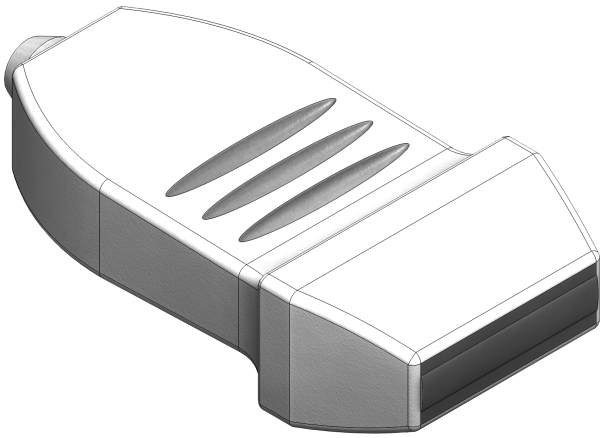

Figure 2.14: The Philips L7-4 linear array transducer

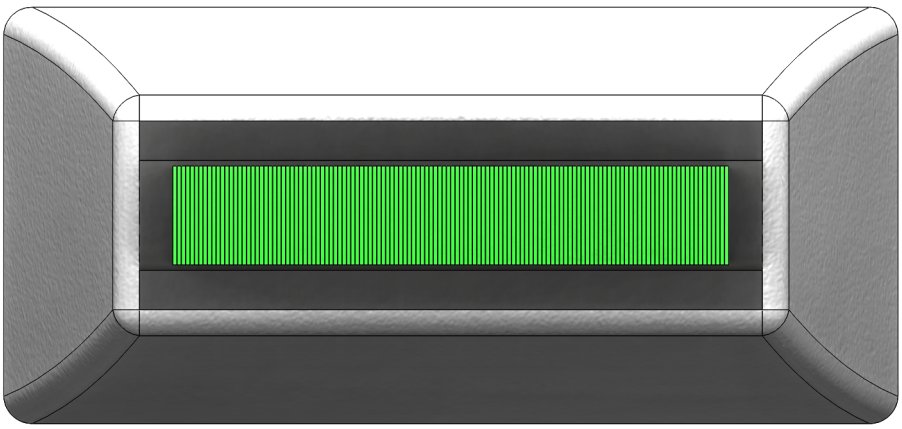

Figure 2.15: The PZT elements of the Philips L7-4 linear array transducer

Using the Verasonics Vantage, a variable probe voltage V_{probe} can be supplied to the L7-4. The maximum probe voltage V_{probe} allowed by the Verasonics Vantage for ultrasound energy transferring purposes is found to be 45 V.

2.2.3. The Ultrasound Energy Carrier

The ultrasound signal used as the energy carrier for the used ultrasound energy transfer set-up is a 24 cycle 4 MHz sine wave, repeated at a maximum repetition frequency of 5 kHz. Figure 2.16 shows a single cycle wave, a 24-cycle burst wave, and the repeated 24-cycle 4 MHz sine wave, which is used as the energy carrier. The number of pulse cycles and the repetition frequency were maximised within the Verasonics system. Longer pulse bursts and higher repetition frequencies could not be achieved with the available equipment.

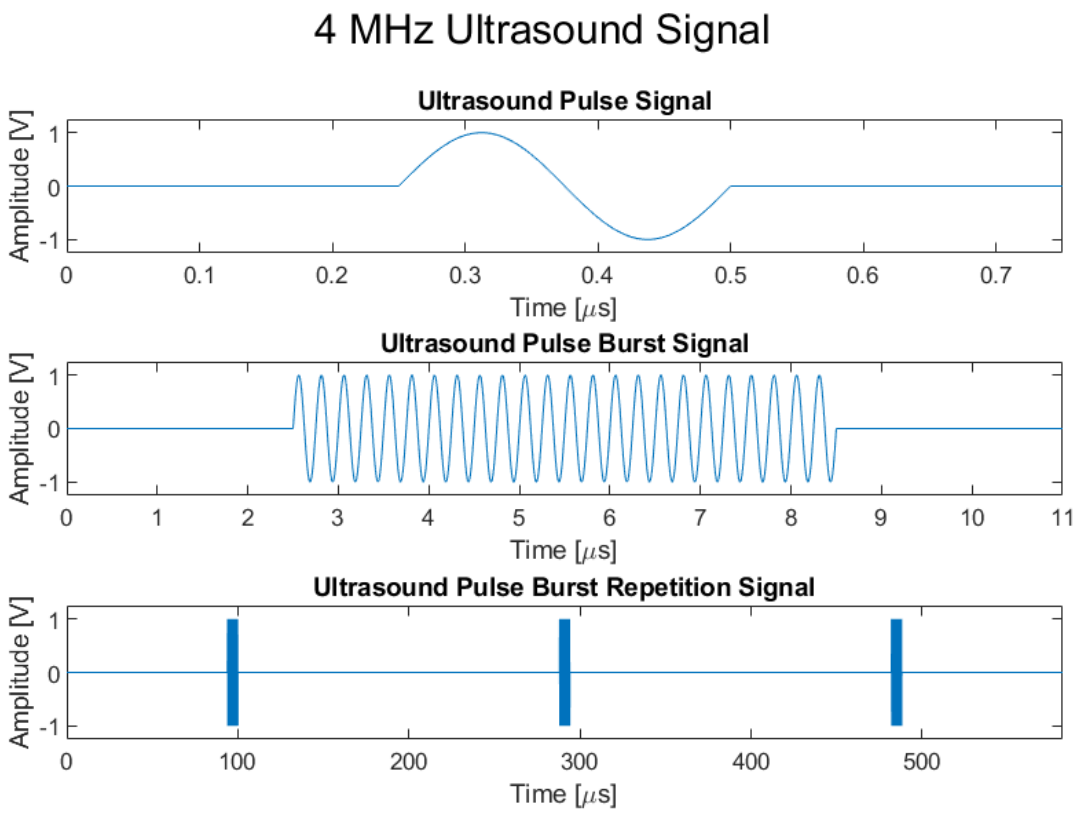

Figure 2.16: The 4 MHz ultrasound energy carrier

The frequency of the ultrasound signal was chosen to be 4 MHz based on the frequency bandwidth of the Philips L7-4 medical imaging probe, and the frequency bandwidth of the receiving charged CMUT ultrasound transducer of the energy harvester. Experimental testing showed that a frequency of 4 MHz resulted in a maximum energy transferring efficiency, and therefore this frequency was used for all the conducted experiments.

2.2.4. Focusing of the Ultrasound Beam

The Verasonics Vantage can focus the ultrasound signals coming from the L7-4 Philips linear array ultrasound transducer's individual elements by applying small delays between the pulses applied to the individual elements; a technique called beam-forming. Using beam-forming, the focal point of the L7-4 probe can be placed anywhere in the top-plane. Using the ultrasound energy transfer set-up, the focal point was placed on the active elements of the CMUT, as shown in figures 2.17 and 2.18. The focus point as seen from the side in figure 2.18 is fixed and determined by the shape of the individual PZT elements of the L7-4 probe (figure 2.15). Simulations regarding the focal point of the focused L7-4 are done in FOCUS (Fast Object-oriented C++ Ultrasound Simulator), an ultrasound simulation tool provided by Michigan State University.

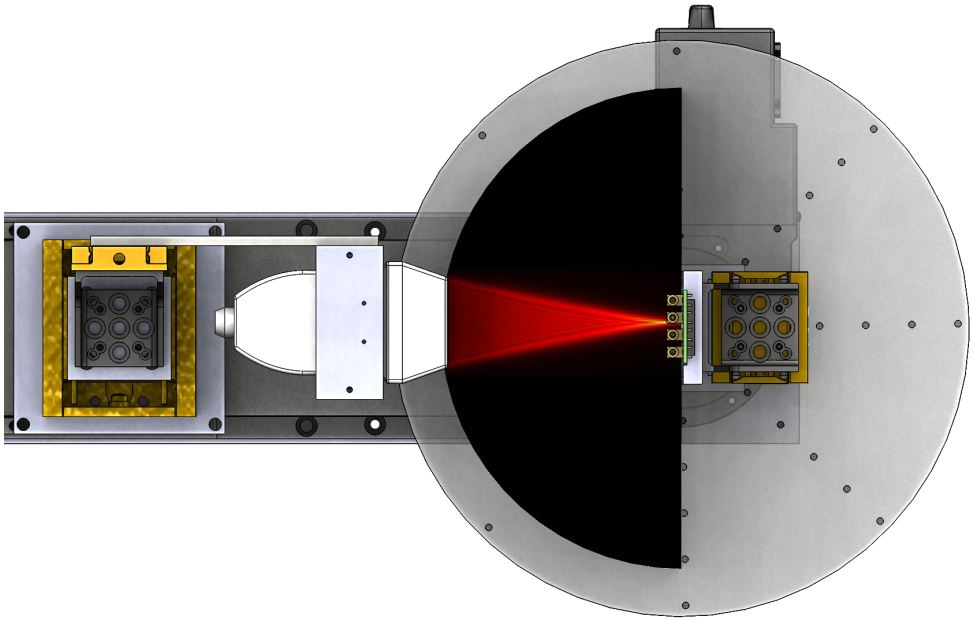

Figure 2.17: Top view of an ultrasound beam focused upon the CMUT

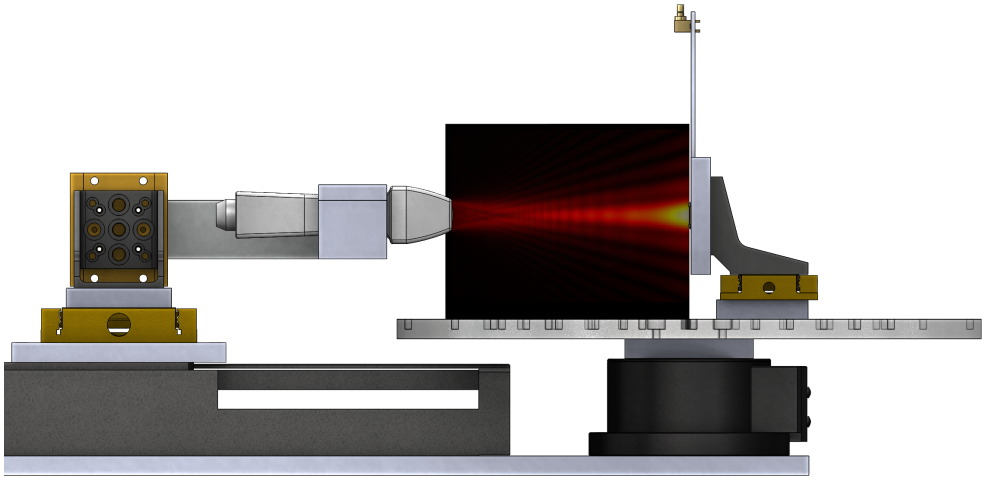

Figure 2.18: Side view of an ultrasound beam focused upon the CMUT

2.3. The Experimental Set-up

The designed and fabricated experimental set-up contains several functionalities that allow for various ultrasound energy transfer experiments.

First of all, the distance between the probe and CMUT is made adjustable utilizing a motorised linear stage (the Newport M-ILS250CC). This functionality ensures that mediums of different sizes can be used for the experiments and that the probe can be placed against the medium automatically and kept there steadily without human interference.

Secondly, the relative angle between the probe and the receiving CMUT is made adjustable utilizing a motorised rotational stage (the Newport RVS80CC). The rotational stage rotates the medium and the CMUT with respect to the probe, thereby changing the ultrasound beam's incident angle upon the CMUT. This functionality gives the opportunity to obtain information about the angular acceptance of the CMUT. Both the linear and rotational stages are controlled with the Newport Universal Motor Controller / Driver ESP 300.

Finally, the set-up allows for alignment using micro-manipulators. In an ultrasound energy transfer link, as holds for other wireless energy transferring techniques, alignment between the transmitting transducer and receiving transducer is crucial to maximise the transferring link's efficiency. The set-up contains multiple micro-manipulators to precisely fine-tune the alignment of the transmitting and receiving transducers.

The phantom was made out of gel wax (paraffine gel). The reason for using gel wax is that it has an attenuation coefficient and a sound speed similar to that of soft tissue. Furthermore, it can be moulded into any shape, and it has the advantage over organic-based phantoms that it doesn't deteriorates easily [18] [33].

The full measurement set-up containing the L7-4 probe, a paraffin wax phantom, a CMUT, two motorised stages, and micro-manipulators can be seen in figures 2.19, 2.20 and 2.21.

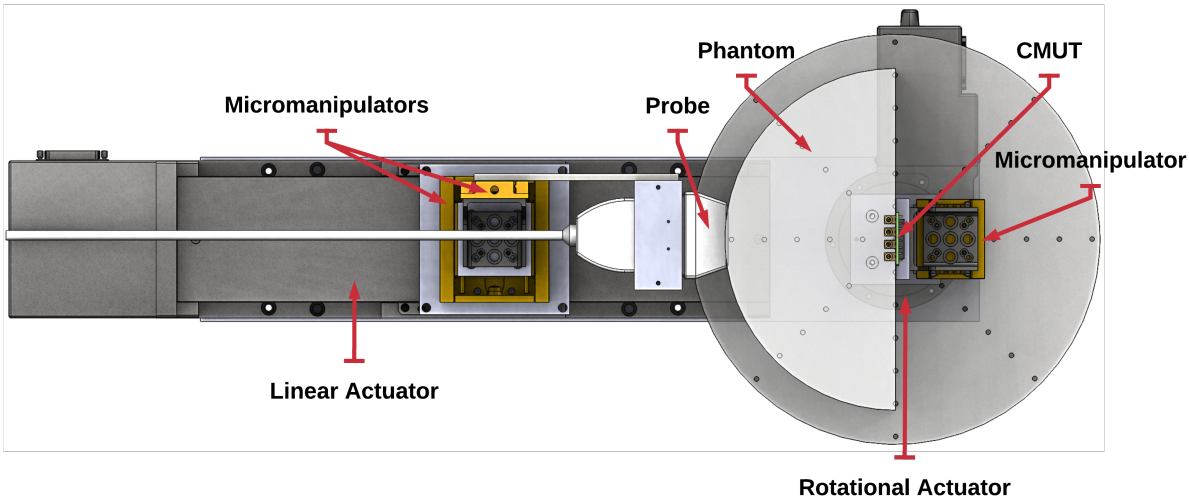

Figure 2.19: Top view of the experimental set-up

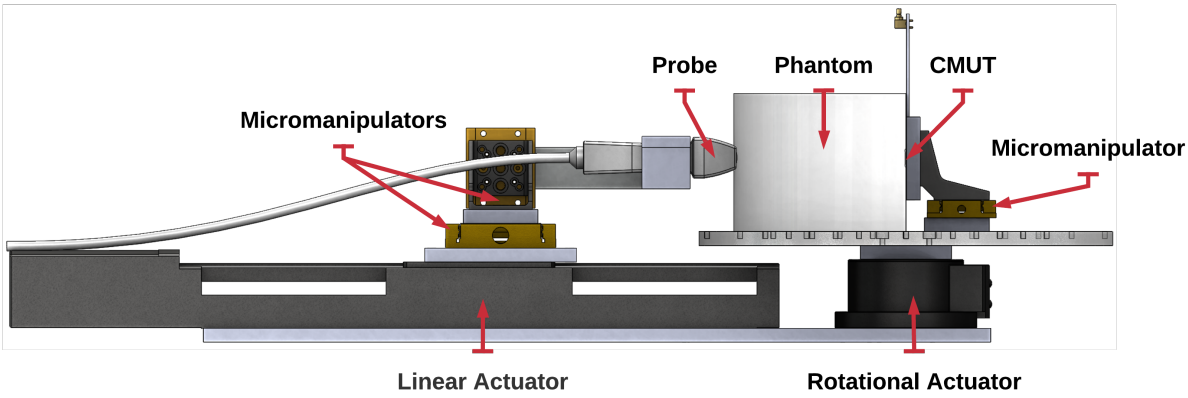

Figure 2.20: Side view of the experimental set-up

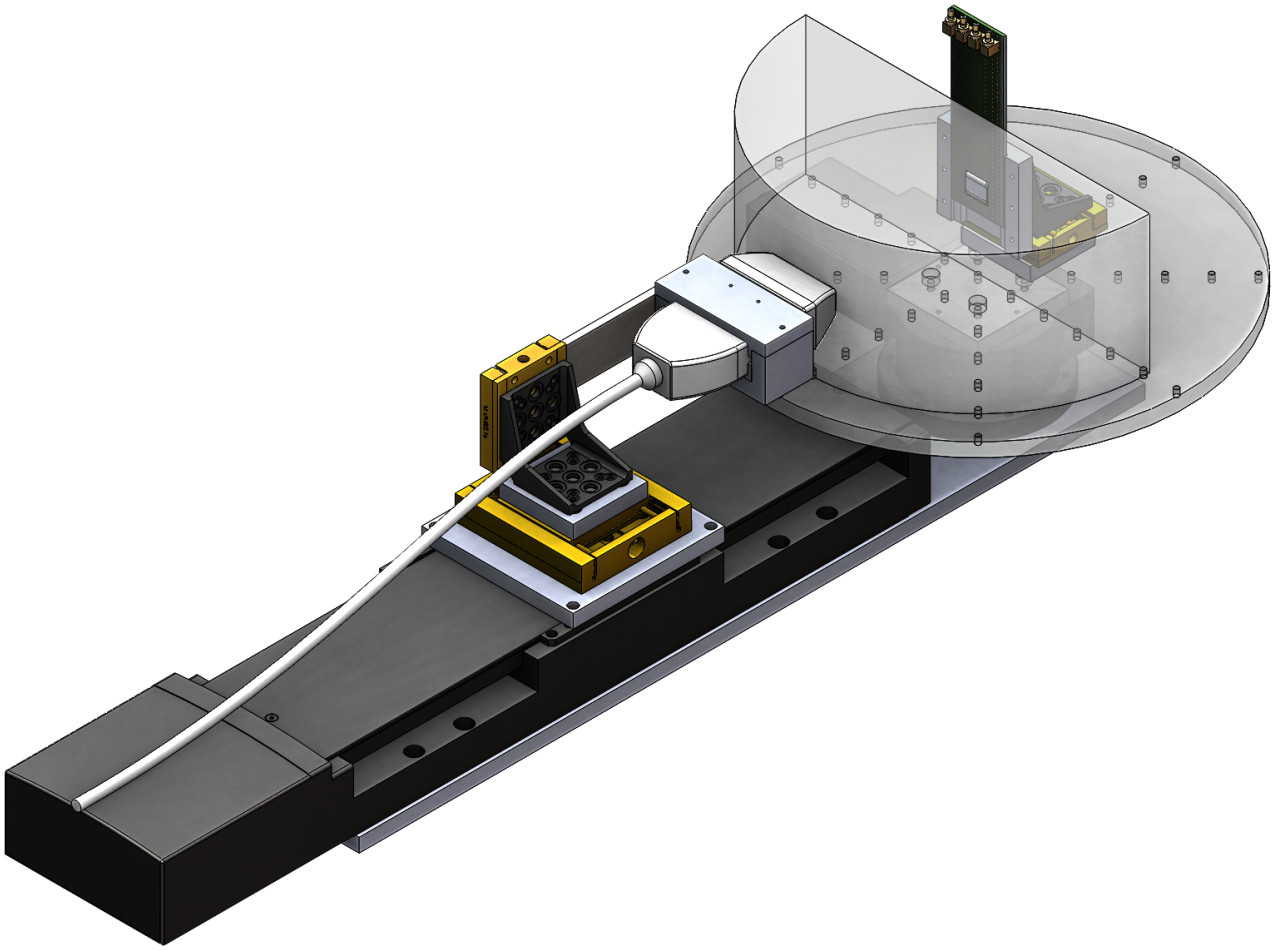

Figure 2.21: Isometric view of the experimental set-up

2.4. System Overview

An overview of the complete system and its information flow can be seen in figure 2.22. The system is programmed in Matlab (a), where both the Verasonics Vantage (b) and the experimental set-up (d) are controlled using scripts, functions, and a graphical user interface. The data-acquisition utilizing an oscilloscope (Agilent Technologies DSO6034A) (g) is also done using Matlab.

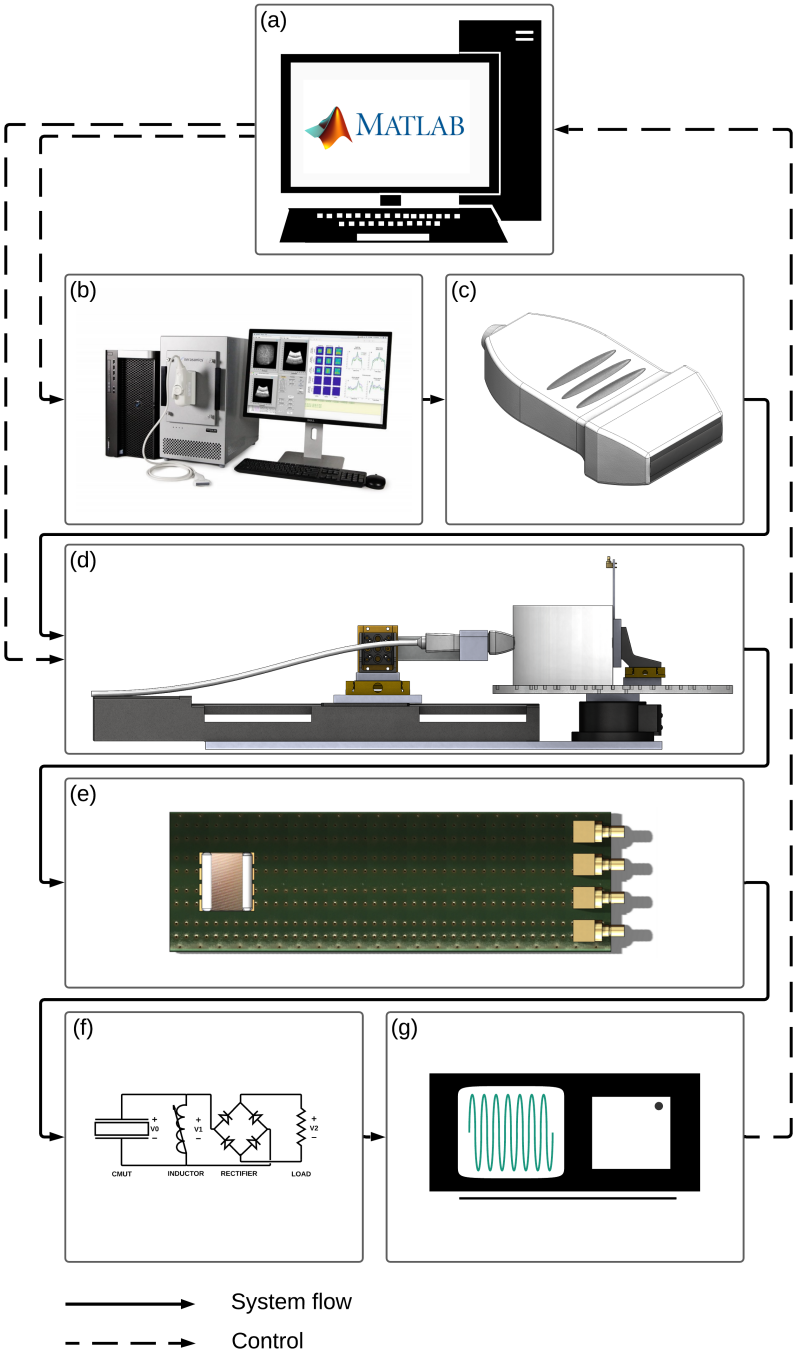

Figure 2.22: System Overview with (a) PC with Matlab, (b) the Verasonics Vantage, (c) the L7-4 probe, (d) the experimental set-up, (e) the CMUT, (f) the matching and rectification circuit and (g) an oscilloscope

3

Results

In this Chapter, results about the charging of the CMUTs, the angular acceptance of the CMUTs, the harvested energy, and its applications can be found.

3.1. Charging of the CMUTs

Three CMUT variants, indicated by $P67$, $P69$ and $P103$, with layer structures as given in table 2.1 were charged according to the method given in Section 2.1.2. After completing each entry of measurement table 2.2, the impedance and phase spectra were measured to determine the resonance frequency, the phase peak, and the amount of trapped charge.

As an example of the obtained data, the impedance and phase spectra of the $P67$ with a charging-Voltage of 175 V are given in figure 3.1. All other impedance and phase spectrum measurements can be found in Appendix A.

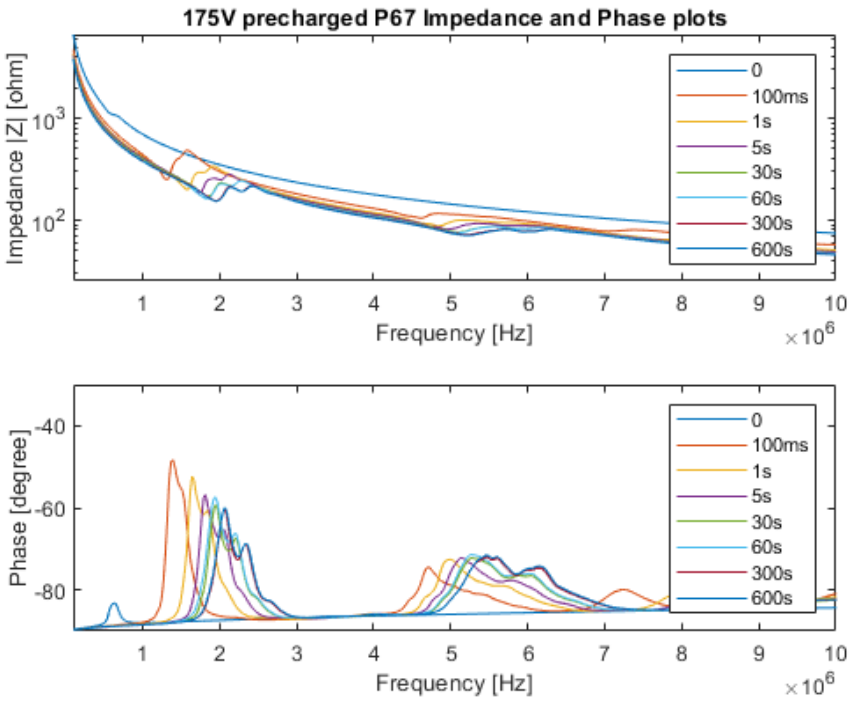

Figure 3.1: The impedance and phase spectra of the $P67$ with a charging-Voltage of 175 V

Charging the CMUTs generally increased the first resonance frequency because the top membrane is increasingly collapsed upon the bottom dielectric, which is caused by the increase in the electrostatic force acting upon the membrane because of the increase in the amount of trapped charges. The more the membrane is collapsed, the smaller the membrane's work area gets, resulting in a higher resonance frequency.

3.1.1. Charging of the P67

In figure 3.2, the resonance frequency as a function of the charging-Voltage and charging-time is given. In figure 3.3, the corresponding phase peaks can be found. In figure 3.4, the estimated amount of trapped charge in the layer of Al_2O_3 is shown.

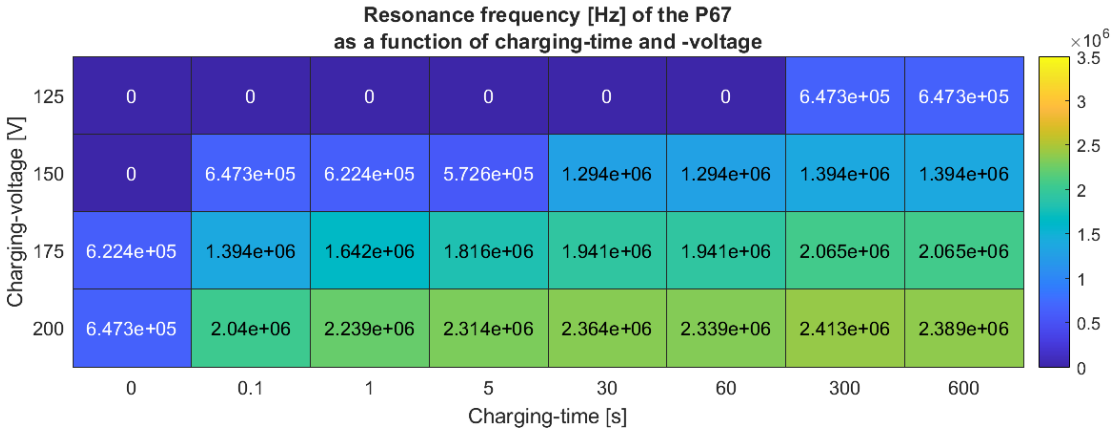

Figure 3.2: Resonance frequencies of the $P67$ as a function of charging-Voltage and charging-time

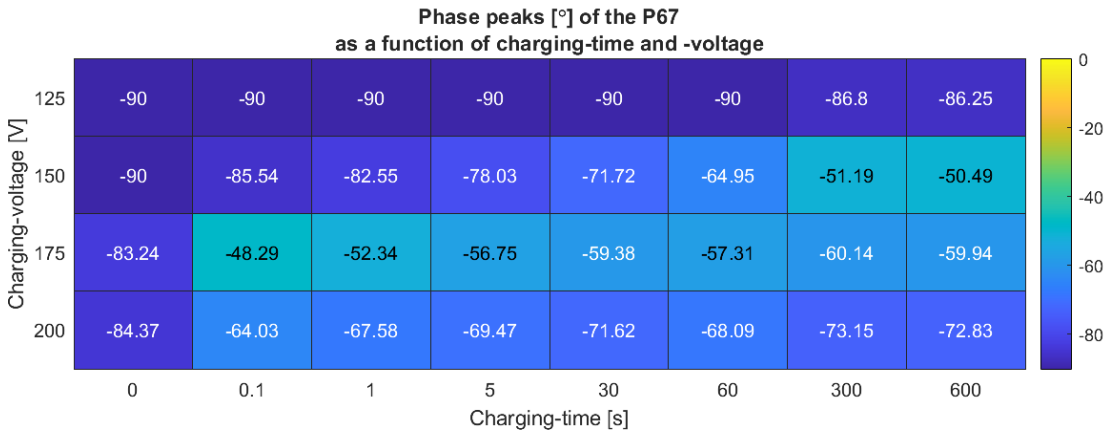

Figure 3.3: Phase peaks of the $P67$ as a function of charging-Voltage and charging-time

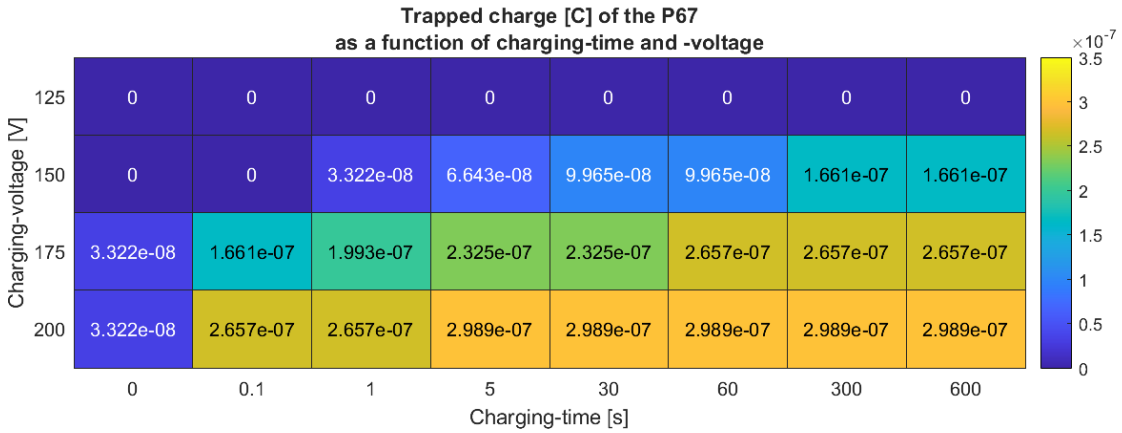

Figure 3.4: Trapped charge of the $P67$ as a function of charging-Voltage and charging-time

Showing from the appearing resonance frequency in figure 3.2, the $P67$ started charging with an applied charging-Voltage of 125 V and higher. From figure 3.3 can be concluded that the $P67$ showed to have its optimum phase after a charging-duration of 0.1 s at a charging-Voltage of 175 V. The trapped charges estimation is based on the equivalent bias Voltage as determined in section 2.1.4, since up to the entry of [1 s 150 V] the equivalent bias Voltage was determined to be 0 V the estimated amount of trapped charges until then is set to 0. While from the resonance frequencies and phase peak values can be concluded that charging starts from [300 s 125 V].

3.1.2. Charging of the P103

In figure 3.5, the resonance frequency as a function of the charging-Voltage and charging-time is given. In figure 3.6, the corresponding phase peaks can be found. In figure 3.7 the estimated amount of trapped charge in the layer of Al_2O_3 is shown.

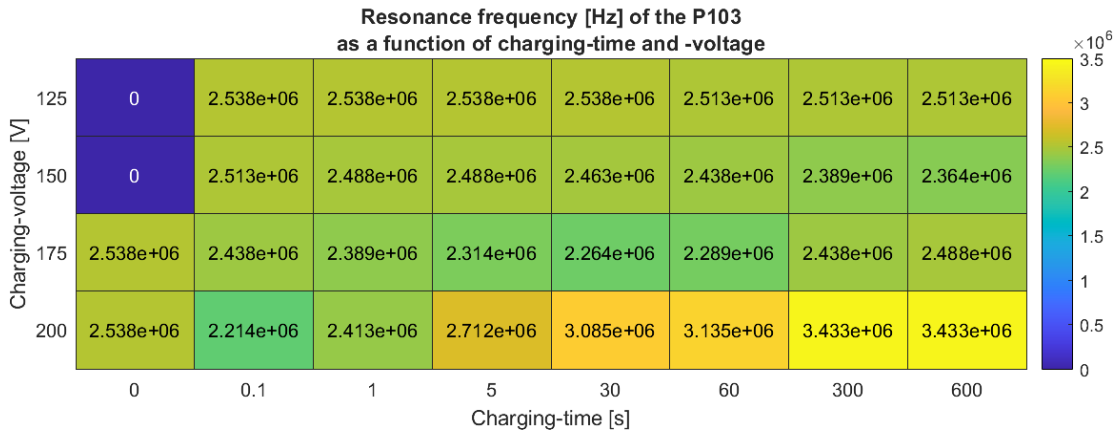

Figure 3.5: Resonance frequencies of the $P103$ as a function of charging-Voltage and charging-time

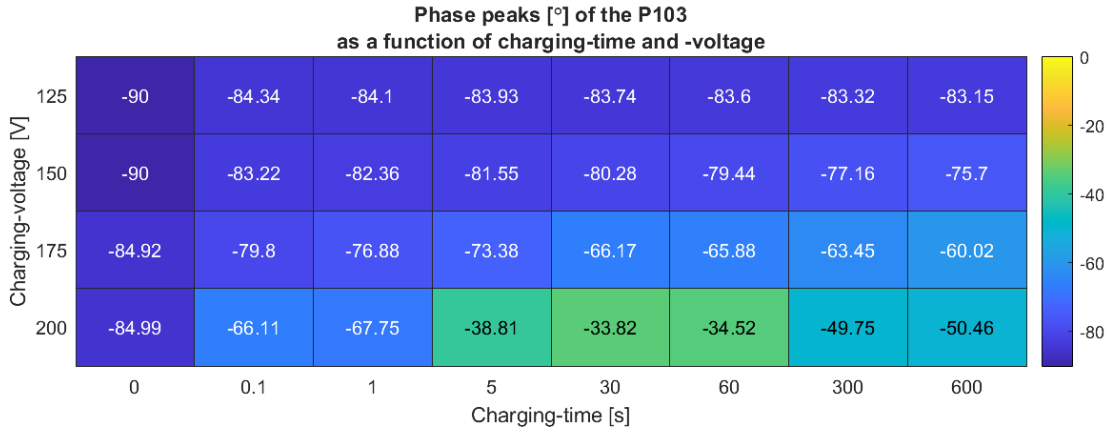

Figure 3.6: Phase peaks of the $P103$ as a function of charging-Voltage and charging-time

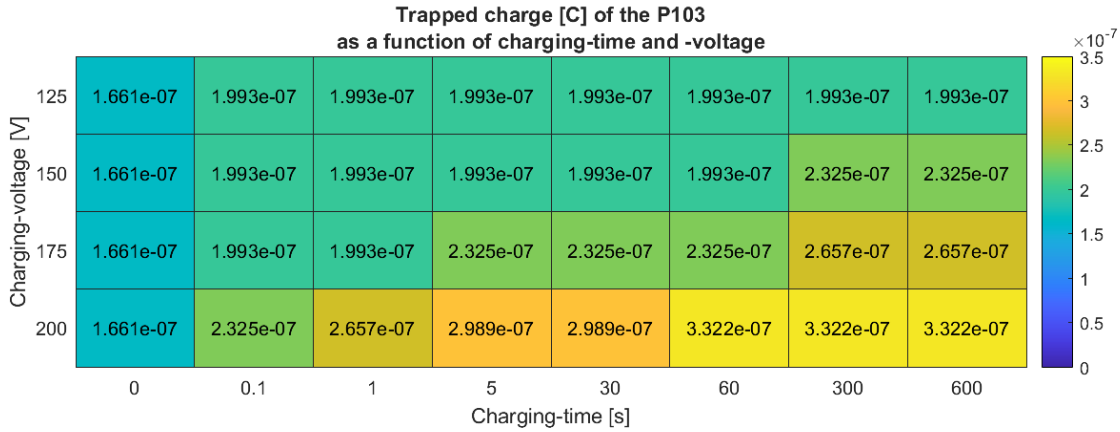

Figure 3.7: Trapped charge of the $P103$ as a function of charging-Voltage and charging-time

Showing from the appearing resonance frequency in figure 3.5, the $P103$ started charging with an applied charging-Voltage of 125 V and higher. From figure 3.6 can be concluded that the $P103$ showed to have its optimum phase after a charging-duration of 30 s at a charging-Voltage of 200 V. The trapped charges estimation is based on the equivalent bias Voltage as determined in section 2.1.4. Since the $P103$ was charged and discharged before this measurement, the equivalent bias Voltage was already

determined to be 50 V without charging because of leftover charge. Since the CMUTs examined in this report are designed for a maximum bias-Voltage of 200 V, and the optimal charging-Voltage was determined to be 200 V, it was decided not to use the $P103$ for the ultrasound energy transfer set-up to avoid breakdown of the device.

3.1.3. Charging of the P69

In figure 3.8, the resonance frequency as a function of the charging-Voltage and charging-time is given. In figure 3.9, the corresponding phase peaks can be found. In figure 3.10, the estimated amount of trapped charge in the layer of Al_2O_3 is shown.

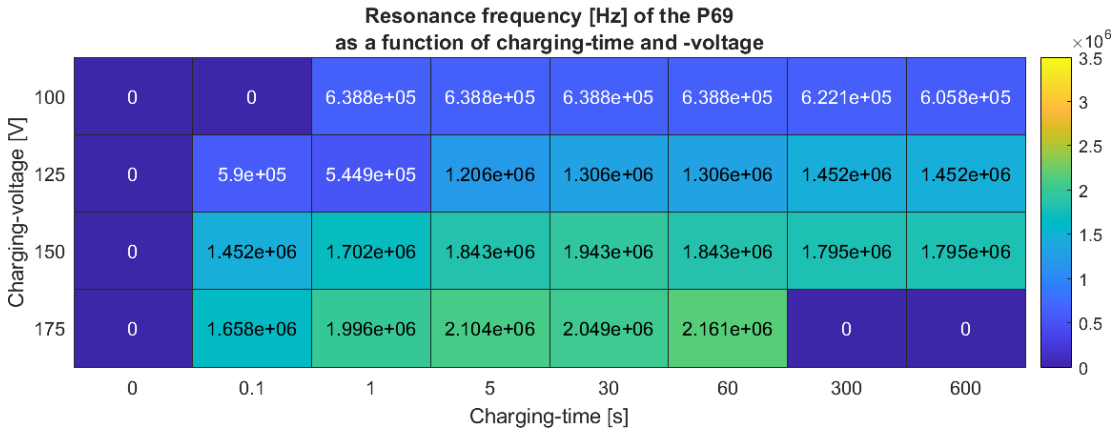

Figure 3.8: Resonance frequencies of the $P69$ as a function of charging-Voltage and charging-time

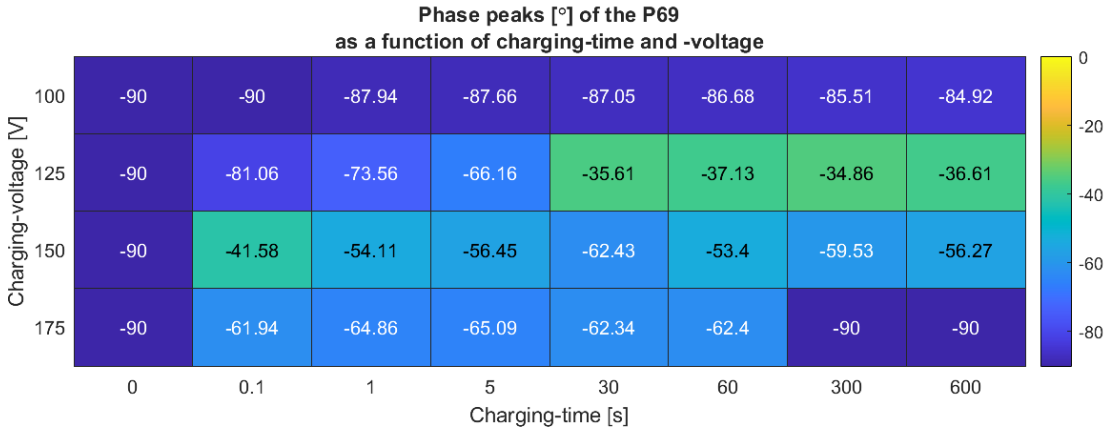

Figure 3.9: Phase peaks of the $P69$ as a function of charging-Voltage and charging-time

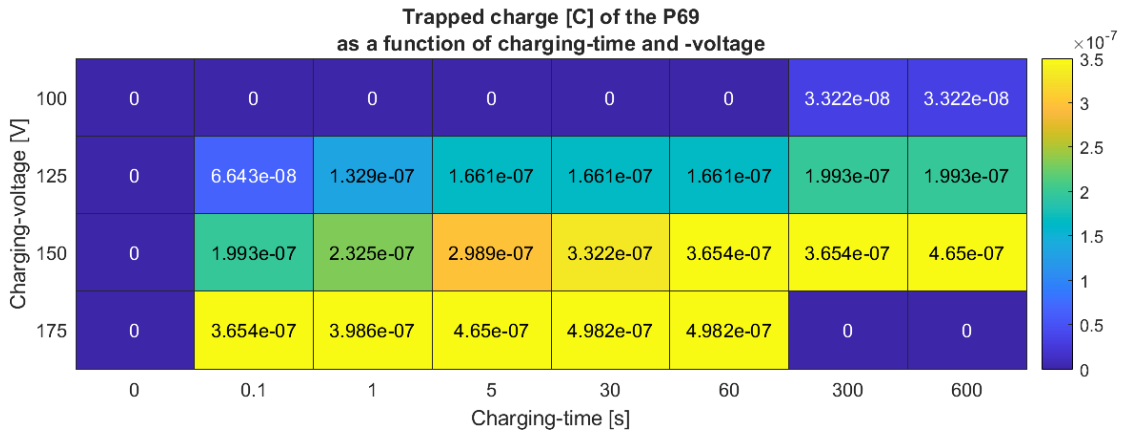

Figure 3.10: Trapped charge of the $P69$ as a function of charging-Voltage and charging-time

Showing from the appearing resonance frequency in figure 3.8, the $P69$ started charging with an applied charging-Voltage of 100 V and higher. From figure 3.9 can be concluded that the $P69$ showed to have its optimum phase after a charging-duration of 300 s at a charging-Voltage of 125 V. The trapped charges estimation is based on the equivalent bias Voltage as determined in section 2.1.4. Since the $P69$ broke on several occasions due to the dielectric breakdown of the thinner dielectric layers in its layer structure during the charging process, it was decided not to use the $P69$ for the ultrasound energy transfer set-up to avoid breakdown of the device.

3.1.4. The Chosen CMUT

The $P67$ being reliable and easy to charge, it was chosen to use the $P67$ in the ultrasound energy transfer experiments. The charged area of the used CMUT is 1.96 mm^2 (0.28 mm×7 mm) and is visible by the eye due to the light reflections induced by the collapsed drums. Figure 3.11 shows the $P67$, and when carefully looked at, the charged lines of CMUT drums can be seen too.

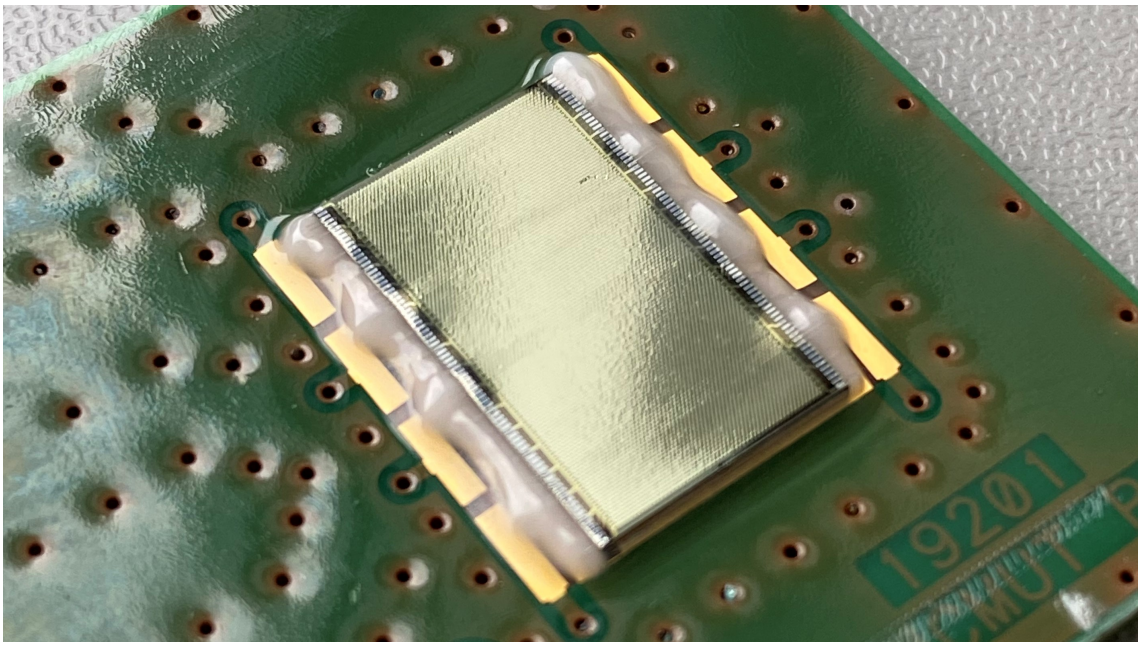

Figure 3.11: The $P67$ and its charged CMUT drums

Since the impedance and phase spectrum measurements were done in air, an additional hydrophone measurement was done to find the resonance-frequency and bandwidth of the $P67$ in water. The result of this hydrophone measurement can be found in figure 3.12. The resonance frequency of the $P67$ in water is about 4.73 MHz with a -3 dB bandwidth of 3.6 MHz to 5.9 MHz.

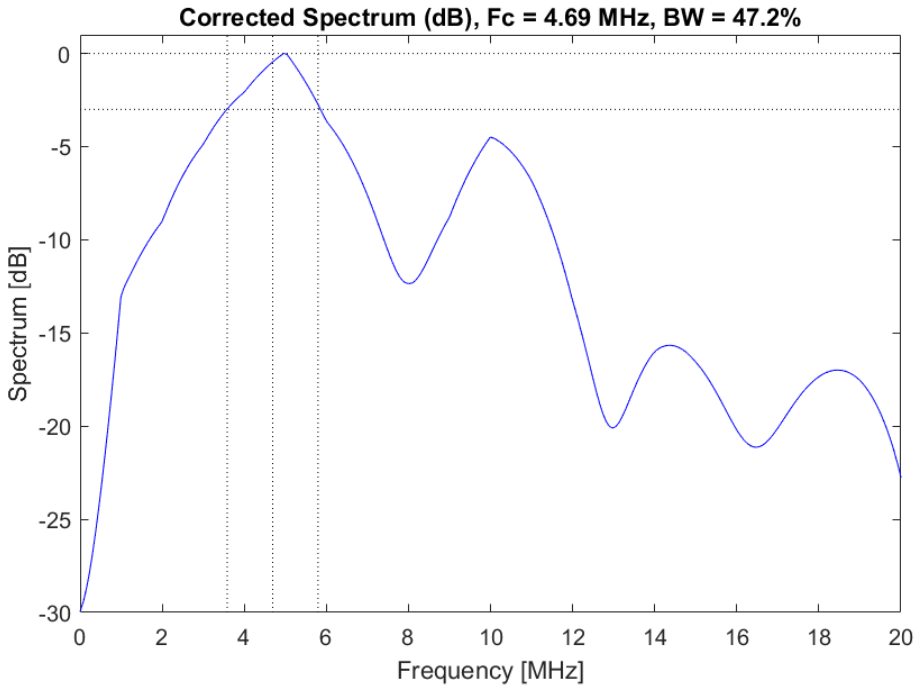

Figure 3.12: The bandwidth of the $P67$ in water

3.2. Energy Transmission

3.2.1. The Ultrasound Energy Transfer System

The complete system used to conduct the ultrasound energy transfer experiments, including the Verasonics Vantage, the experimental set-up, the matching circuit, and a variable load resistor, is shown in figure 3.14. A close-up of the probe, phantom, and CMUT can be found in figure 3.13.

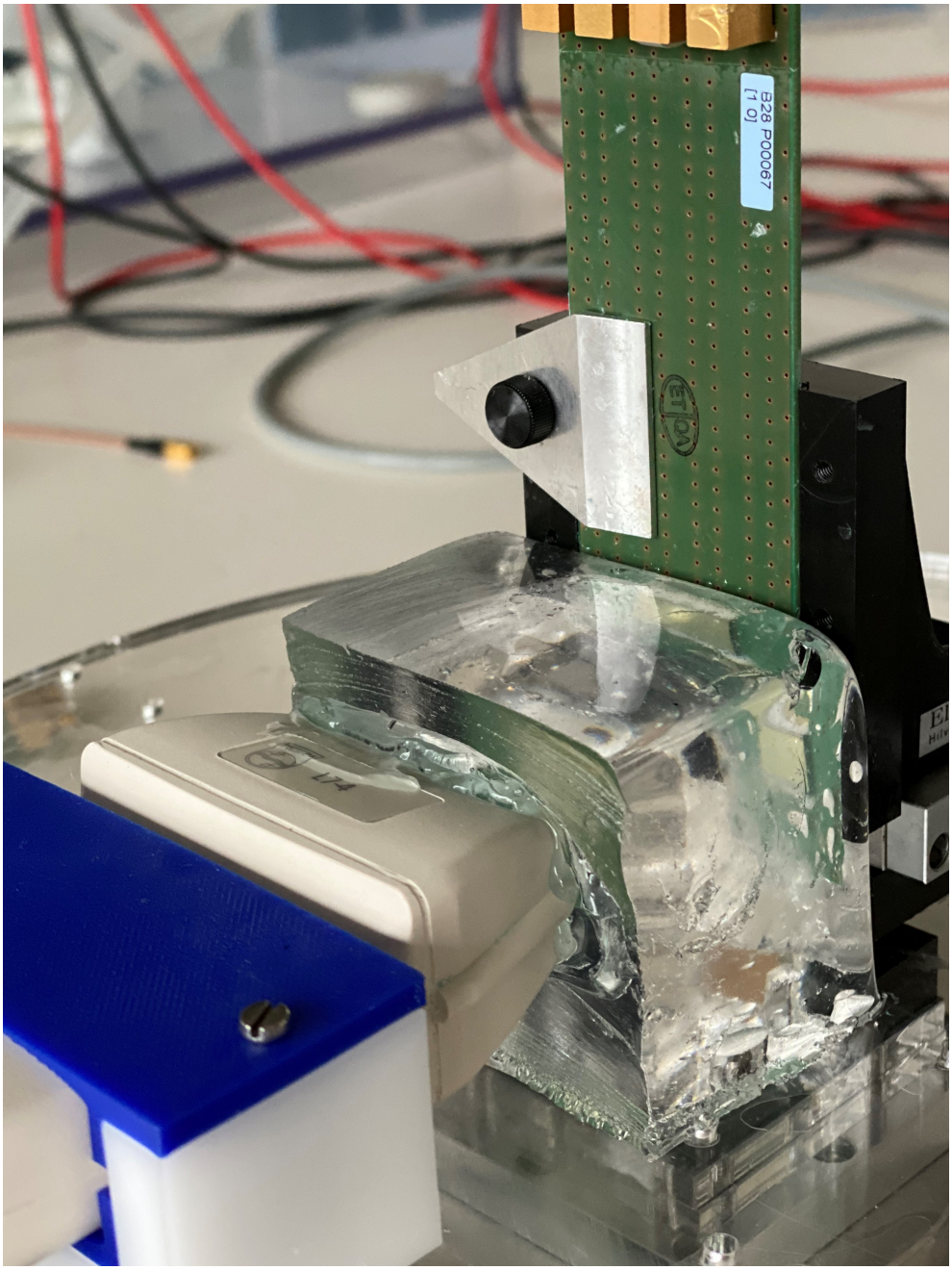

Figure 3.13: The probe, phantom and CMUT

Figure 3.14: The Ultrasound Energy Transfer System

3.2.2. Alignment of the System

Alignment is an essential part of the ultrasound energy transfer system. Improper alignment of the ultrasound transmitting probe and the ultrasound receiving CMUT will result in ultrasound power being lost and lowers the total system efficiency. Three variables are important to attain an alignment in which the power harvested by the CMUT is maximised.

1. The distance between the probe and CMUT; the *transfer distance*
2. The distance of the focus as seen from the probe; the *focus distance*
3. The angle of the focus as seen from the probe; the *focus angle*

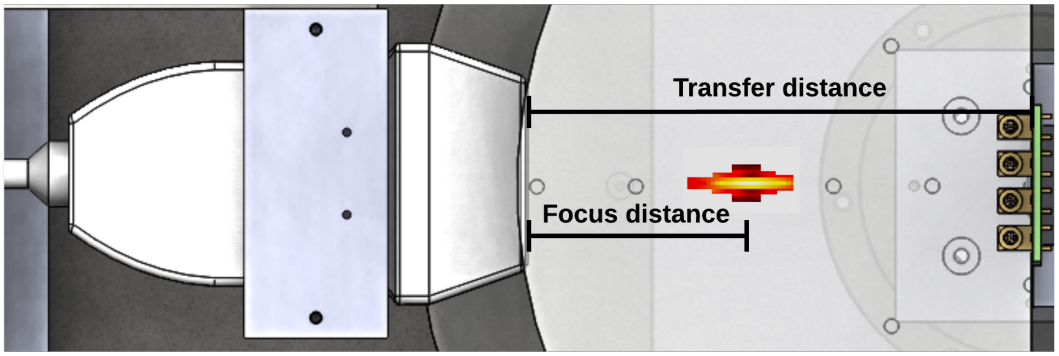

Figure 3.15: The transfer distance and the focus distance

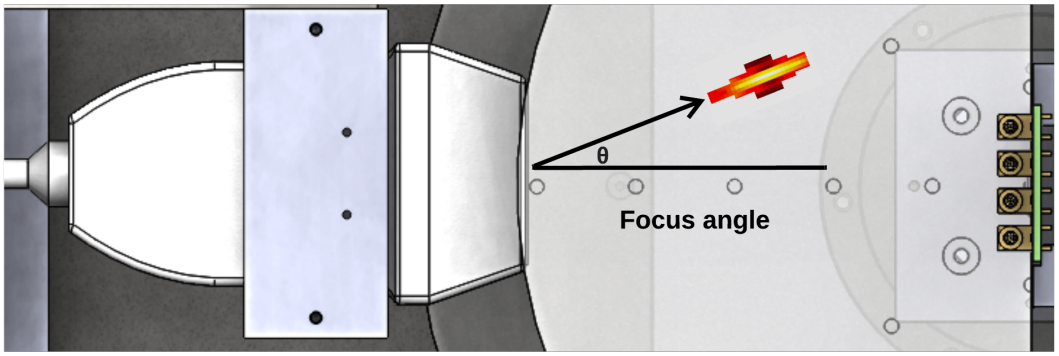

Figure 3.16: The focus angle

First, the transfer distance (see figure 3.15) at which the ultrasound power is most efficiently targeted on the CMUT was searched for. Since the L7-4 is a linear array probe, it can only focus on the top-plane using beam-forming as shown in figure 2.17. In the side-plane, it has a natural focusing effect induced by the shape of the individual PZT elements, as shown in figure 2.18. Therefore, the distance at which the probe is placed from the CMUT determines the shape and intensity of the focal point targeted at the CMUT.

To determine from what transfer distance focusing the ultrasound beam of the L7-4 upon the CMUT (as shown in figure 2.17) would result in the highest harvested output power, a measurement was done in which the transfer distance was stepped from 40 mm to 140 mm in steps of 20 mm. To conduct this experiment, the phantom was shortened by 20 mm for every measurement by means of physically cutting it. Therefore only a limited number of transfer distances were explored.

To validate the measurement, a simulation was performed in which the transfer distance was stepped from 0 mm to 175 mm with steps of 25 mm. The simulated normalised acoustic intensities at the surface of the CMUT (with a width of 0.28 mm and a height of 7 mm) for each of these transfer distances are shown in figure 3.17. Where the surface area of the receiving CMUT is

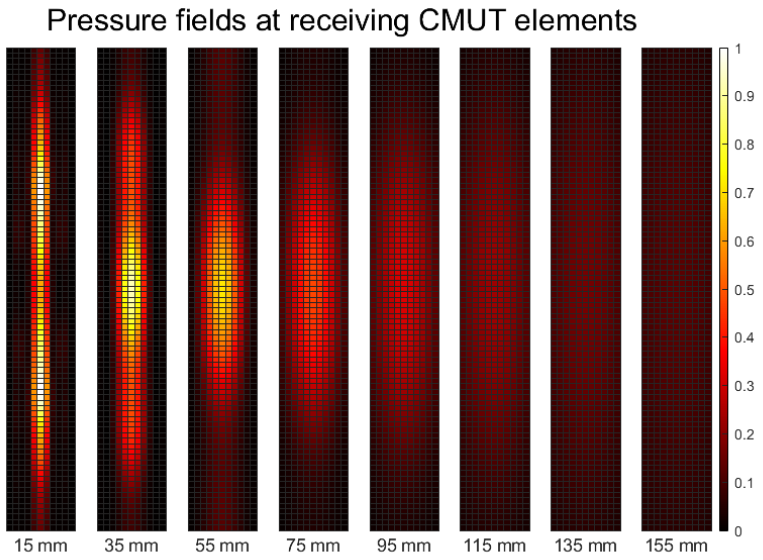

Figure 3.17: The simulated normalised acoustic intensities at the surface of the CMUT for each of the transferring distances

In figure 3.18, both the measurement and simulation results for the transfer distance are plotted. From the measurement, it can be concluded that a distance of approximately 100 mm between the probe and CMUT resulted in the highest outputted power. However, the simulation results showed that a transferring distance of 35 mm to 55 mm would be the most beneficial. The discrepancy between the measurement and simulation results is possibly a consequence of destructive interference caused by reflections of the probe and CMUT.

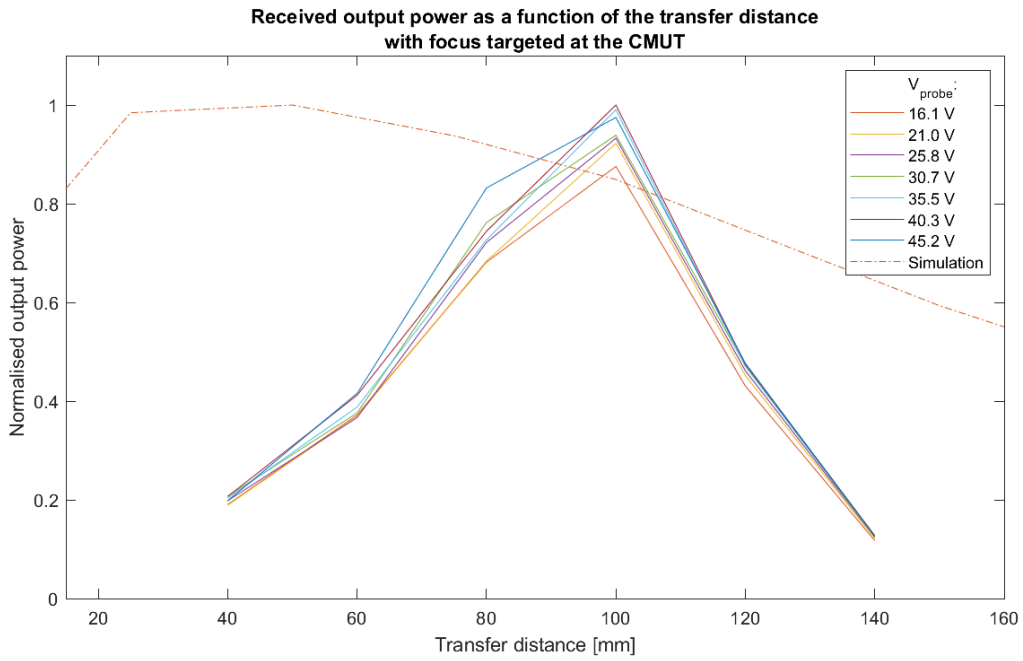

Figure 3.18: Normalised output power as a function of the transfer distance

Secondly, the focus distance was explored. The ultrasound beam's focus distance affects the amount of area of the receiving transducers radiated with mechanical (ultrasound) power. A focus distance of 100 mm implies the focal point is located at 100 mm from the transmitting transducer and that the radiated incident area at this distance is the smallest with the highest power per square area (figure 3.15).

To test whether a trade-off exists between the radiated incident area and the radiated power per square area (see figure 3.19), the focal point of the ultrasound beam was stepped from 70 mm to 130 mm with steps of 2 mm while keeping the transfer distance between the probe and CMUT constant at 100 mm to check for a maximum in the harvested signal.

To validate the measurements, a simulation was performed in which the focus distance was stepped from 70 mm to 130 mm with steps of 2 mm. The simulated normalised acoustic intensities at the surface of the CMUT for each of these focal distances can be seen in figure 3.19.

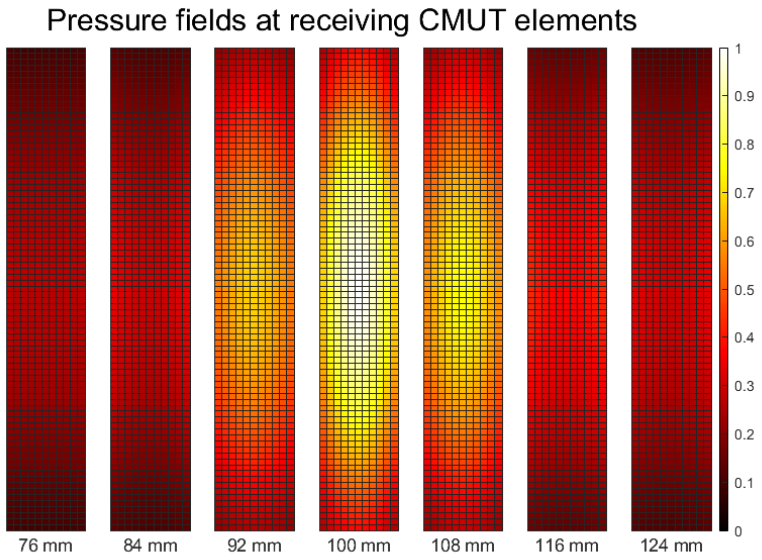

Figure 3.19: The simulated normalised acoustic intensities at the surface of the CMUT for some of the focus distances

In figure 3.20, both the measurement and simulation results for the focus distance are plotted. The obtained measurement data and the simulation results match very closely, meaning it can be said with certainty that to maximise the output power at a distance of 100 mm it is best to place the focal point at this same distance.

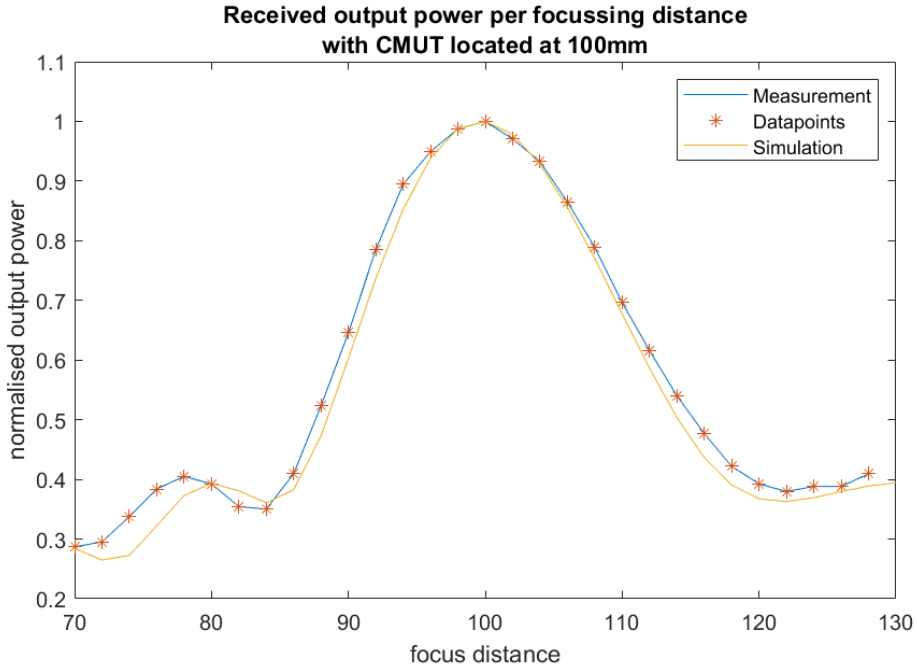

Figure 3.20: Normalised output power as a function of the focus distance with a CMUT located at 100 mm

Lastly, an experiment was done in which the focus point was *steered* over the CMUT, at a fixed transfer distance and focus distance of 100 mm. With steering is meant that the focal point can be focused in a different direction; pointing the focus point with a different angle as seen from the probe (figure 3.16).

To validate the measurement, a simulation was conducted in which the focal angle was stepped from $-1°$ to $1°$ with steps of $0.1°$. The simulated normalised acoustic intensities at the surface of the CMUT for each of these focal angles can be seen in figure 3.21.

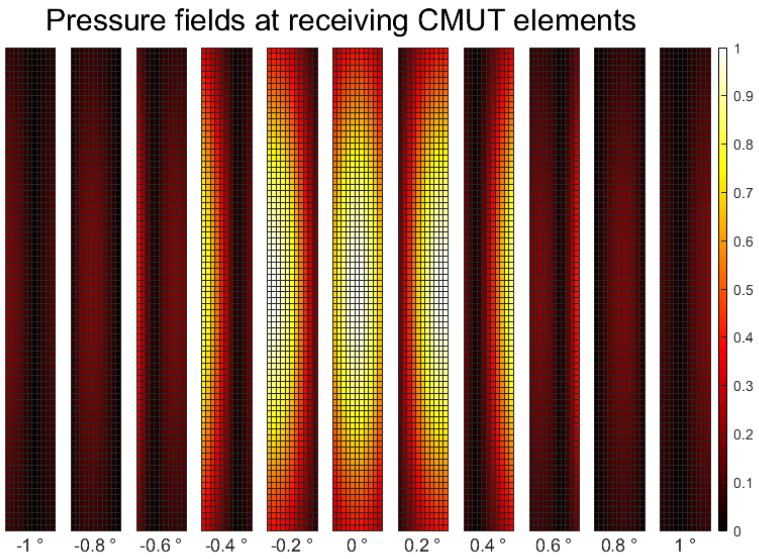

Figure 3.21: The simulated normalised acoustic intensities at the surface of the CMUT for some of the steering angles

In figure 3.22, both the measurement and simulation results for the focus angle are plotted. It was found that the maximum power was harvested at a steering angle of $0°$, indicating the probe and CMUT were perfectly aligned using the established measurement set-up. Furthermore, it can be seen from figure 3.22 that the measurement and simulation results match.

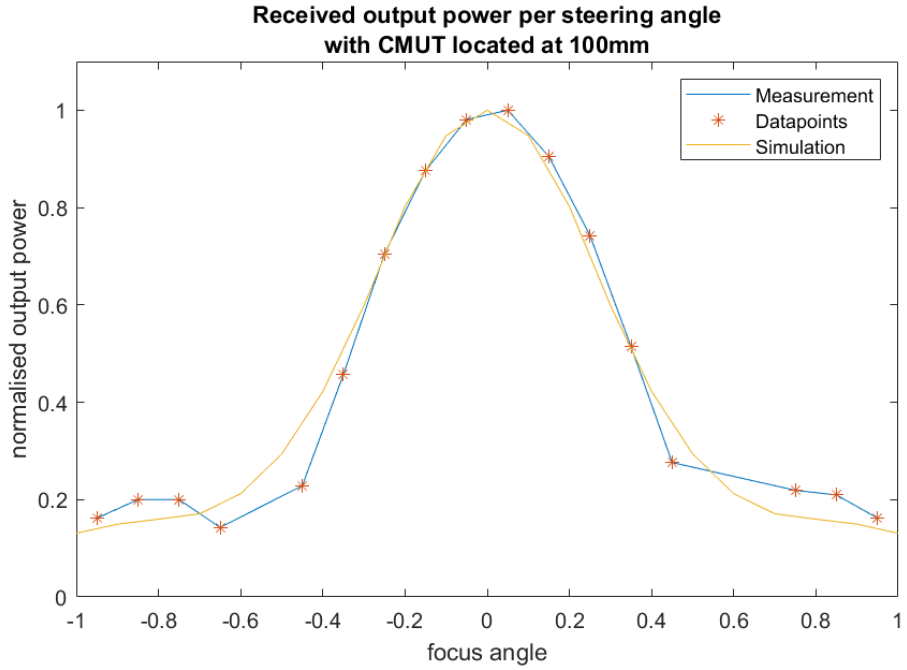

Figure 3.22: Normalised output power as a function of the focus angle with a CMUT located at 100 mm

3.3. Angular Acceptance of the CMUT

To measure the angular acceptance of the CMUT, to determine from which angle the CMUT can still act as an efficient energy harvester, the CMUT was rotated with respect to the probe using the motorised rotational stage (see figure 3.23). For this experiment, a circular phantom was made with the purpose that the transfer distance for every angle was kept equal (figure 3.24).

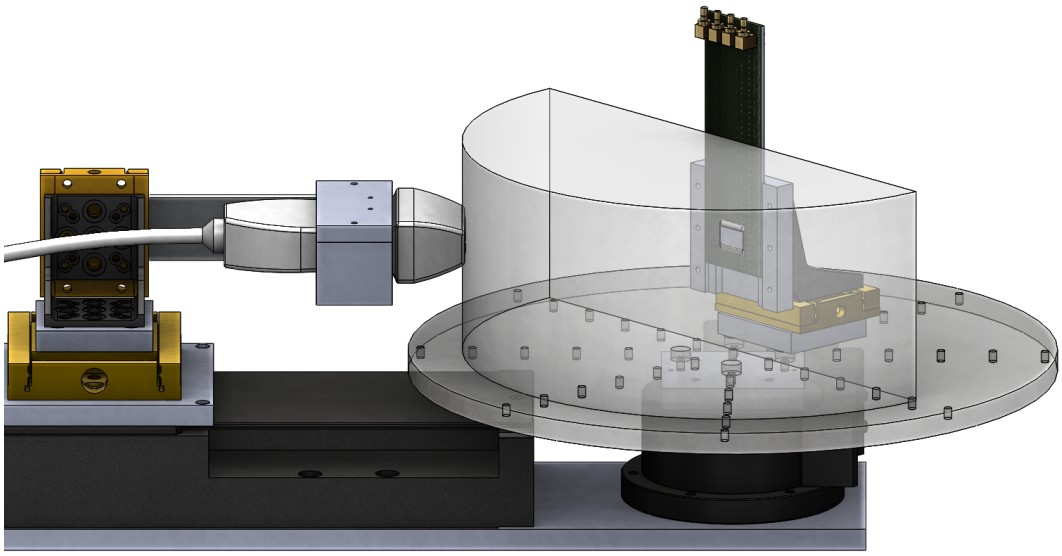

Figure 3.23: Using the rotational stage to change the angle of the CMUT with respect to the probe

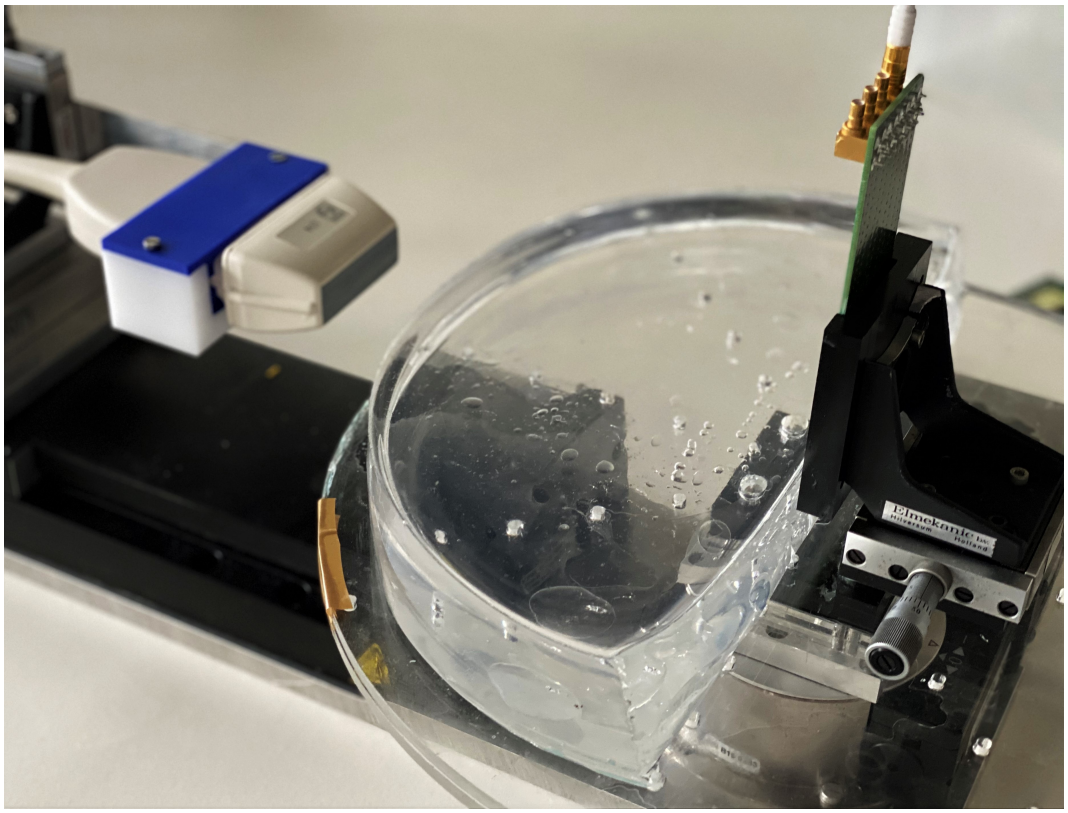

Figure 3.24: The fabricated half circle phantom

The resulting mean normalised output and standard deviation from twenty measurements can be seen in figure 3.25. As expected, the harvested power is maximum when the transmitting probe and receiving CMUT are positioned parallel so that the induced mechanical waves of the probe impinge perpendicularly upon the CMUT its drums.

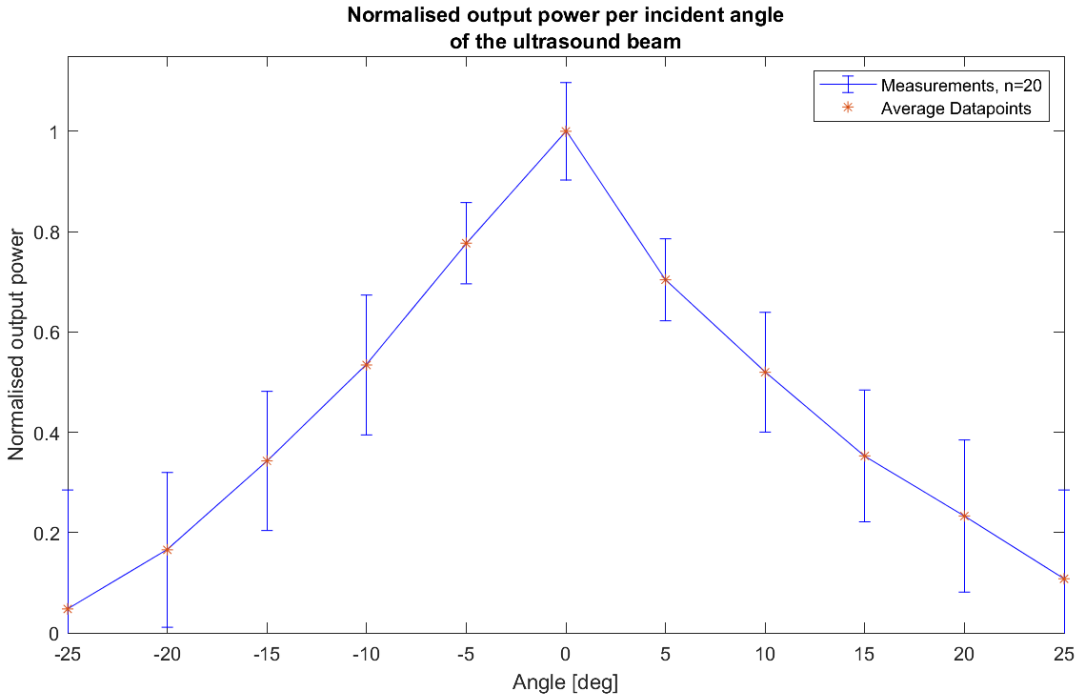

Figure 3.25: Normalised mean output power and standard deviation as a function of the incident ultrasound angle

3.4. Energy Harvesting

3.4.1. The Matching and Rectification Circuit

The realised matching and rectification circuit of (which the schematic can be found in figure 3.27) can be seen in figure 3.26. From left to right, the raw AC Voltage from the CMUT gets matched by a selectable inductance and then rectified by either a full- or half-bridge rectifier. It was found that using full-bridge rectification resulted in the maximum harvested power, and so the full-bridge rectifier was used if AC to DC conversion was needed.

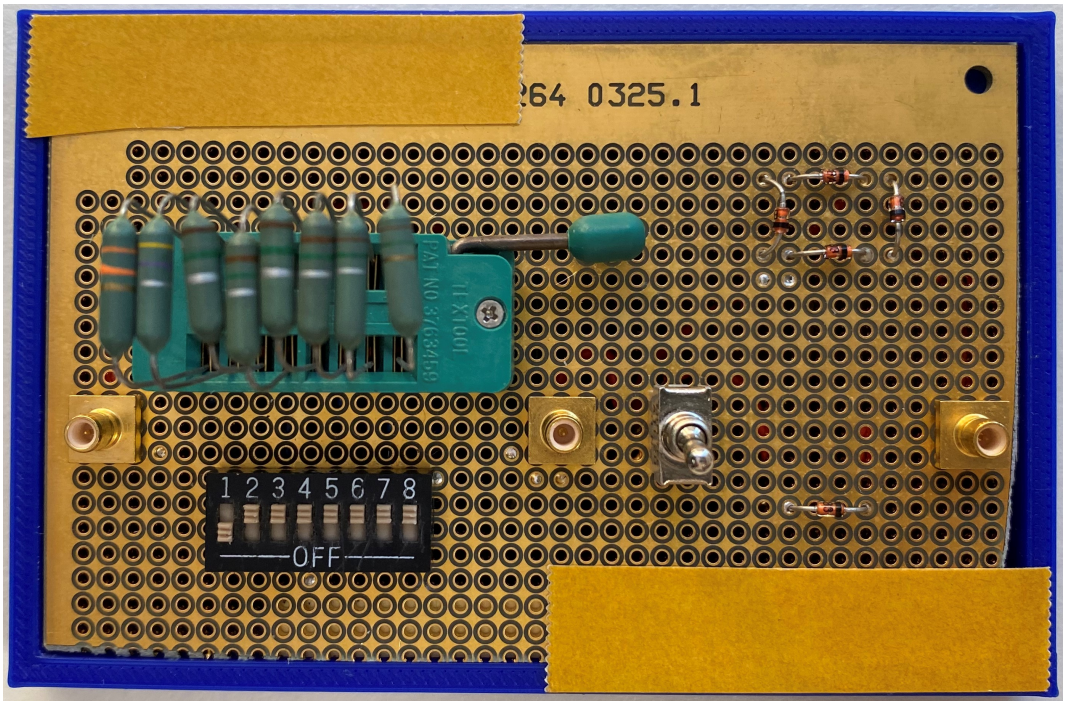

Figure 3.26: The matching and rectification circuit

3.4.2. Matching and Rectification of the Harvested AC Voltage

The CMUT harvests the 24 cycle 4 MHz ultrasound burst and converts it to an AC signal V_0 at its output as shown in figure 3.27. After matching the internal capacitance of the CMUT with an inductance L of approximately 3.3 µH (see figure 2.11), the AC signal amplitude increases to the matched AC signal V_1 as shown in figure 3.27

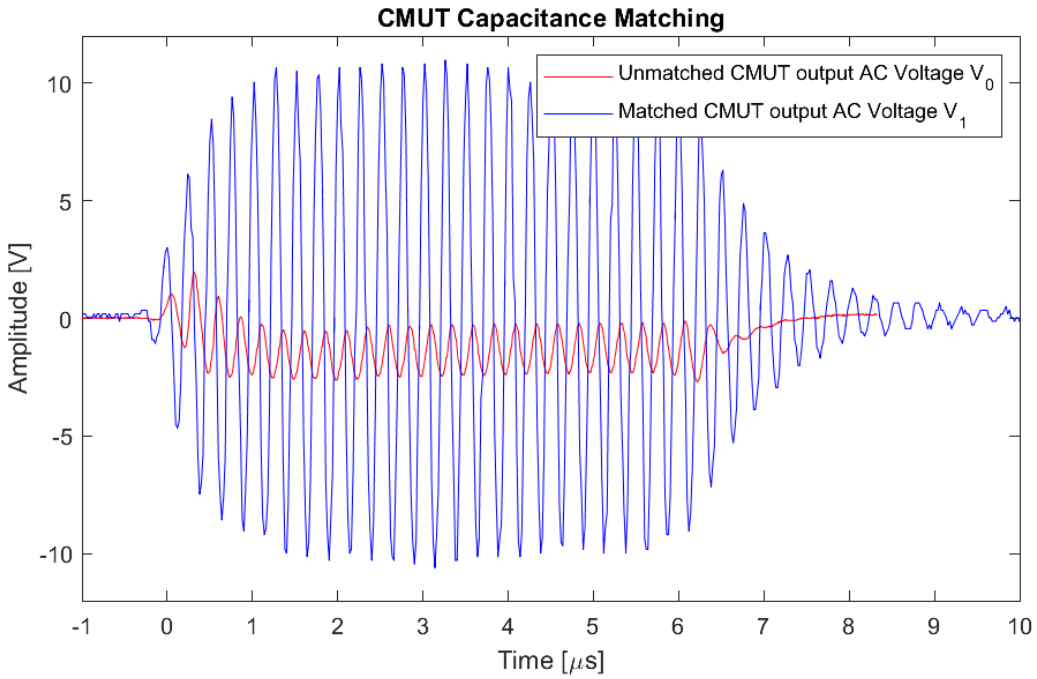

Figure 3.27: Matching of the internal capacitance of the CMUT

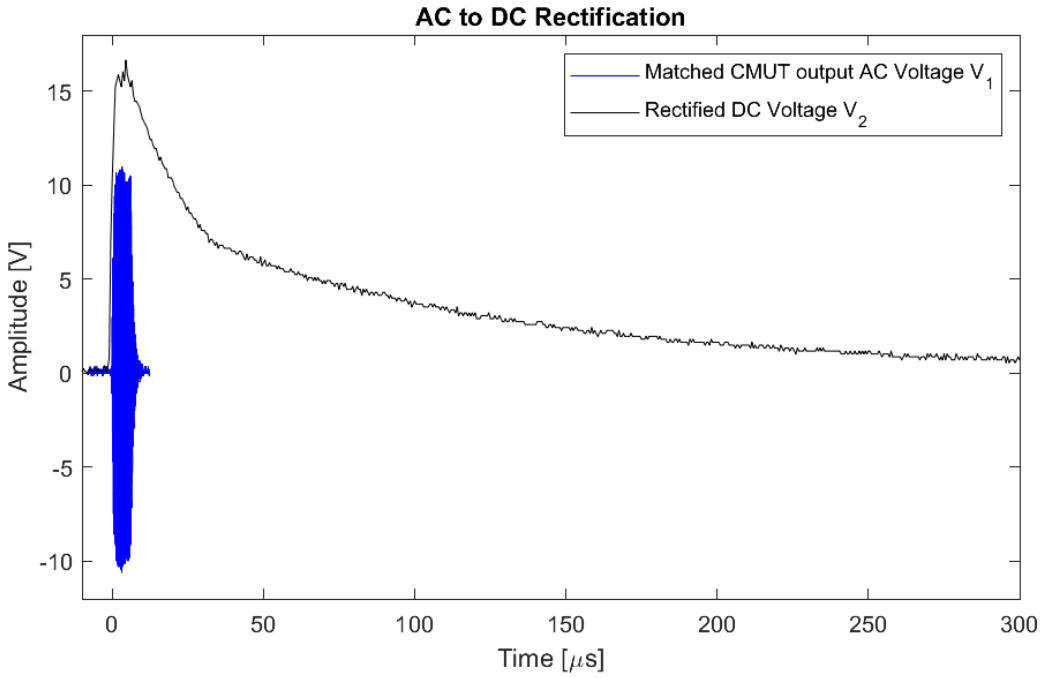

Figure 3.28: AC to DC rectification of the matched CMUT output Voltage

The matched signal V_1 then is rectified using the full-bridge rectification circuit as shown in figure 2.11 to rectified signal V_2, shown in figure 3.28.

During the ultrasound energy transferring experiments, a maximum matched signal with a peak-to-peak voltage of 26.1 V was obtained from the CMUT when focusing the focal focus point of the ultrasound

upon the receiving elements of the CMUT. Whereas the maximum rectified voltage achieved had a peak value of 20.7 V. Both were measured over an unloaded CMUT.

3.4.3. Impedance Matching of the Energy Harvester

To find the load resistance at which the output power is maximised (the matched load), a variable load resistance was connected to the matching and rectification circuit's output. The connected variable load resistance was stepped from 100 Ω to 1000 Ω in steps of 100 Ω. The resulting normalised output power as a function of the load resistance can be seen in figure 3.29.

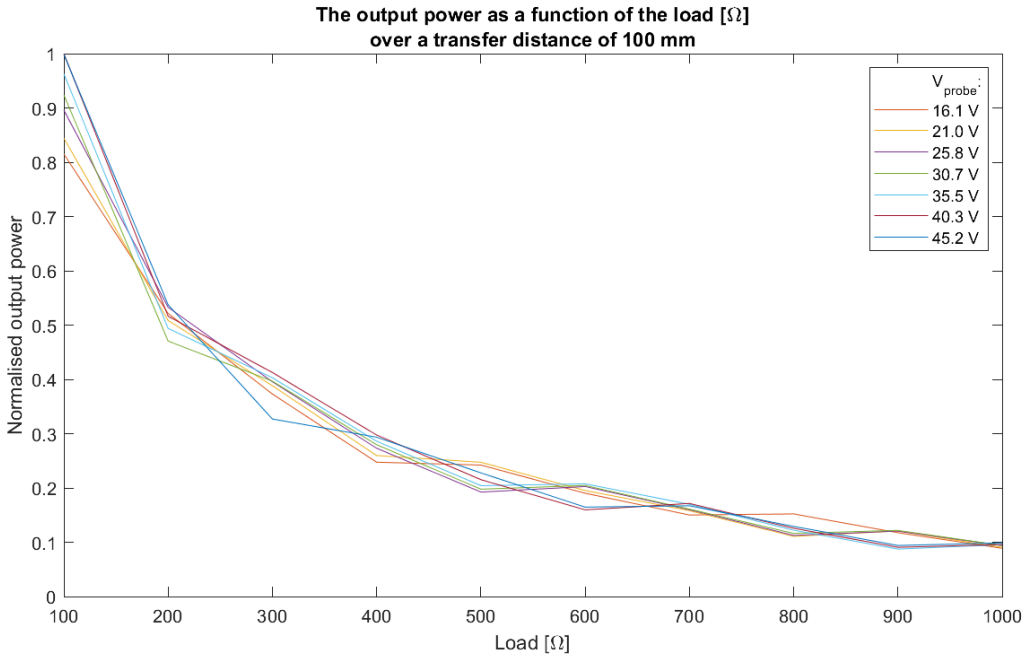

Figure 3.29: Normalised output power as a function of load resistance

The measurement result indicates that the value of the load resistance at which the output power is maximised has a value less than 100 Ω. Since 100 Ω is a rather small load, no further experiments were done to investigate the matched load resistance further.

3.4.4. Harvested Power

The ultrasound energy transfer set-up sends energy in short 24-cycle 4 MHz ultrasound pulse bursts at a maximum repetition frequency of 5 kHz. Therefore the harvesting circuit is not continuously harvesting power. Consequently, the harvested power is first calculated over the harvested pulse as pulse power P_{pulse} and is compensated for the system's duty cycle thereafter.

$$P_{pulse} = \frac{V_{rms}^2}{R_{load}} \tag{3.1}$$

The maximum pulse power harvested over the course of the ultrasound energy transfer experiments was 250 mW. It was harvested with a connected load of 100 Ω at a transferring distance of 75 mm. The AC Voltage output of the loaded CMUT and the corresponding RMS Voltage can be seen in figure

3.30.

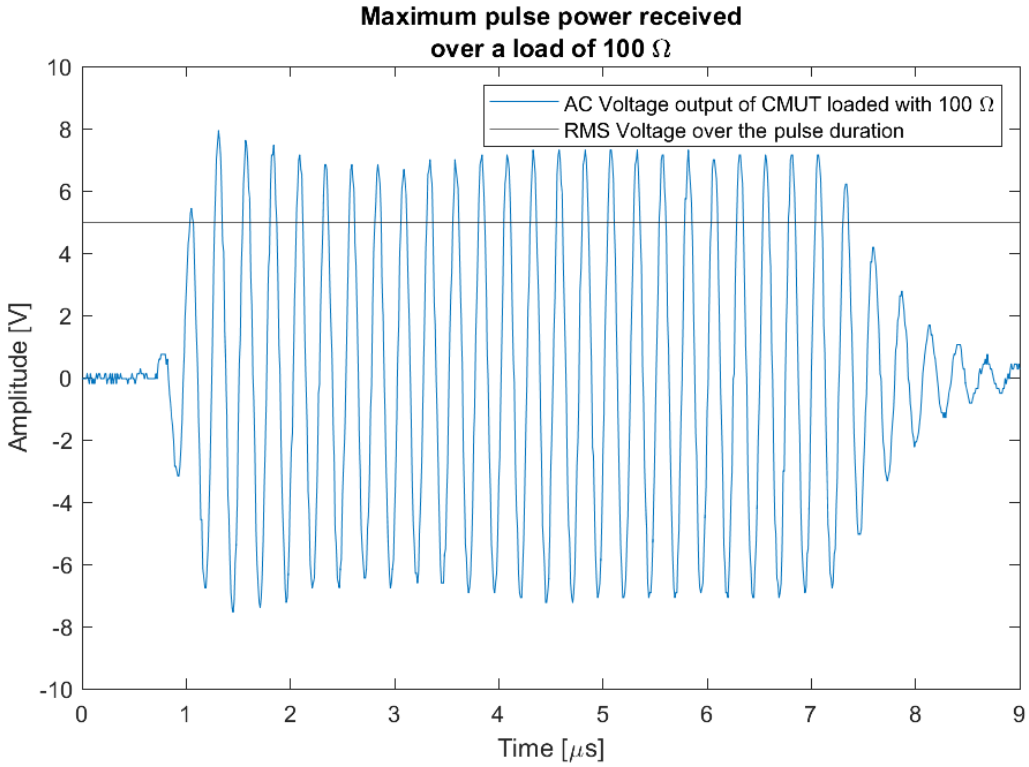

Figure 3.30: The maximum pulse power harvested during the ultrasound energy transfer experiments

The maximum power harvested during the ultrasound energy transfer experiments as a function of the distance can be found in table 3.1. The average power is the pulse power compensated for a maximum duty cycle of 3%. The area of the CMUT used to harvest energy was 1.96 mm^2 (0.28 mm×7 mm), and so in table 3.2 the harvested power per unit area of the CMUT as a function of the distance is given.

Table 3.1: The maximum harvested power as a function of the transfer distance

Maximum harvested power as a function of transfer distance							
Transfer distance	[mm]	25	50	75	100	125	150
Pulse power	[mW]	46	91	250	216	96	23
Average power	[mW]	1.38	2.73	7.5	6.48	2.88	0.69

Table 3.2: The maximum harvested power per unit area as a function of the transfer distance

Maximum harvested power per unit area as a function of the transfer distance							
Transfer distance	[mm]	25	50	75	100	125	150
Pulse power per unit area	[mW cm^{-2}]	2346	4643	12755	11020	4898	1174
Average power per unit area	[mW cm^{-2}]	70.4	139.3	382.7	330.6	146.9	35.2

Assuming that the efficiency at which ultrasound energy is converted into the electrical domain by

the CMUT is above 40% [28], an estimation can be made about the intensity of the focal point of the ultrasound wave targeted at the CMUT. The estimated acoustic intensities used during the power transfer experiments can be found in table 3.3.

Table 3.3: The estimated maximum received acoustic intensity as a function of the transfer distance

Estimated received acoustic intensity as a function of the transfer distance							
Transfer distance	[mm]	25	50	75	100	125	150
I_{sppa}	[mW cm^{-2}]	5865	11608	31888	27550	12245	2935
I_{spta}	[mW cm^{-2}]	176	348.25	956.75	826.5	367.25	88

3.5. Up-link Communication using Ultrasound Back-scattering

The CMUT converts the incoming ultrasound wave into the electrical domain with an efficiency that depends on the matching and loading of the CMUT. Therefore, part of the ultrasound energy as received by the CMUT is not converted and reflected to the energy transmitting probe, which can measure the resulting echo.

It was found that just as for PZTs [35], CMUTs can be matched or loaded differently to change the amplitude of the reflected echo. In figure 3.31 and 3.32 the reflected echos and their envelopes of a loaded and shorted CMUT can be seen, taken from a single channel of the L7-4 probe. Demonstrating that a correctly loaded CMUT converts more ultrasound energy into the electrical domain and therefore reflects less echo.

Using this method, a protocol for up-link communication could be created, in which the load of the CMUT is changed periodically, allowing for modulation of the echo. In this way, an energy harvester located within the body will be able to communicate data such as the state of charge of the internal battery to the outside of the body passively.

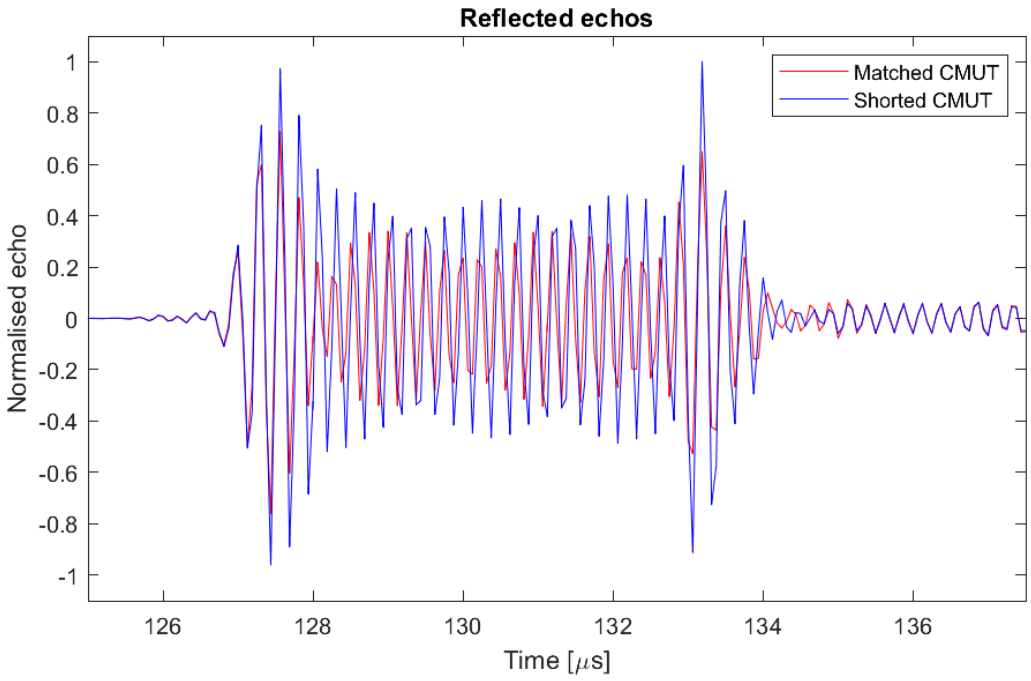

Figure 3.31: The reflected echos of a matched and shorted CMUT

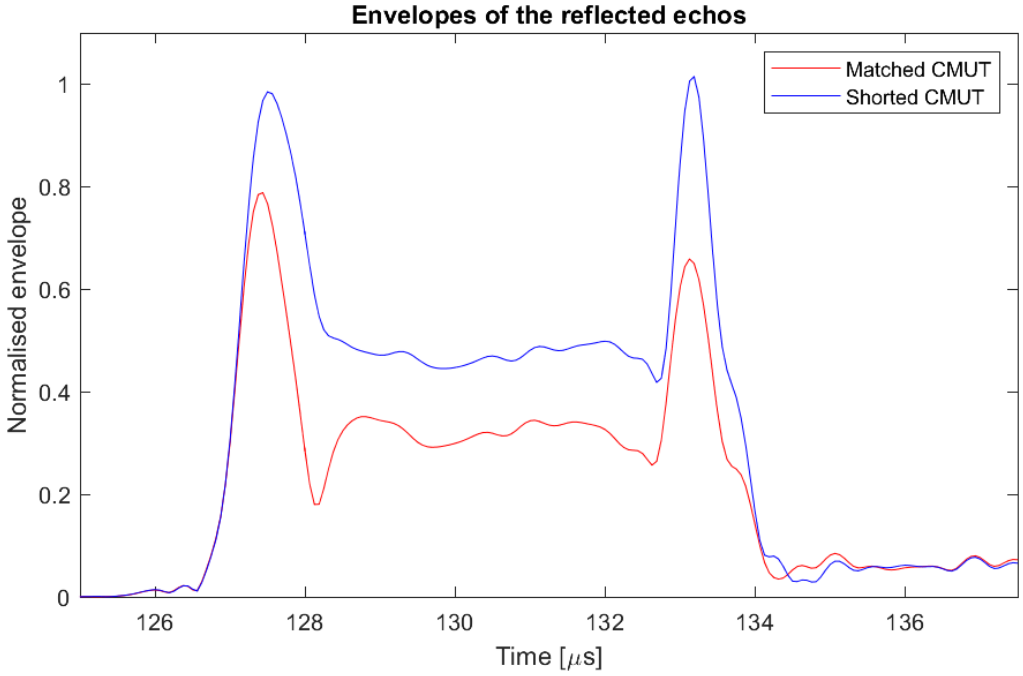

Figure 3.32: The envelopes of the reflected echos of a matched and shorted CMUT

3.6. Direct Electrical Stimulation of a Sciatic Nerve

As a proof of concept, an electrical stimulator was connected to the CMUT to use the harvested energy as a stimulation pulse for an earthworm's sciatic nerve. In figure 3.33 the PCB used for the electrical stimulation can be seen, from left to right, the raw CMUT AC Voltage from the CMUT is matched by an optimal inductance, rectified, and supplied over two stimulation electrodes ($1+$ and $1-$, or $2+$ and $2-$) on which the nerve is placed.

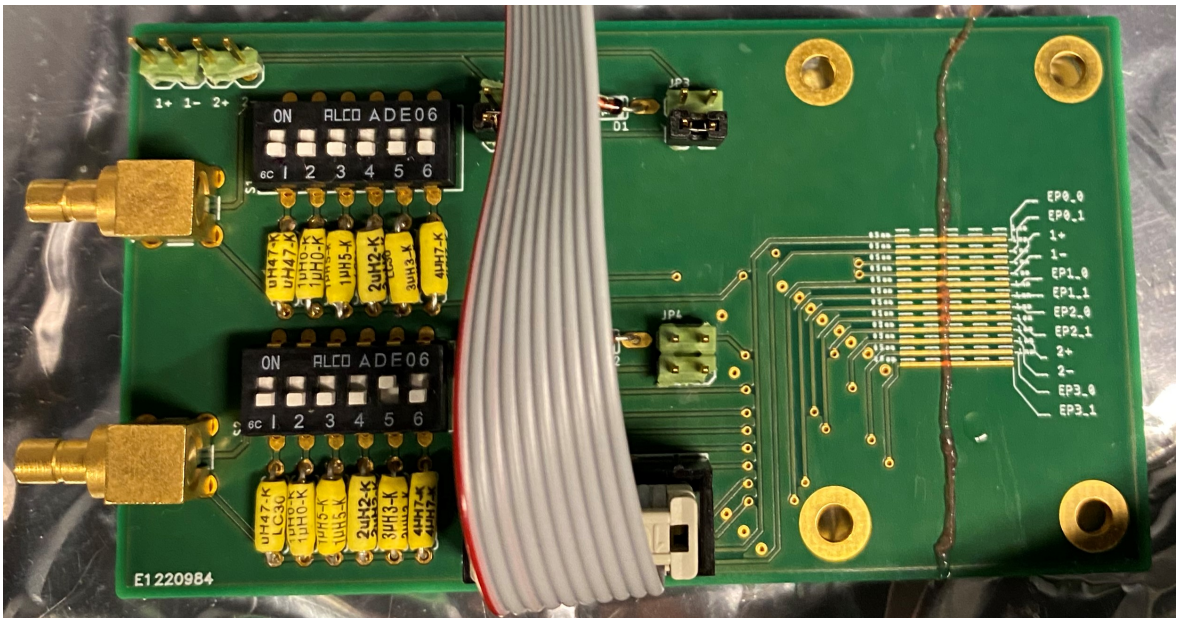

Figure 3.33: The PCB used to supply the harvested DC pulse to the sciatic nerve of an earthworm

The ultrasound energy transfer set-up was programmed to send a 24-cycle 4 MHz ultrasound pulse burst using the probe when triggered by the stimulation recording software. Using the ultrasound energy transfer set-up, enough power was harvested from the received ultrasound pulse burst to supply an electrical stimulation pulse to the nerve sufficient for inducing an action potential. During this successful experiment, the stimulation electrodes $1+$ and $1-$ were used to supply the stimulation pulse, after which the action potential traveled down the nerve over recording electrode pairs $EP1$ and $EP2$, while decreasing in amplitude. In figure 3.34 the action potential recorded over $EP1$ (Electrode Pair 1), the action potential recorded over $EP2$, the trigger signal Ref and the recorded stimulation signal $Estim$ during a successful stimulation can be seen.

During the course of this experiment, found was that a stimulation pulse with an amplitude of approximately 2 V and duration of 6 µs was sufficient. However, the set-up was able to deliver electrical stimulation pulses with amplitudes of up to 9 V to the nerve. An example of such an electrical stimulation pulse harvested from ultrasound energy can be seen in figure 3.35.

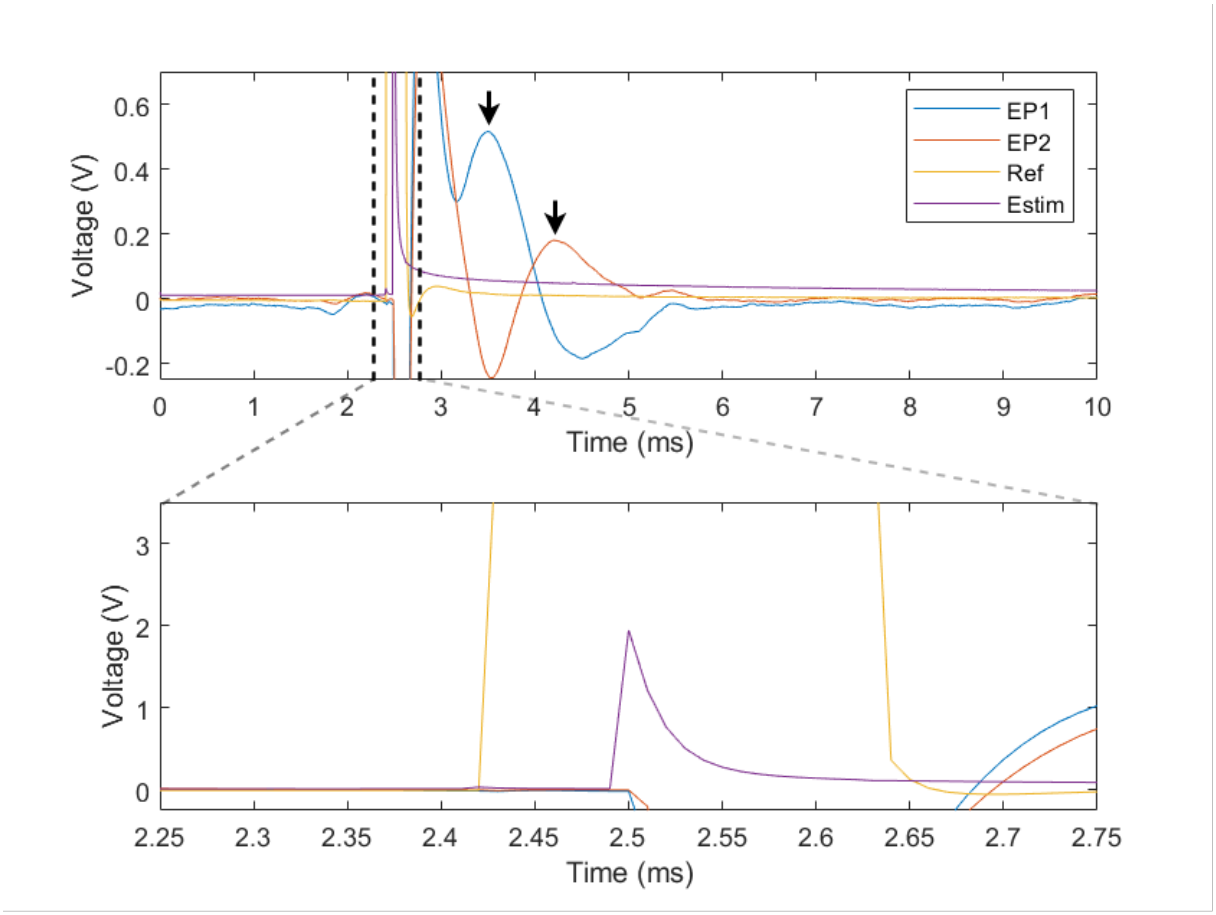

Figure 3.34: The stimulation signal and recorded action potentials [10]

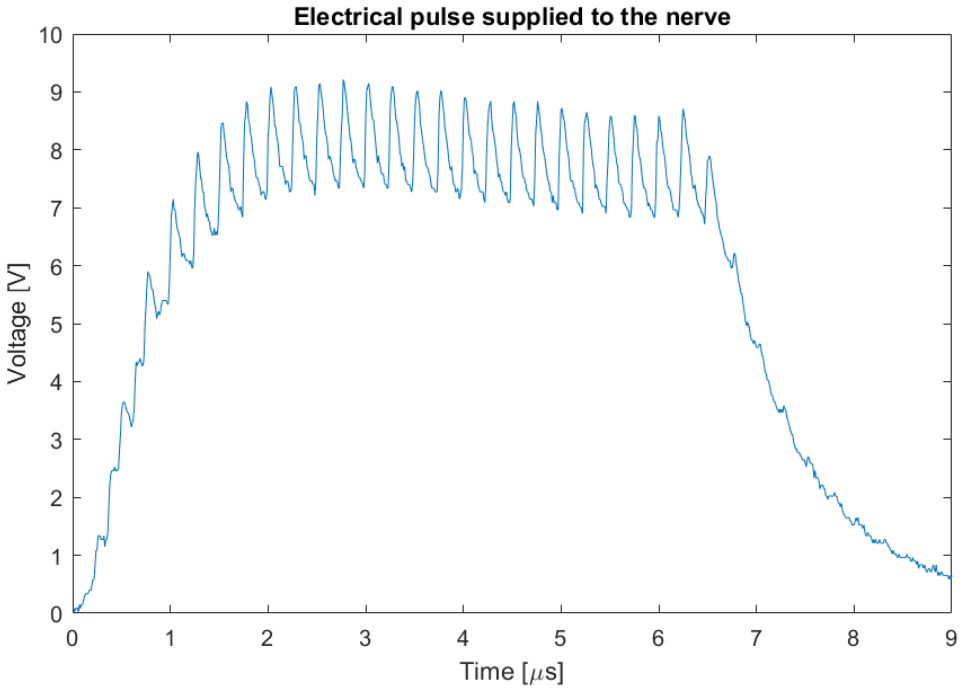

Figure 3.35: The maximum stimulation pulse measured over the sciatic nerve of an earthworm

3.7. Powering of a Medically Certified Bluetooth Module

To demonstrate the device powering capabilities of the created set-up, the RSL10-SOLARSENS-GEVK microchip (manufactured by ON Semiconductor) was connected to the energy harvester. The RSL10 has an on-board Bluetooth module designed for medical applications and was programmed to transmit the battery voltage, temperature, humidity, and air pressure to the RSL10 Sensor Beacon smartphone application.

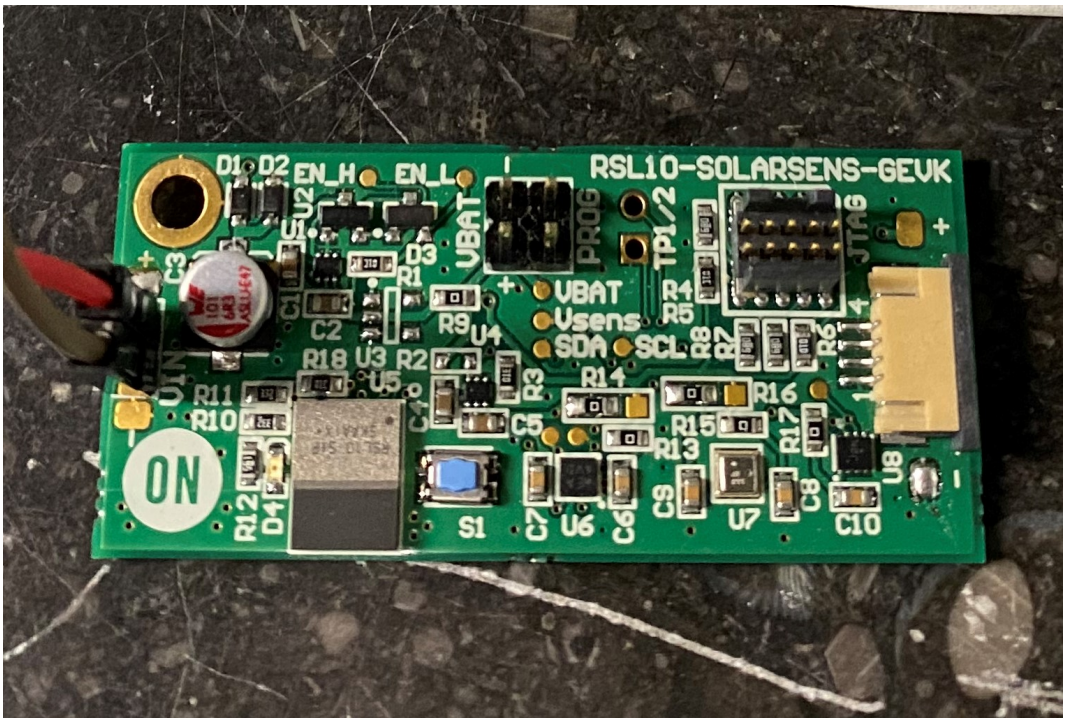

Figure 3.36: The RSL10-SOLARSENS-GEVK by ON Semiconductor

The RSL10 has a DC supply Voltage range of 1.1 V - 3.3 V. Therefore the full-bridge rectifier on the matching and rectification circuit was used to supply a DC pulse (figure 3.28) to charge the 6.8 µF capacitor (the battery) on the RSL10.

The rectified DC pulse was sufficient to charge the capacitor of the RSL10 and make it transmit information via Bluetooth. In figure 3.37 the battery Voltage can be seen during operation. The measured Voltage over the battery decreases every time the RSL10 goes through a transmitting sequence and is recharged thereafter by the ultrasound energy transferring set-up. Screenshots of the transmitted information received by the RSL10 Sensor Beacon application on a smartphone can be found in figure 3.38.

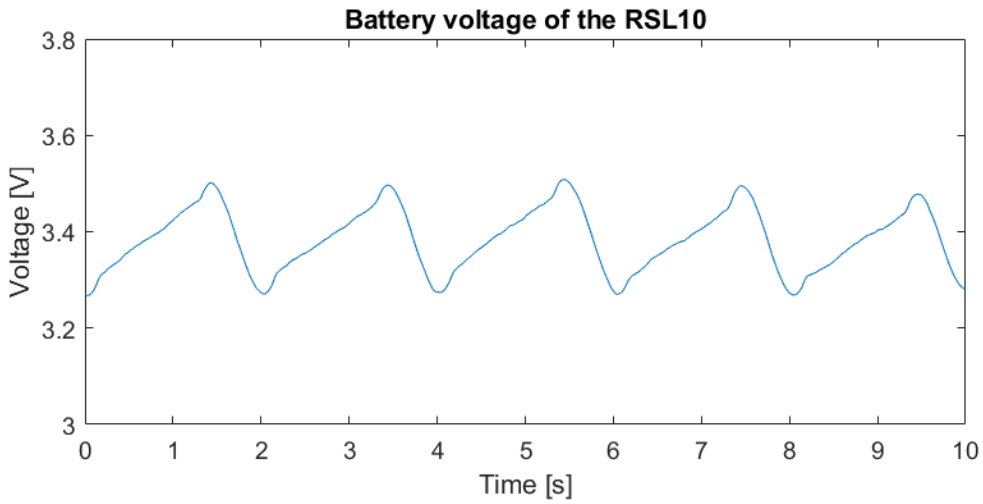

Figure 3.37: The battery Voltage of the RSL10-SOLARSENS-GEVK while powered by ultrasound

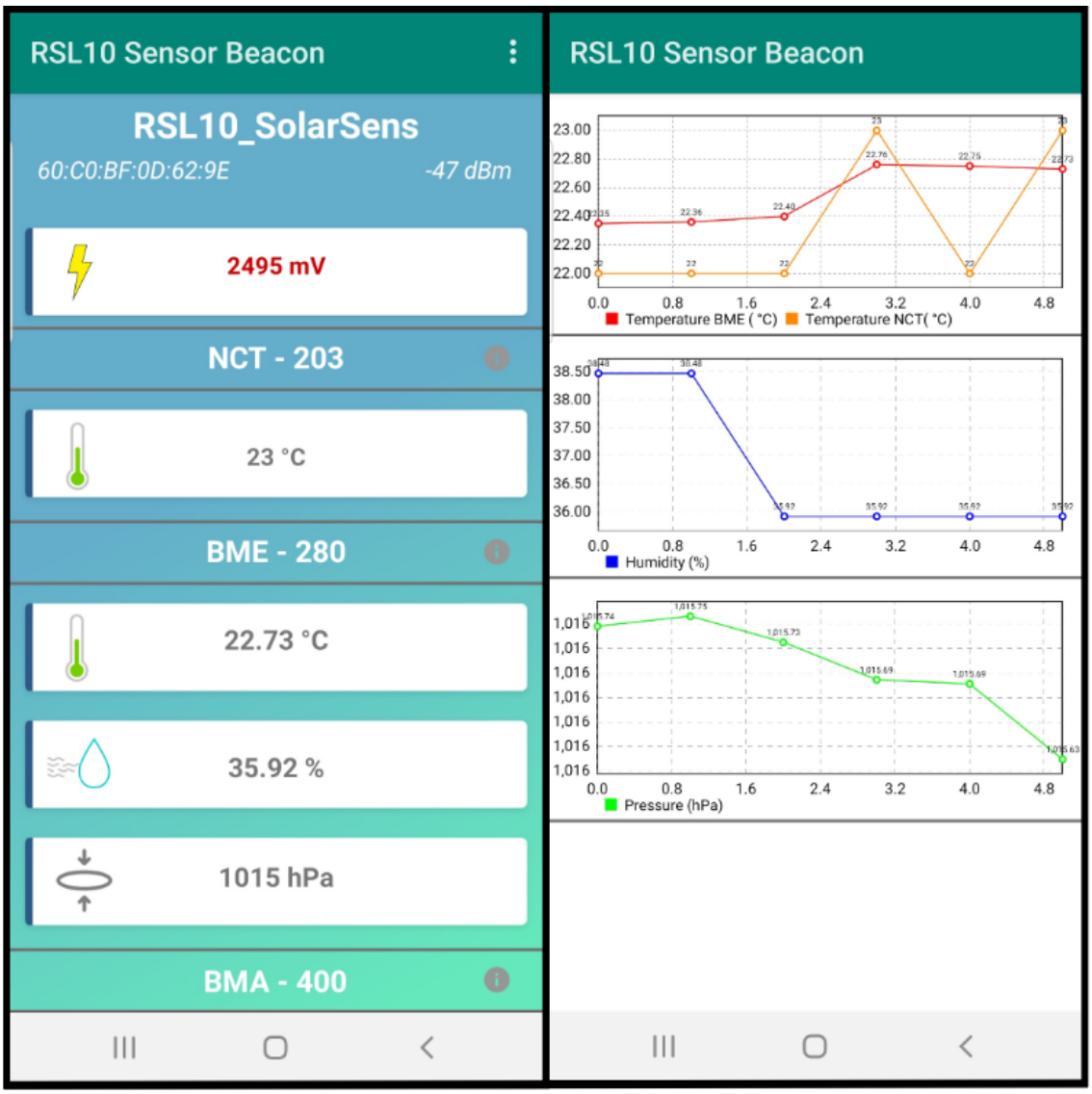

Figure 3.38: The transmitted information received by the RSL10 Sensor Beacon app

3.8. Ultrasound Energy Transfer through Pork Tissue

Lastly, an experiment was done in which the ultrasound energy transfer set-up was used to transfer energy through biological tissue. The biological tissue used during this experiment was a piece of pork leg, which can be seen in figures 3.39 and 3.40. The transfer distance during this experiment was set at 90 mm.

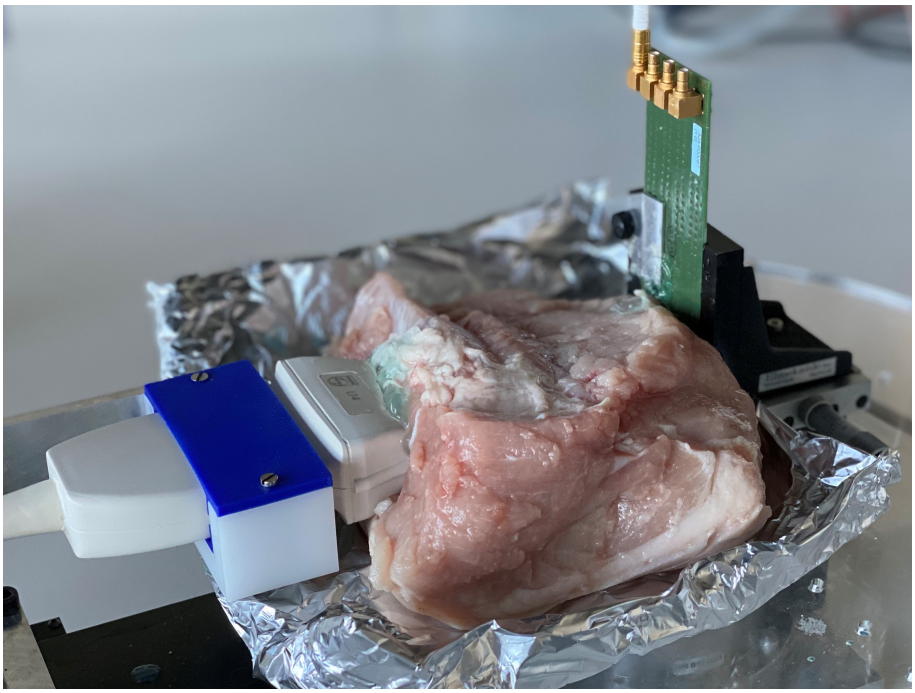

Figure 3.39: The pork tissue used in the ultrasound energy transfer set-up

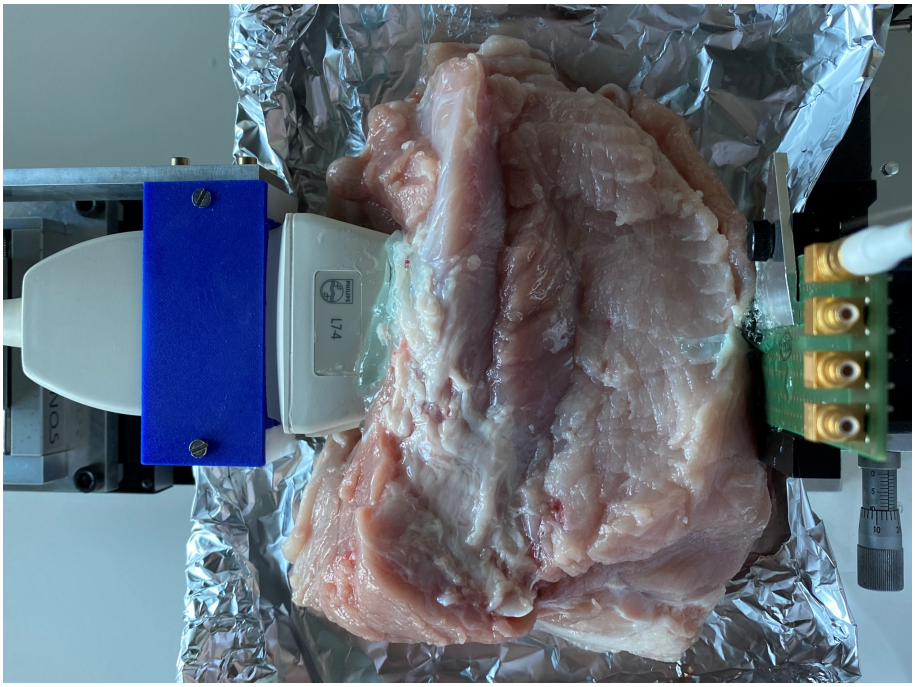

Figure 3.40: Top view of the pork tissue experiment

First, a look was taken at the unloaded output of the matching circuit, in which an inductance of 3.3 µH was used to match for the internal capacitance of the CMUT. The unloaded peak-to-peak Voltage output of the matched CMUT as a function of the probe Voltage V_{probe} can be found in figure 3.41.

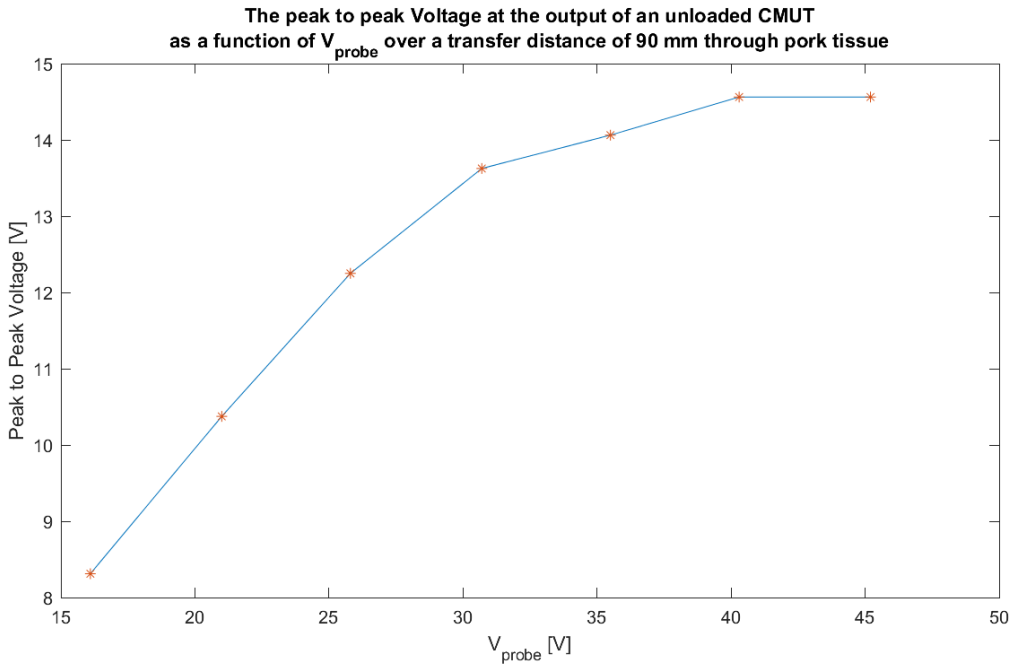

Figure 3.41: The peak-to-peak Voltage as a function of the probe Voltage V_{probe} for a transfer distance of 90 mm through pork tissue

Hereafter, the harvesting circuit was loaded to determine the transferred power. In figure 3.42, the harvested power as a function of the load resistance can be found.

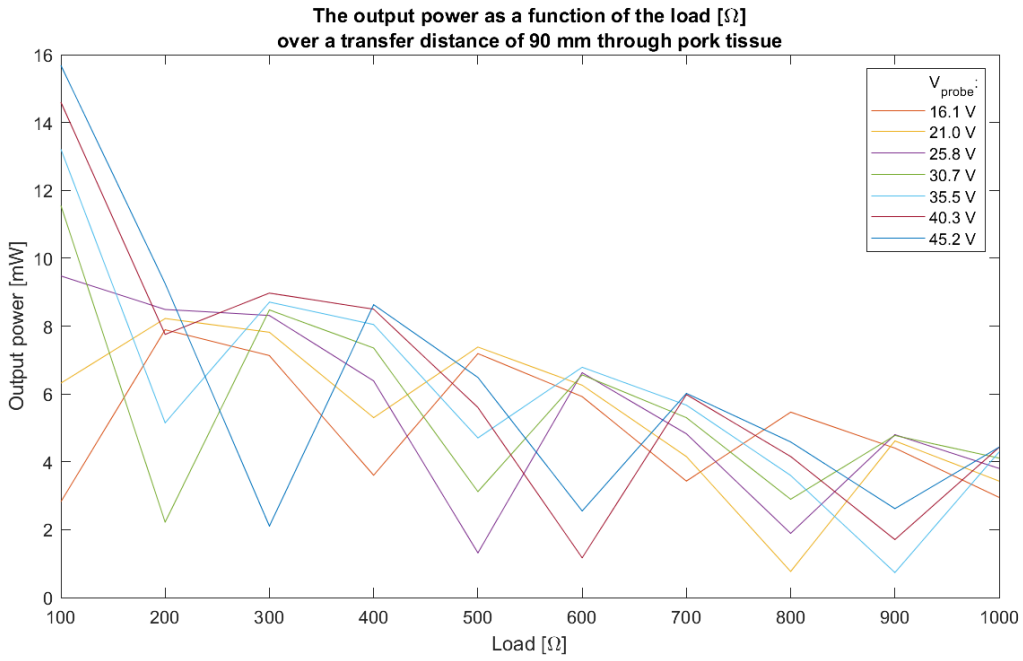

Figure 3.42: The output power as a function of the load resistance for a transfer distance of 90 mm through pork tissue

The output power as a function of the connected load shows to be non-linear, which was unexpected after the results of the same measurement using the paraffin gel phantom in Section 3.4.3, and therefore is possibly a consequence of using the pork tissue.

Using the pork meat, up-link communication as described in section 3.5 using ultrasound back-scattering of the CMUT was again proven successful, and the amount of harvested power was sufficient to directly power the RSL10 Bluetooth module as described in Section 3.7. The maximum harvested power as a function of the probe voltage can be found in table 3.4.

Table 3.4: The maximum harvested power as a function of the probe voltage

Maximum harvested power over a load as a function of the probe voltage for a transfer distance of 90 mm								
Probe Voltage V_{probe}	[V]	16.1	21.0	25.8	30.7	35.5	40.3	45.2
Maximum harvested power	[mW]	7.9	8.2	9.5	11.6	13.2	14.6	15.7
Load	[Ω]	200	200	100	100	100	100	100

4

Discussion

With its lower attenuation in the body and smaller wavelengths as compared to its electromagnetic counterpart, ultrasound energy transfer seems to be an efficient and safe method to transfer energy over long distances to small implantable medical devices.

The total ultrasound energy transfer system developed in this thesis work consisted of the Verasonics Vantage and Philips L7-4 Linear array transducer as the energy transmitter, a mechanical set-up to align the probe with respect to the CMUTs, and the harvesting circuit which included the charged CMUTs. The complete system showed to be able to transfer a maximum power of 250 mW over a transferring distance of 75 mm.

First, three types of CMUTs were methodologically charged to find the charging voltage and charging duration at which the phase peak of the resonance frequency was maximum. After this, an estimation was made of the amount of trapped charge in the Al_2O_3 layers. Variant $P67$ showed to be the most reliable CMUT, with no signs of dielectric breakdown as a result of the charging process, and was therefore chosen to be used as the energy harvester in the ultrasound energy transfer set-up. Further investigation is necessary to determine under which circumstances the trapped charge is retained in the Al_2O_3 layer and what the retention time of charged CMUTs is.

Using the Verasonics Vantage, ultrasound pulse bursts were transmitted and focused on the CMUTs, and the focusing showed to be very effective. However, since ultrasound is mainly used for imaging purposes, the amount of energy transmitted by the Verasonics Vantage and Philips L7-4 Linear array transducer was limited to short pulse burst, resulting in a low maximum duty-cycle of 3%. Furthermore, it was not possible to do system efficiency measurements since the Verasonics Vantage did not allow for monitoring of the power delivered to the Philips L7-4 probe. Nonetheless, a considerable amount of power was harvested by the CMUTs after matching of its internal capacitance with an inductance and loading it with a load resistor.

The power harvested was extremely dependent on the alignment of the probe with respect to the CMUTs, and the interfaces between the probe, medium, and CMUT. Meaning that a small misalignment of the experimental set-up did result in a significant efficiency drop of the system. Focusing on a millimetre sized implant located deeply in a body will therefore be immensely difficult. Accurate alignment will require an up-link communication channel and a closed loop control system to accurately determine if the focal point is targeted at the right location.

Luckily, it was found that the charged CMUTs can be used as a means of up-link communication. The

resulting echo reflected by the charged CMUTs depends on the matching and load of the CMUTs, where an optimal load results in the smallest returned echo. Using this technique, information can be sent back to the energy transmitting system using load modulation. Meaning a feedback loop could possibly be created in which the focusing is done automatically.

The transferred power showed to be sufficient for direct electrical stimulation of the sciatic nerve of an earthworm, in which action potentials were induced by the harvested pulse from the received ultrasound energy. This shows that ultrasound energy can be used to directly stimulate nerves.

Finally, an experiment was conducted in which pork tissue was used as the medium. It was shown that abundant energy could be sent through the pork tissue to establish successful up-link communication, and that adequate power was transferred through the pork tissue to power a medically certified Bluetooth module on a microchip over a transfer distance of 90 mm.

Overall, it can be stated that ultrasound energy transfer is an exciting technique to wirelessly transfer energy for all kinds of biomedical applications.

5

Conclusion

Charged capacitive micromachined ultrasound transducers (CMUTs) can harvest significant amounts of power from ultrasound transmitted from a medical imaging probe. Using focusing of the ultrasound, proper alignment of the system, and matching of the CMUTs, a maximum power of 250 mW was harvested. It is demonstrated shown that CMUTs can be used to passively communicate back information to the energy transmitting ultrasound probe using ultrasound back-scattering. And finally, it was shown that the charged CMUTs can harvest sufficient energy to stimulate a nerve and to power a medically certified Bluetooth module directly.

A

Impedance and Phase Plots Obtained During the Charging Process

In this appendix, the impedance and phase plots obtained during the charging process of the $P67$, $P69$, and $P103$ an be found.

A.1. P67

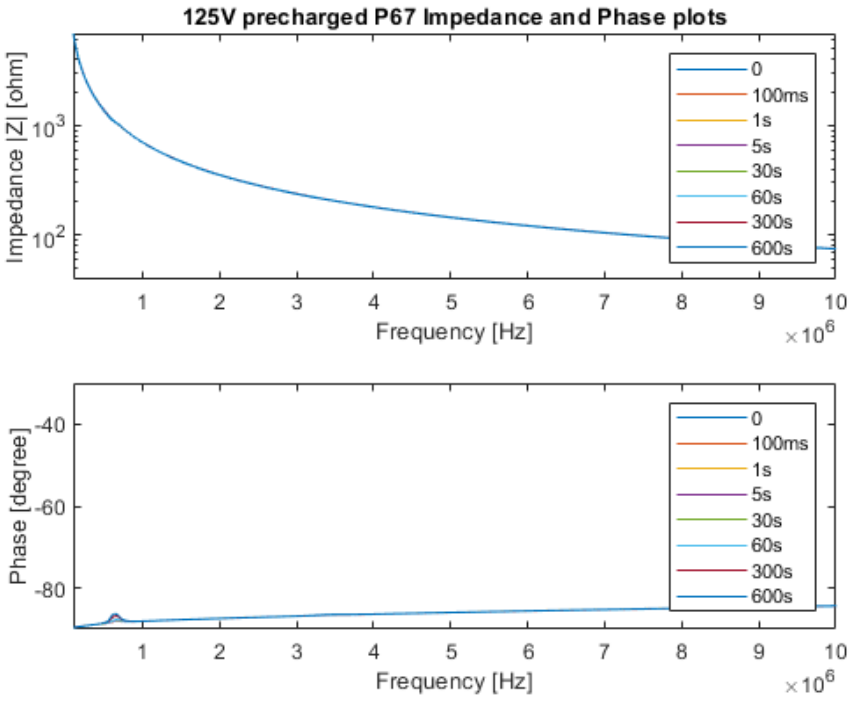

Figure A.1: The impedance and phase spectra of the $P67$ for a charging-Voltage of 125 V as a function of the charging-duration

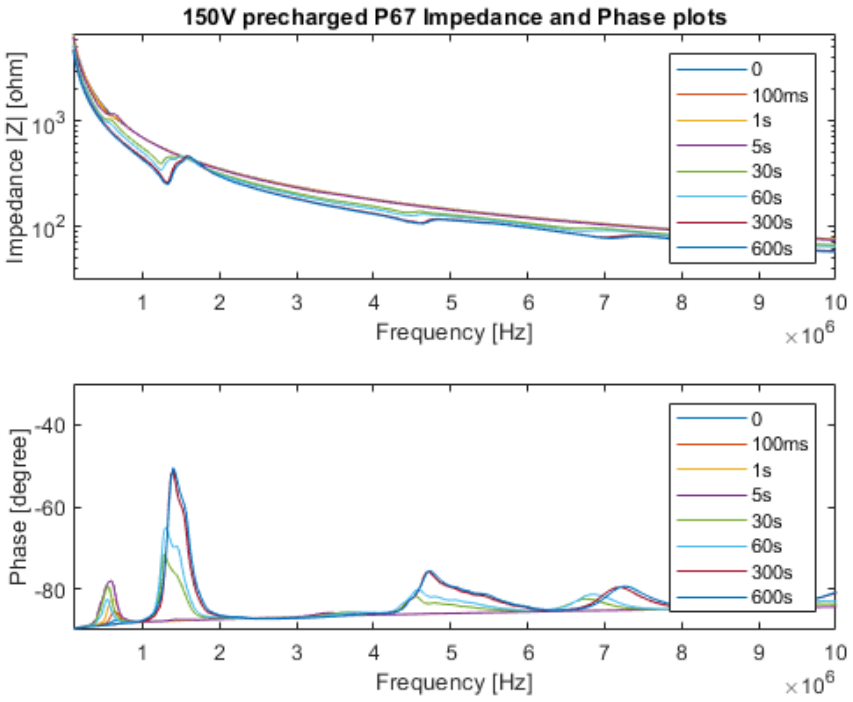

Figure A.2: The impedance and phase spectra of the $P67$ for a charging-Voltage of 150 V as a function of the charging-duration

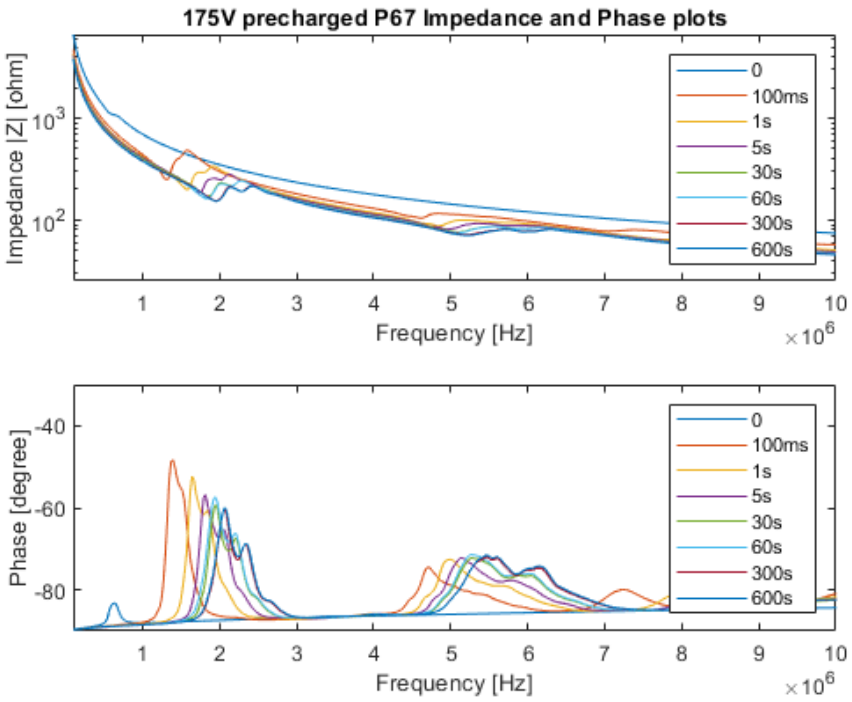

Figure A.3: The impedance and phase spectra of the $P67$ for a charging-Voltage of 175 V as a function of the charging-duration

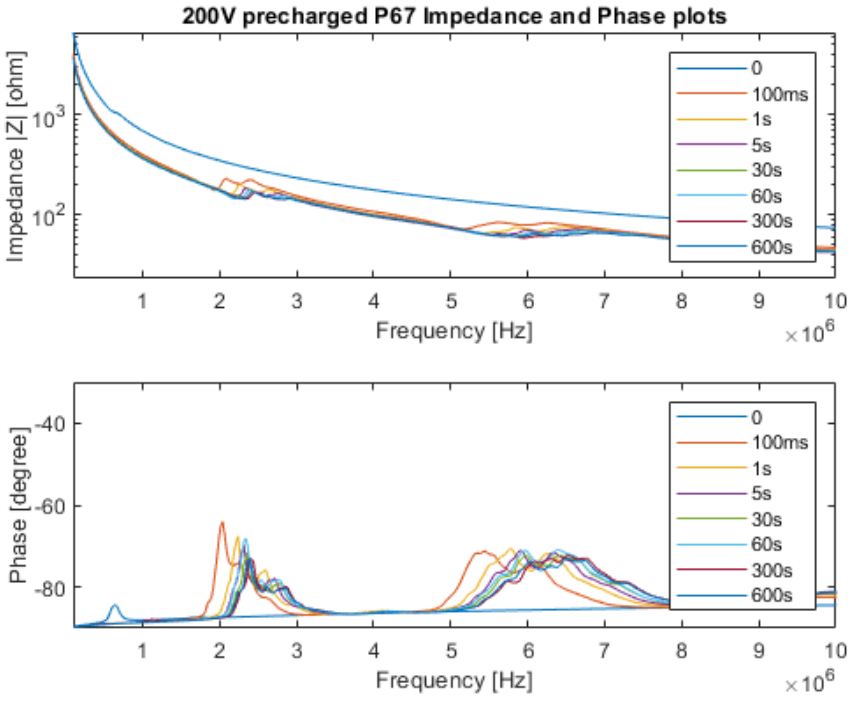

Figure A.4: The impedance and phase spectra of the $P67$ for a charging-Voltage of 200 V as a function of the charging-duration

A.2. P69

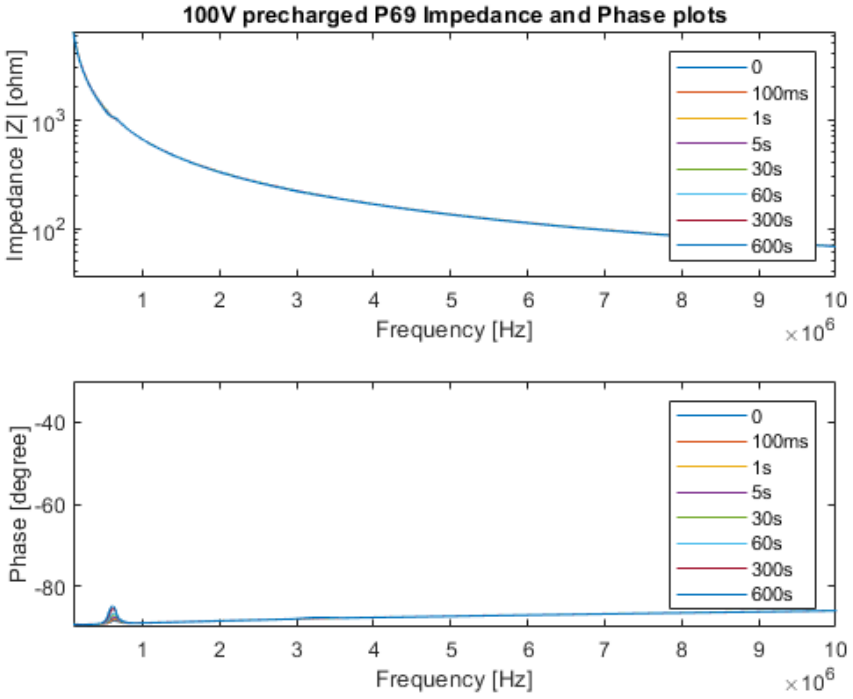

Figure A.5: The impedance and phase spectra of the $P69$ for a charging-Voltage of 125 V as a function of the charging-duration

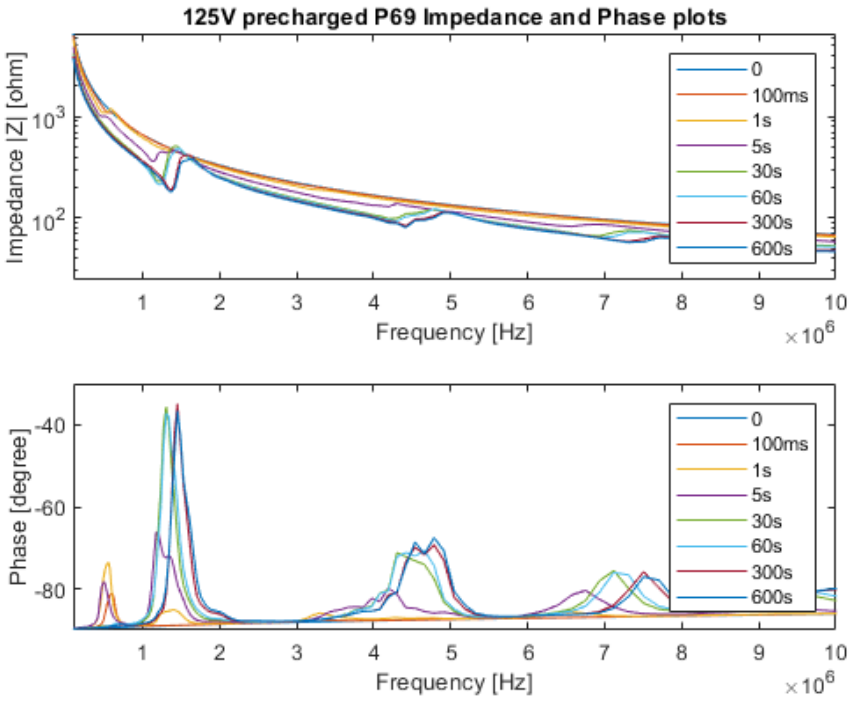

Figure A.6: The impedance and phase spectra of the $P69$ for a charging-Voltage of 125 V as a function of the charging-duration

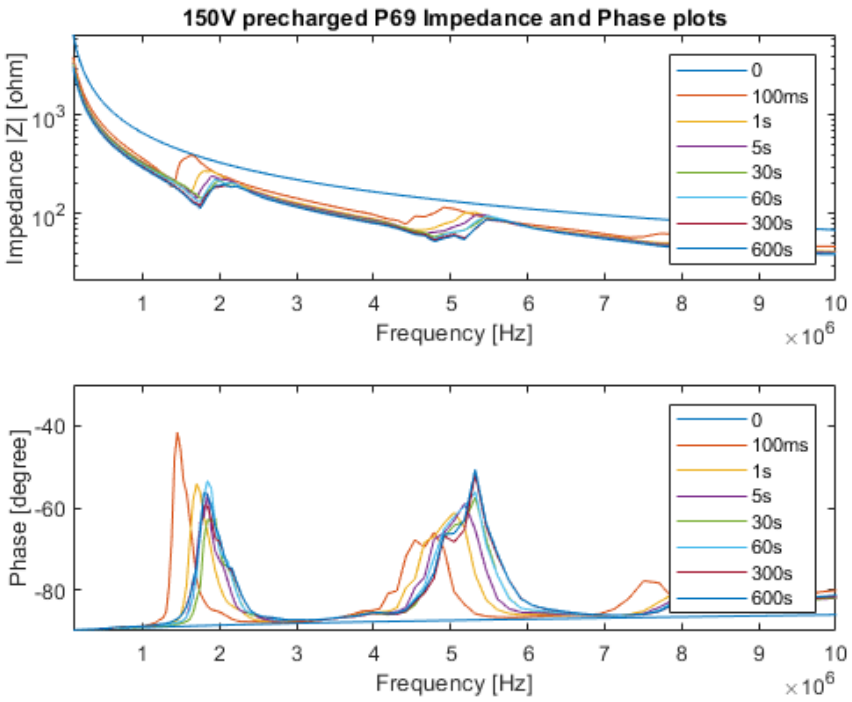

Figure A.7: The impedance and phase spectra of the $P69$ for a charging-Voltage of 150 V as a function of the charging-duration

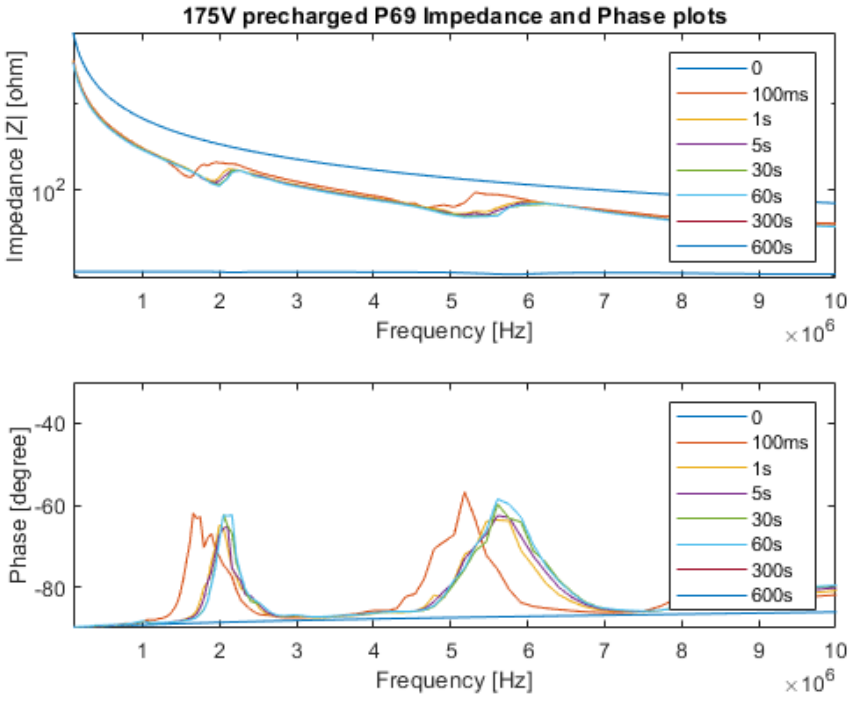

Figure A.8: The impedance and phase spectra of the $P69$ for a charging-Voltage of 175 V as a function of the charging-duration

A.3. P103

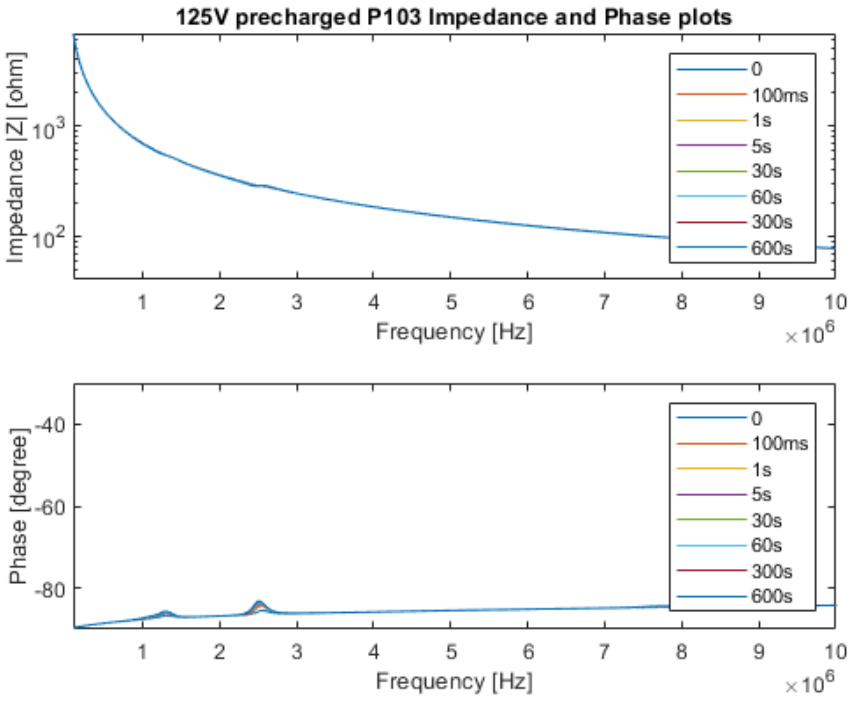

Figure A.9: The impedance and phase spectra of the $P103$ for a charging-Voltage of 125 V as a function of the charging-duration

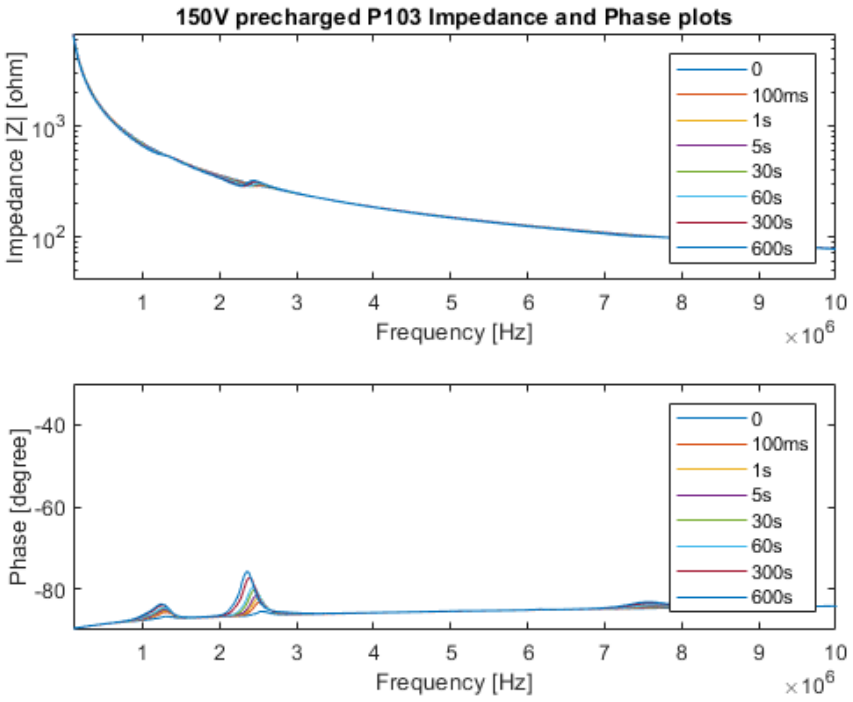

Figure A.10: The impedance and phase spectra of the $P103$ for a charging-Voltage of 150 V as a function of the charging-duration

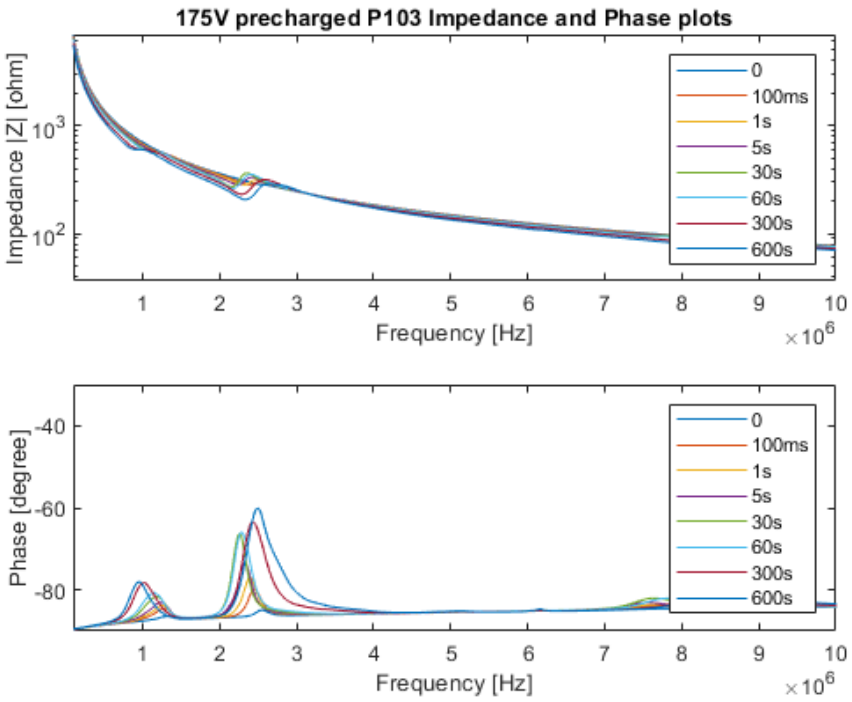

Figure A.11: The impedance and phase spectra of the $P103$ for a charging-Voltage of 175 V as a function of the charging-duration

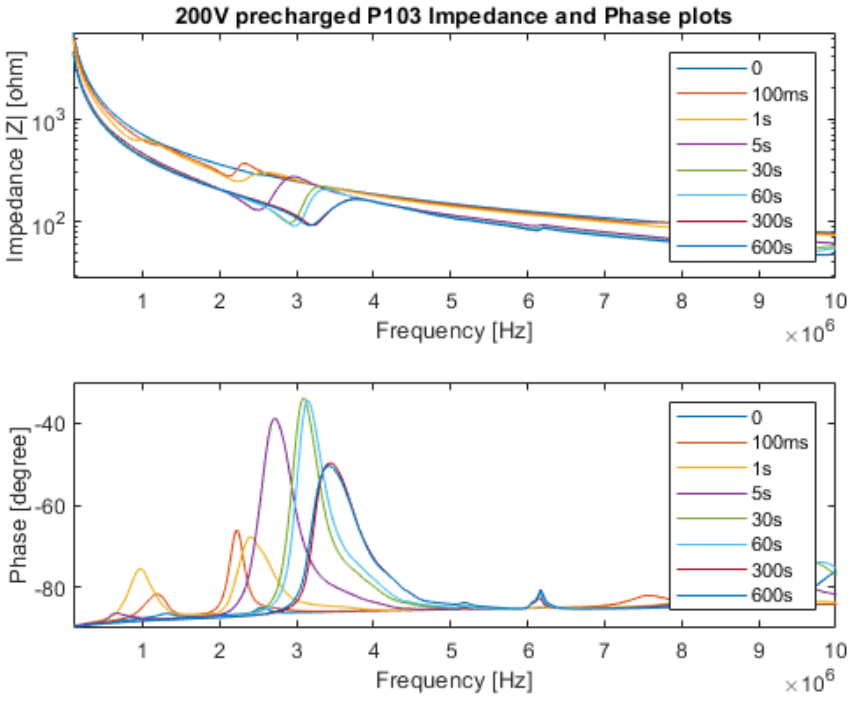

Figure A.12: The impedance and phase spectra of the $P103$ for a charging-Voltage of 200 V as a function of the charging-duration

Bibliography

[1] Achraf Ben Amar, Ammar B. Kouki, and Hung Cao. Power approaches for implantable medical devices. *SENSORS*, 15:28889–28914, 2015. doi: 10.3390/s151128889.

[2] Hongchae Baek, Ki Joo Pahk, and Hyungmin Kim. A review of low-intensity focused ultrasound for neuromodulation. *Biomed. Eng Lett.*, 7:135–142, 2017. doi: 10.1007/s13534-016-0007-y.

[3] Stanley B. Barnett, Gail R. Ter Haar, Marvin C. Ziskin, Hans-Dieter Rott, Francis A. Duck, and Kazuo Maeda. International recommendations and guidelines for the safe use of diagnostic ultrasound in medicine. *Ultrasound in Medicine and Biology*, 26:355–366, 2000.

[4] Hamid Basaeri, David B. Christensen, and Shad Roundy. A review of acoustic power transfer for bio-medical implants. *Smart Materials and Sctructures*, 25, 2016. doi: 10.1088/0964-1726/25/12/123001.

[5] Baris Bayram, Edward Haeggstrom, Goksen G. Yaralioglu, and Butrus T. Khuri-Yakub. A new regime for operating capacitive micromachined ultrasonic transducers. *IEEE transactions on ultrasonics, ferroelectrics, and frequency control*, 50(9), 2003.

[6] Tommaso Campi, Silvano Cruciani, Federica Palandrani, Valerio De Santis, Akimasa Hirata, and Mauro Feliziani. Wireless power transfer charging system for aimds and pacemakers. *IEEE TRANSACTIONS ON MICROWAVE THEORY AND TECHNIQUES*, 64, 2016.

[7] G. V. B. Cochran, M. W. Johnson, M. P. Kadaba, F. Vosburgh, M. W. Ferguson-Pell, and V. R. Palmeiri. Piezoelectric internal fixation devices: A new approach to electrical augmentation of osteogenesis. *J. Orthopaedic Res.*, 3(4):508–513, 1985.

[8] Martin O. Culjat, David Goldenberg, Priyamvada Tewari, and Rahul S. Singh. A review of tissue substitutes for ultrasound imaging. *Ultrasound in Med. Biol.*, 36, 2010. doi: doi:10.1016/j.ultrasmedbio.2010.02.012.

[9] Diane Dalecki. Mechanical bioeffects of ultrasound. *Annual Review of Biomedical Engineering*, 6 (1):229–248, 2004. doi: 10.1146/annurev.bioeng.6.040803.140126.

[10] Eric Dijkema. Towards cmut for neurostimulation. 2020.

[11] A. Hakansson, J. Sanchez-Dehesa, and L. Sanchis. Aoustic lens design by genetic algorithms. *Physical Review*, 70, 2004. doi: 10.1103/PhysRevB.70.214302.

[12] https://www.massdevice.com/silicone-materials-for-long-term-medical-implants-innovate-for-the future/. Silicone materials for long-term medical implants: Innovate for the future. 2019.

[13] Takeshi Inoue, Masaya Ohta, and Sadayuki Takahashi. Design of ultrasonic transducers with multiple acoustic matching layers for medical applcation. *IEEE TRANSACTIONS ON ULTRASONICS, FERROELECTRICS AND FREQUENCY CONTROL*, 34[1], 1987. doi: 0885-3010/87/0100-000.

[14] Ehsan Jafarzadeh and Anthony N. Sinclair. Non-linear wave propagation and safety standards for diagnostic ultrasound devices. *Ultrasound in Med. Biol.*, 45:11–20, 2019. doi: https://doi.org/10.1016/j.ultrasmedbio.2018.08.021.

[15] Farid Ullah Khan and Izhar. State of the art in acoustic energy harvesting. *Journal of Micromechanics and Microengineering*, 25, 2015. doi: 10.1088/0960-1317/25/2/023001.

[16] Jina Kim, B. L. Grisso, J. K. Kim, Dong Sam Ha, and D. J. Inman. Electrical modeling of piezoelectric ceramics for analysis and evaluation of sensory systems. *2008 IEEE Sensors Applications Symposium*, pages 122–127, 2008.

[17] J.P. Lefebvre. Chapter 1 - physical basis of acoustics. *Academic Press*, pages 1 – 39, 1999. doi: https://doi.org/10.1016/B978-012256190-0/50002-6.

[18] Efthymios Maneas, Wenfen Xia, Daniil I Nikitichev, Batol Daher, Maniragav Manimaran, Rui Yen J Wong, Chia-Wei Chang, Benyamin Rahmani, Claudio Capelli, Silvia Schievano, Gaetano Burriesci, Sebastien Ourselin, Anna L David, Malcolm C Finlay, Simeon J West, Tom Vercauteren, and Adrien E Desjardins. Anatomically realistic ultrasound phantoms using gel wax with 3d printed moulds. *Phys. Med. Biol.*, 2018.

[19] Francesco Mazzilli, Cyril Lafon, and Catherine Dehollain. A 10.5 cm ultrasound link for deep implanted medical devices. *IEEE transactions on biomedical circuits and systems*, 8, 2014. doi: 10.1109/TBCAS.2013.2295403.

[20] Omer Oralkan, Baris Bayram, Goksen G. Yaralioglu, A. Sanli Ergun, Mario Kupnik, David T. Yeh, Ira O. Wygant, and Butrus T. Khuri-Yakub. Experimental characterization of collapsed-mode cmut operation. *IEEE transactions on ultrasonics, ferroelectrics, and frequency control*, 53(8), 2006.

[21] Shaul Ozeri and Doron Shmilovitz. Ultrasonic transcutaneous energy transfer for powering implanted devices. *Ultrasonics*, 50:556–566, 2010.

[22] Shaul Ozeri, Doron Shmilovitz, Signmond Singer, and Chua-Chin Wang. Ultrasonic transcutaneous energy transfer using a continuous wave 650 khz gaussian shaded transmitter. *Ultrasonics*, 50, 2010.

[23] Michela Peisino. Deeply implanted medical device based on a novel ultrasonic telemetry technology. *École polytechnique federale de Lausanne*, 2013.

[24] Philips. Capacitive micromachined ultrasound transducers. *https://www.innovationservices.philips.com/looking-expertise/mems-microdevices/mems-applications/capacitive-micromachined-ultrasonic-transducers-cmut*.

[25] Giuseppina Puzzilli, Bogdan Govoreanu, Fernanda Irrera, Maarten Rosmeulen, and Jan Van Houdt. Characterization of charge trapping in sio2/al2o3 dielectric stacks by pulsed c–v technique. *Microelectronics Reliability*, 47(4):508 – 512, 2007. doi: https://doi.org/10.1016/j.microrel.2007.01.040.

[26] TUV Rheinland. Active implantable medical devices (aimd). *https://www.tuv.com/thailand/en/active-implantable-medical-devices-(aimd).html*.

[27] Maurice G.L. Roes, Jorge L. Duarte, Marcel A.M. Hendrix, and Elena A. Lomonova. Acoustic energy transfer: A review. *IEEE TRANSACTIONS ON INDUSTRIAL ELECTRONICS*, 60[1], 2013.

[28] Marta Saccher. Mems ultrasound for active implantable devices. 2019. doi: https://repository.tudelft.nl.

[29] Dongjin Seo, Jose M. Carmena, Jan M. Rabaey, Elad Alon, and Michel M. Maharbiz. Neural dust: An ultrasonic, low power solution for chronic brain-mahine interfaces. *Helen Wills Neuroscience Institute*, 2013.

[30] Henry A. Sodano, Daniel J. Inman, and Gyuhae Park. A review of power harvesting from vibration using piezoelectric materials. *The Shock and Vibration Digest*, 36[3], 2004. doi: 10.1177/0583102404043275.

[31] S. H. Song, A. Kim, and B. Ziaie. Omnidirectional ultrasonic powering for milimeter-scale implantable devices. *IEEE transactions on biomedical engineering*, 62, 2015. doi: 10.1109/TBME.2015.2444854.

[32] Victor Farm-Guoo Tseng, Sarah S. Bedair, and Nathan Lazarus. Acoustic wireless power transfer with receiver array for enhanced performance. *U.S. Army Research Laboratory*.

[33] Silvio L. Viera, Theo Z. Pavan, Jorge E. Junior, and Antonio A. O. Carneiro. Paraffin-gel tissue-mimicking material for ultrasound-guided needle biopsy phantom. *Ultrasound in Med. Biol.*, pages 2477–2484, 2013. doi: https://doi.org/10.1016/j.ultrasmedbio.2013.06.008.

[34] Max L. Wang, Ting Chia Chang, Thomas Teisberg, Marcus J. Weber, Jayant Charthad, and Amin Arbabian. Closed-loop ultrasonic power and communication with multiple miniaturized active implantable medical devices. *IEEE*, 2017.

[35] Max L. Wang, Ting Chia Chang, and Amin Arbabian. Ultrasonic implant localization for wireless power transfer: Active uplink and harmonic backscatter. *IEEE Int Ultrason Symp.*, 2019.

[36] Xiaojuan Wei and Jing Liu. Power sources and electrical recharging strategies for implantable medical devices. *Front. Energy Power Eng.*, 2:1–13, 2008. doi: 10.1007/s11708-008-0016-3.

[37] Qi Xu, Zhaolong Gao, Hao Wang, Jiping He, Zhi-Hong Mao, and Mingui Sun. Batteries not included. *IEEE Microwave Magazine*, 2013. doi: 10.1109/MMM.2012.2234640.

[38] Goksen G. Yaralioglu, Baris Bayram, and Butrus T. Khuri-Yakub. Finite element analysis of cmutss: Conventional vs. collapse operation modes. *IEEE Ultrasonics Symposium*, pages 586–589, 2006. doi: 1051-0117/06.

[39] Yihan Zhang and Kenneth L. Shepard. A $0.6mm^2$ powering and data telemetry system compatible with ultrasound b-mode imaging for freely moving biomedical sensor systems.

[40] Y. Zhu, SOR. Moheimani, and MR. Yuce. Ultrasonic energy transmission and conversion using a 2-d mems resonator. *IEEE Electron Device Letters*, 2010. doi: https://doi.org/10.1109/LED.2010.2040575.